Mechanical characterization of the flexible epoxy adhesive EA9361 and its influence on hybrid bolted/bonded joint design

Gyu-Hyeong, Lim

Department of Mechanical Engineering

McGill University

Montreal, Quebec

11th April 2016

A thesis submitted to McGill University in partial fulfillment of the requirements of the degree of Master of Engineering

My Best Picture from Jerónimos Monastery, Lisbon during ICCM 2015


Left: Larry at Jerónimos Monastery, Lisbon during ICCS 2015

I was with my camera that we actually have no picture together

Right: Gyu Lim and Chanvit Viriyasuthee

Two good additions, a Korean and a Thai, to Larry’s diverse student body =)

Abstract

This study investigates the properties of flexible epoxy adhesives and their applicability in the design of hybrid bolted/bonded joints. There is increasing interest in using flexible adhesives for joint design, due to their ductility that enables significant elongation before failure. Generally, the behaviour of ductile adhesive involves considerable nonlinearities including large deformation, nonlinear material properties and plasticity. Analysis of flexible adhesives is more challenging than that of stiff adhesives, which is sufficiently described by linear elasticity and infinitesimal strain theory. The present study experimentally characterizes EA9361, selected as the representative material for flexible epoxy adhesives. The tensile tests, based on ASTM D638, generate stress/strain relation and also measure the evolution of Poisson's ratio throughout the strain until failure. From the stress/strain curve of the tensile tests, distinct yielding is observed. Therefore, in order to further understand the yielding nature of the epoxy adhesive, biaxial tests are then performed using a custom-designed Arcan fixture. While the biaxial tests try to capture yield stresses at different levels of biaxial loading, sharp stress concentrations are developed in the adhesive due to the constraint effects caused by high Poisson's ratio. Consequently, the values of the measured yield stresses are severely underestimated except for the pure shear case. From the pure shear case, the shear stress/strain relation is presented. Also tested is the adhesive under tension-tension cyclic loading in order to investigate the evolution of material properties through repeated cycles of plastic deformation. The results show that the material response converges in the presence of yielding and significant viscous effects. In addition to the above material characterizations, hybrid bolted/bonded joints are tested under cyclic loading in order to simulate *in-situ* application of a flexible adhesive. The results of the joint testing show that, despite the complex adhesive's response due to yielding and viscous effects, proper use of flexible epoxy adhesives could help design hybrid joints that operate at higher efficiency. Additionally, a new methodology to measure adhesive strain for a very thin adhesive bondline is proposed, and the custom-designed testing and manufacturing devices are introduced.

Abrégé

Cette étude porte sur les propriétés d'un adhésif flexible et son applicabilité dans la conception du joint hybrides boulonnés/collés pour structures aérospatiales. En raison de sa ductilité qui permet un allongement significatif avant l'échec, l'utilisation d'adhésif flexible pour la conception des joints suscite un intérêt croissant. En général, le comportement de l'adhésif ductile est considérablement non-linéaire : ceci inclut de grande déformation, des propriétés de matériaux non-linéaires et la plasticité. L'analyse d'un adhésif flexible est plus difficile que celle d'un adhésif rigide, qui est suffisamment décrit par élasticité linéaire et la théorie de déformation infinitésimale. La présente étude caractérise expérimentalement des adhésifs époxy flexibles, en utilisant EA9361 comme matériau représentatif. Les essais de traction, selon ASTM D638, génèrent des relations entre la contrainte et la déformation et mesurent également l'évolution du coefficient de Poisson au long du processus de contrainte jusqu'à la rupture. De l'écoulement plastique distincte est observé par des tests de traction. Ensuite, afin de définir la transition entre l'élasticité et la plasticité, des tests bi-axiaux sont effectués en utilisant un montage Arcan conçu sur mesure. Alors que les tests bi-axiaux tentent de mesurer des limites d'écoulements à différents niveaux de chargement bi-axial, des concentrations de contraintes sont développées dans l'adhésif en raison des effets de contraintes causées par le coefficient de Poisson élevé. Par conséquent, les valeurs de la limite d'écoulement sont gravement sous-estimées, sauf pour le cas de cisaillement pur. Dans le cas de cisaillement pur, la relation entre la déformation de cisaillement et la contrainte est notée. On a également testé l'adhésif sous une charge cyclique tension-tension, afin d'étudier l'évolution de la réponse du matériau par des cycles répétés de déformation plastique. Les résultats montrent que la réponse du matériau converge en présence d'écoulement et d'effets visqueux. En outre des caractérisations des matériaux ci-dessus, joints hybrides boulonnés / collés sont testés sous une charge cyclique afin de simuler l'application *in-situ* d'un adhésif flexible. Les résultats des tests de joints montrent que, en dépit de la complexité en raison de plasticité et les effets visqueux d'adhésifs ductiles, leur utilisation appropriée pourrait aider à la conception des articulations hybrides d'une plus grande efficacité. En plus, une nouvelle méthodologie pour mesurer un allongement adhésif pour un collage très mince est proposée, et des appareils d'essai et de fabrication sur mesure sont introduits.

Acknowledgement

First and foremost, praise and thanks goes to my savior Jesus Christ, whose plan and blessing for me has led myself to McGill and to the loving supervisor, Prof. Lessard, and all other supporters. I humbly wish that His name be glorified through the presented work, and that His love and blessing be upon each person mentioned below.

I express my gratitude to my supervisor, Professor Larry Lessard, for his technical and financial support along with his kind motivation during the entire period of the research.

I thank all the collaborating industrial sponsors and research institutes including Bombardier Aerospace, L3 Communications, Delastek, Consortium de Recherche et d'Innovation en Aérospatiale au Québec (CRIAQ), Natural Science and Engineering Research Council of Canada (NSERC), Carleton University, Ecole Polytechnique de Montreal, and McGill University.

I express my gratitude to my research colleagues, Kobye Bodjona and Karthik Raju, for generously sharing their knowledge and experience throughout my research work.

I sincerely thank Professor Pascal Hubert and all the member of the Structures and Composite Matrerials Laboratory of McGill University, for kindly sharing the necessary equipment and training me to use them, and to kindly sharing with me advice and insights to help advance my research.

I thank all who have either directly or indirectly supported me in completing the research and scripting of the thesis.

Lastly, I sincerely thank my father, Dae-hwui Lim, and mother, Sun-hyung Kim, for their unconditional love and continual prayers.

CONTRIBUTIONS OF THE AUTHOR

The author of this thesis has performed all the work presented therein, with the following exceptions.

Chapter 7: Kobye Bodjona, a Ph.D student in the Structures & Composite Materials Laboratory, designed the mold for the manufacturing of the hybrid bonded joints, and developed the methodology of the manufacturing.

Chapter 7: Sean Fielding, a undergraduate summer intern in the Structures & Composite Materials Laboratory, manufactured the CFRP (carbon-fiber reinforced plastic) plate, from which the substrates of the hybrid joints are manufactured.

The author acknowledges these contributions.

Table of Contents

List of Figures

List of Tables

Nomenclature

Symbols

$A = area\ over\ which\ to\ calculate\ tensile\ stress$

$E = strain\ energy\ density\ function$

$d = joint\ displacement$

$F = axial\ force$

$\bar{\bar{F}} = two\ dimensional\ deformation\ gradient$

$I_1, I_2 = Invariants\ of\ Cauchy\ Green\ deformation\ tensor$

$L = length$

$P = shear\ force$

$t = thickness$

$T = time$

$\bar{\bar{T}} = two\ dimensional\ stress\ tensor$

$u = displacement\ in\ horizontal\ directoin$

$v = displacement\ in\ vertical\ direction$

$W = width$

$\lambda = stretch$

$\sigma = axial\ stress$

$\varepsilon = strain$ (scalar, in the adhesive for the tensile testing)

$\tau = shear\ stress$

$\upsilon =$ Poisson′s ratio

$\theta = angular\ deformation$

Subscripts

$i = spatial\ coordinate\ index$

$j = spatial\ coordinate\ index$

$MR = Mooney\ Rivlin\ formulation\ of\ hyperelasticity$

$o = initial\ (T = 0)$

$r = relative, for\ displacement\ of\ adherends$

$x = horizontal\ coordinate$

$y = vertical\ coordinate$

$Eng = engineering\ (for\ stresses\ and\ strains)$

$True = true\ (for\ stresses\ and\ strains)$

1. Introduction and Literature Review

1.1 Bonded Joints and Bolted Joints

1.1.1 The types of joints

Structures consist of numerous components. It is impractical to design a large structure using only a single part for functionality and manufacturability. Therefore, joining components is inevitable to achieve the final assembly of a complex structure, such as an aircraft. Joints are the critical locations of structures where the flow of loads converges. Therefore, proper joint design is essential to ensure structural integrity. For the past decades, two major techniques to connect components have been employed in the aerospace industry. One is mechanical fastening [1-3] and the other is adhesive bonding [4].

Mechanical fastening in aerospace applications is most often in the form of bolts or rivets. The bolts are the fasteners that carry both tension load and shear load. Therefore, the two types of bolted joints are classified as tension joints and shear joints. Figure 1(a) and (b) illustrate the tension joints and shear joints, respectively [5]. Rivets are designed to counteract shear load, but they have a limited load bearing capacity against tension loads [6]. Therefore, riveted joints are used only in the form of a shear joint. The comparison between the riveted shear joint and bolted shear joint is shown by Figure 2.

The common types of bonded joints include single lap joints, double lap joints, scarf joints and stepped joints [4]. They are illustrated by Figure 3. Amongst the presented types, the shear lap joint is the type most commonly found in aerospace structures because they are appropriate for joining panels and shell structures.

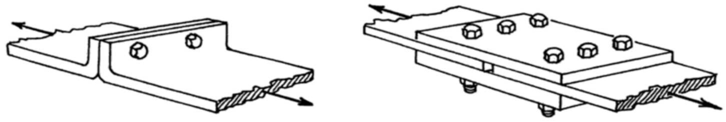

a) Tension joint b) Shear joint

Figure 1. Types of bolted joints.

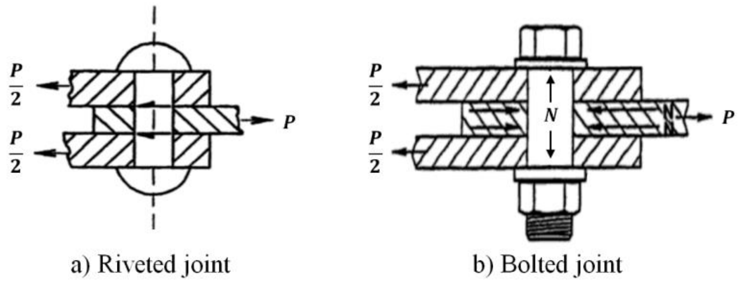

Figure 2. Shear joints with fasteners.

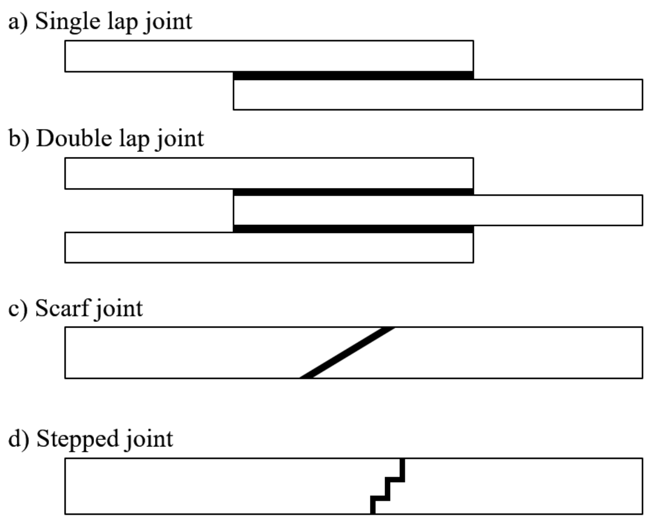

Figure 3. The common types of bonded joints.

1.1.2 Characteristics of bolted joints and bonded joints

Adhesive bonding and mechanical bolting have their advantages and disadvantages. Bonding is more weight efficient since adhesives add significantly lower weight to the joints than bolts. The weights of the bolts are substantial as they're made of high strength steel or titanium. Consequently, the bonded joints have superior strength-to-weight ratio compared to the bolted joints [7] when used with the conventional aerospace adhesives. Furthermore, the substrates of the bonded joints are less exposed to stress concentration than those of the bolted joints because they contain no cut-out, as seen by Figure 4 [8]. Nevertheless, Bonding involves difficulties with quality control and damage inspection. For example, the joint strength of bonded joints is sensitive to the adhesive thickness [9]. But, the bond is very thin and its thickness control is difficult and costly. Also the bonded joints' failure is abrupt and catastrophic [10]. Such downsides present challenges to certify bonded joints for commercial aerospace applications despite the weight-saving advantage. The bolted joints possess properties that compensate for these downsides. The repeatability in the bolt production attains consistent quality control. If properly designed for bearing failure, the failure mechanism is controlled to be progressive, therefore catastrophic failure is avoidable [11]. In case of the damage in the bolt, the repair process is easily done by the replacement of bolts. Lastly, the metallic bolts are resistant to surrounding conditions [7].

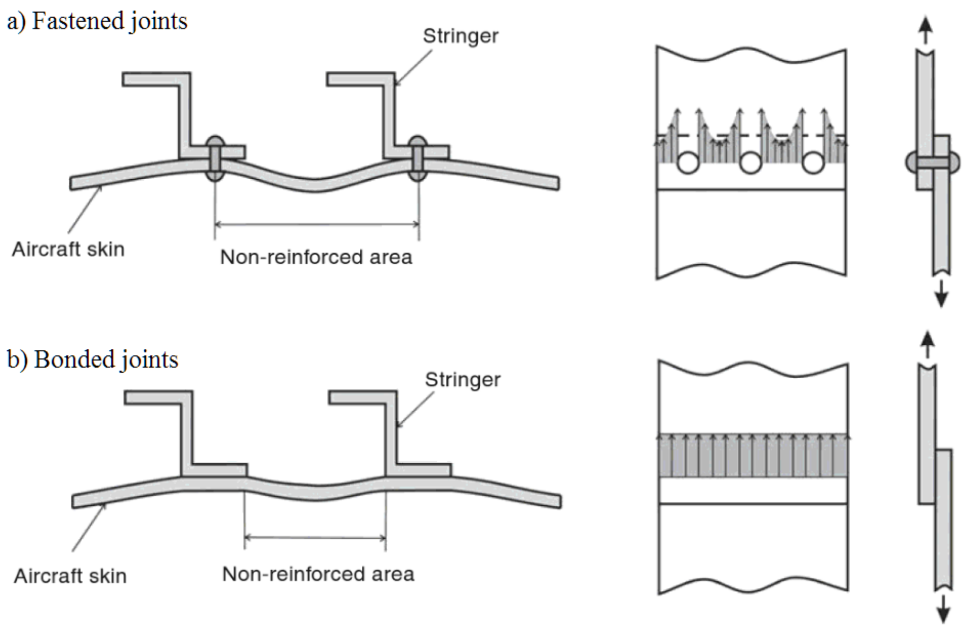

Figure 4. Stress concentration in the substrate: bolted joint vs bonded joint.

1.2 Hybrid Bonded/Bolted Joint

Combining a bonded joint and a bolted joint leads into a hybrid boned/bolted joint, which retains the advantages and reduces the downsides of each constituent joint type. Figure 5 visually compares the bonded joint, the bolted joint, and the hybrid bolted/bonded joint in the configuration of a single lap joint. In the rest of the text, the hybrid bonded/bolted joint is to be called the hybrid joint for simplicity.

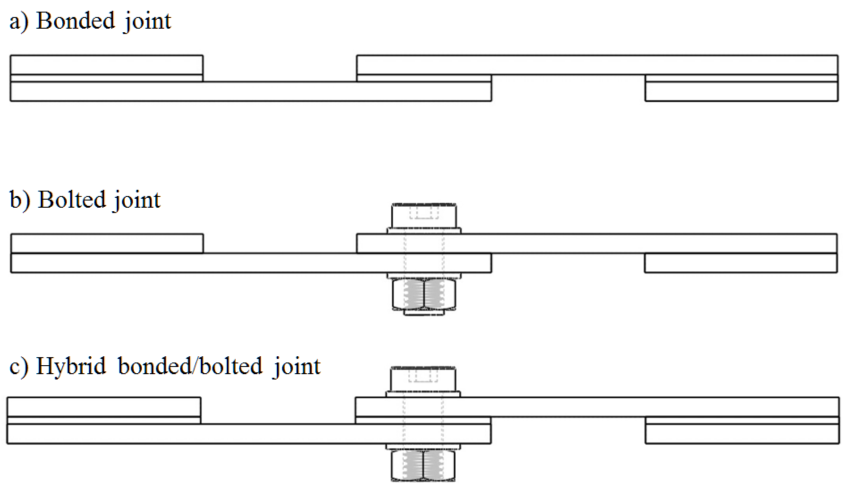

Figure 5. Bonded joint, bolted joint, and hybrid bonded/bolted joint
in the single lap joint configuration.

1.2.1 Hybrid joint with traditional stiff adhesive

Hybrid bolted/bonded joints have been studied to demonstrate its potential to be a superior joint type over either type of the two traditional joints. The early study by Hart-Smith [12] introduces the hybrid joints for aerospace applications. His investigation on single-bolted hybrid joint shows that the insertion of a bolt to a bonded joint does not improve the joint strength even if the bolt adds to the total joint weight. But the bolt contributes to slow down the crack propagation in a joint whose adhesive has failed. The additional investigation by Fu and Mallick [13] realizes the superior fatigue resistance of a hybrid joint (singled-bolted). The study by Chowdhury *et al.* [14] extends these findings to hybrid joints with multiple fasteners. Their experimental results find that the multi-fasteners hybrid joints have strength only marginally higher than that of bonded joints. But similar to the previous studies from the single-bolted hybrid joints, Chowdhury quantifies the improved fatigue life of the hybrid joints over those of fastened joints and bonded joints. These previous studies are carried out with the traditional aerospace adhesives that have been used in bonded joints for the past few decades. Such adhesives are strong and stiff as they have to meet the structural integrity required by the heavily loaded applications.

1.2.2 Hybrid joint with flexible adhesive

Further investigation on the hybrid joints reveal that improvement is feasible through the use of less stiff adhesives. The experimental study by Kweon *et al*. [15] compare hybrid joints with two different adhesives, one substantial weaker than the other. As they test the hybrid joints with the weaker adhesive, they realize that the hybrid joint's strength is significantly superior to the strength of the bonded joint of the same adhesive. This result is in contrast to the hybrid joint with stiff adhesive discussed in Section 1.2.1, for which the strengths of the hybrid joints and bonded joints are observed to be equivalent. Kweon *et al*. realize that the design of hybrid joints become effective, given that its constituent bolted joint is stronger than the bonded joint.

Kelly [16] introduces the use of flexible adhesive in hybrid joints. He considers the bolt load sharing to be a key parameter to the mechanics of the hybrid joints. When the traditional stiff adhesives are used, the bond carries most of the load and the bolt is ineffective. As a result, the hybrid joints with stiff adhesive fail at the failure load of the bonded joint. Therefore, the design of the hybrid joints with a stiff adhesive is highly inefficient. When adhesives with lower modulus are used, the bolts can participate in reacting the load as well as the bond. Efficient hybrid joint design is attained through the use of low-modulus adhesives. The capacity for large deformation and the higher failure strain of flexible adhesives are also beneficial for hybrid joints. In the presence of the bolt hole clearance (Figure 6), there has to be certain deformation of the bond until the bolts touches the hole, after which bolts start carrying the load. In case of the stiff adhesive with low failure strain, the bond may fail even before the bolt starts touching the bolt hole.

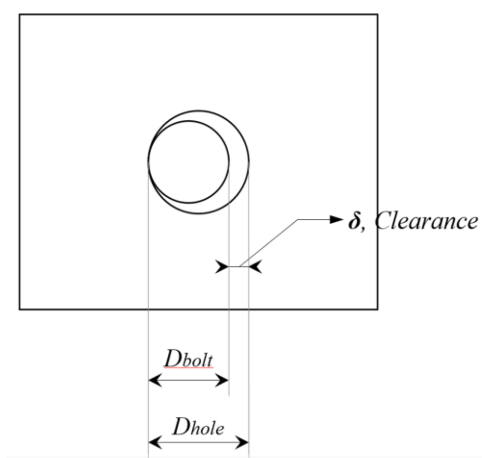

Figure 6. Bolt hole clearance.

In order to investigate hybrid joints with flexible adhesives, it is first attempted to confirm the improved bolt load sharing. By installing a miniscule strain gage on the bolt's shank, Kelly [16] experimentally measures the shear force through the bolt of his single-lap hybrid joint. The stress/strain relation of the three representative adhesives of different modulus and their corresponding bolt load sharing presented are shown in Figure 8. With increasing applied load, Kelly's hybrid joint shows the bolt load transfer $\left(= \frac{F_{bolt}}{F_{total}}\right)$ over 40% when tested with the flexible polyurethane adhesive, *Pilogrip 7400/7410*. The joints with stiffer adhesive has negligible load through the bolts. Similar experiments by Bodjona *et al*. [17] utilize such an instrumented bolt and measure the bolt load transfer of his hybrid joints with a flexible epoxy adhesive. Kobye finds agreement between the measurements and his three dimensional finite element modeling, in which the bolt load transfer levels are compared.

Following the verification of the improved bolt load sharing, the improved performances of hybrid joints with flexible adhesives are studied. Kelly's static tests [10] compare the strengths of bolted joints, bonded joints and hybrid joints. The results show the hybrid joints' strength being significantly greater than those of both bonded joints and bolted joints, possible through the proper load transfer into the bolts. His study also finds that the use of flexible adhesive offers significant improvement in fatigue resistance, while the use of stiff adhesive negligibly contributes. In a follow-up, quasi-static tests by Bodjona and Lessard [18] compare hybrid joints with stiff and flexible adhesive and find that the latter achieves higher joint strength. The superior strength is not only due to the improvement in the bolt load transfer, but also due to the capacity of the flexible adhesive to eliminate adhesive peak stress found in bonded joints [19]. This peak-stress-relieving capacity of ductile adhesive, numerically verified by Loureiro *et al*. [20] in 2D and by Hoang-Ngot and Paroissien [21] in 3D, contributes to control the adhesive failure in hybrid joints. Figure 8 shows the nearly uniform stress distribution in the flexible adhesive without peak stresses.

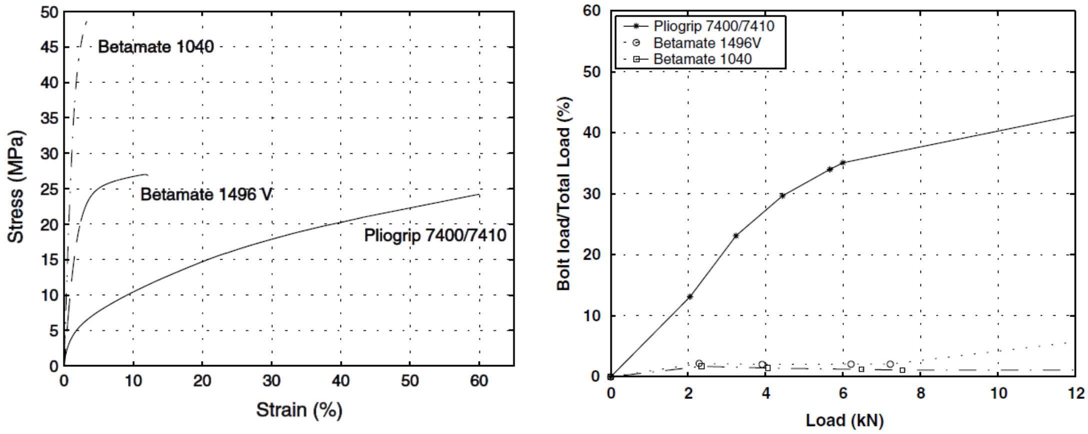

Figure 7. Representative adhesives and corresponding bolt load sharing in hybrid joints.

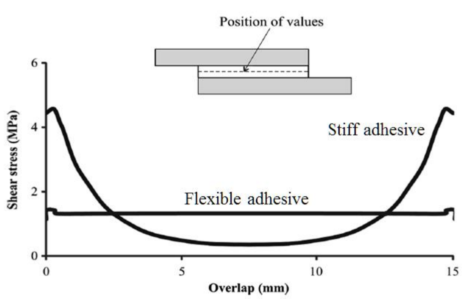

a) Two-dimensional analysis

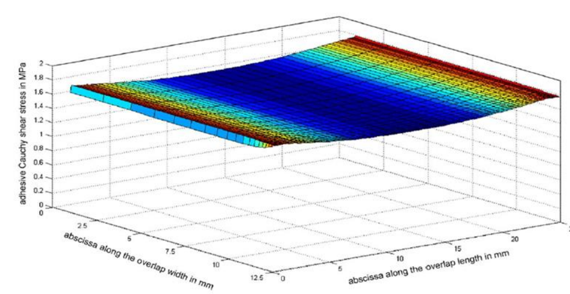

b) Three-dimensional analysis

Figure 8. Stress alleviation in a SLJ due to flexible adhesive.

(a) 2D analysis (b) 3D analysis

1.3 Characterization of Flexible Adhesive

It is evident that the use of flexible adhesive is essential for improving the performance of hybrid joints. Nevertheless, the nature of a flexible adhesive involves tremendous complexity. The stress/strain response is nonlinear [22-24] and their large deformation adds to the nonlinearity. [22, 25] Flexible adhesives are also viscoelastic in nature that they exhibit different response under different loading rate [26, 27]. Moreover, the mechanical properties of the flexible adhesives are subject to significant change with temperature [28, 29]. Currently, there exist insufficient experimental data to fully understand the properties of the flexible adhesives [20, 22].

Nevertheless, a few attempts have been made in order to initiate the characterization of the flexible adhesives of a few different adhesive groups.

One group is the elastomeric adhesives. Crocker et al. [24] present the experimental results of tensile tests, biaxial tension tests and planar shear tests for the commercial adhesive, M70. The particular three tests are performed such that the results are incorporated into the hyperelastic material model. But when M70 is simulated through finite element modeling, the hyperelastic material model is shown to be insufficient to imitate the mechanics of flexible adhesive [30]. Another characterization performed is the Thick Adhered Shear Test (TAST) by Mariana [23] on the two adhesives, Sikaflex 552 and AS1805, which adds to shear properties of elastomeric adhesives. From the studied elastomeric adhesives, significantly low modulus and strength are found. Although the low modulus is desired for increasing the bolt load transfer in hybrid joints, their low strength is considered inadequate for heavily loaded aerospace application. For example, the representative adhesive, M70, has its strength an order magnitude lower than the strengths of other types of representative adhesives as shown in Table 1. Its strength is also two to three orders of magnitudes lower than those of metallic or fiber-reinforced materials that are generally used as joints' adherends.

Another group is the polyurethane adhesive. Crocker et al. [24] and Kelly [16] present the stress/strain relation of DP609 and Pilogrip 7400/7410, respectively. In the case of Pilogrip 7400/7410, Kelly's measurement shows the proper bolt load transfer achieved in the hybrid joints. Therefore, the modulus of the flexible polyurethane adhesives is considered appropriate for hybrid joint application. Also observed is the adequately high failure strain of 60%. Afterwards, Kelly performs finite element analysis using his measured adhesive's properties. His numerical simulation of the hybrid joint approximates the bolt load transfer, which matches his experimental measurement, verifying the validity of the adhesive characterization.

The last group is the epoxy adhesives. Da Silva [26] presents tensile test results for a flexible epoxy adhesive, EA9361. The initial modulus of EA9361, reported by its datasheet [31], is very close to the modulus of the polyurethane adhesive, Pilogrip 7400/7410 which has been proven appropriate for hybrid joint application. However, Da Silva's results show that that the epoxy adhesive yields, after which sharp drop in modulus is found. When the stress/strain of the epoxy and polyurethane adhesives are plotted together, the epoxy adhesive shows significantly lower modulus than the polyurethane adhesive after yielding, though the initial moduli of the two are similar. This observation is illustrated in Figure 9. Such reduced modulus shows the potential of the epoxy adhesive to achieve superior bolt load transfer in hybrid joints. This introduces the flexible epoxy to be another appropriate adhesive type for hybrid joints. Through further characterization of flexible epoxy adhesives, their properties can be better understood, based on which their applicability to the design of aerospace hybrid joint can also be examined.

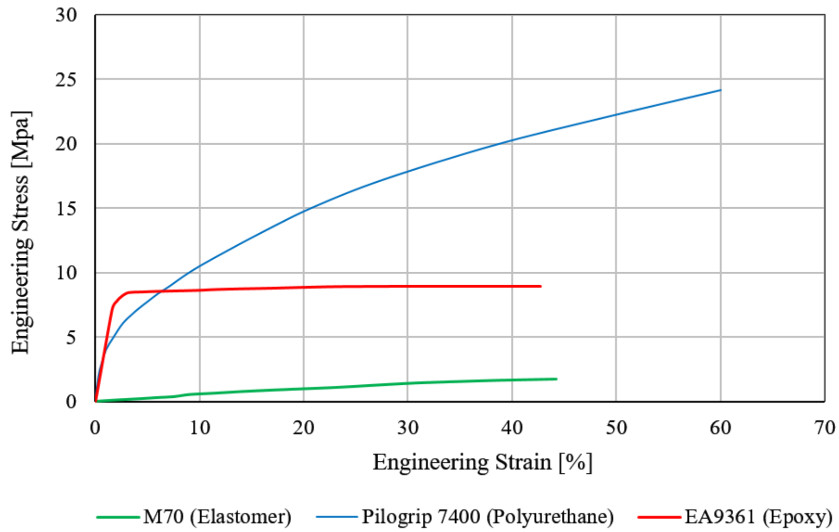

Figure 9. Stress/strain of the flexible adhesives of different types at room temperature.

Table 1. Mechanical properties of flexible adhesives of different types at room temperature.

Adhesive Name	Adhesive Type	Initial Tensile Modulus [MPa]	Yield Stress [MPa]	Failure Strength [MPa]	Failure Strain [%]	Comment
M70	Elastomer	6.9 [24]	Not applicable	1.7 [24]	44 [24]	The strength doesn't meet the requirement for heavily loaded aerospace applications.
Pilogrip 7400	Polyurethane	687 [16]	Not applicable	24 [16]	60 [16]	Polyurethane adhesives are considered appropriate for aerospace hybrid joint applications. [16]
EA9361	Epoxy	723 [31]	8.5 [26]	9 [26]	43 [31]	Epoxy adhesives possess the potential to be used in aerospace hybrid joint design.

2. Problem Statement and Methodology

2.1 Problem Statement

The literature review introduces the flexible adhesives and explains their role in hybrid joint applications. Only recently, attention has been made to the use of flexible adhesives, and there is a lack of information on their nature and properties. Further understanding of these adhesives is possible through experimental characterization, and subsequent interpretation of the measured properties can lead to improving the design of the hybrid joints.

This study aims to characterize flexible epoxy adhesives. Their properties are relatively less investigated compared to other types of adhesives, but they have the potential to be a well-fitting adhesive type for the hybrid joint application. Several mechanical properties of flexible epoxy adhesives can be experimentally investigated. These includes tensile modulus, shear modulus, Poisson's ratio, yield strength, failure strength and so on. It is essential to know and understand these properties to perform structural analysis for the adhesives. Several pre-established test standards and methodologies are available, with which these properties can be measured. [32, 33] The first objective of this study is to quantify the mechanical properties of a representative material to be selected.

A material has particular values of yield stresses when loaded in different directions. For example, a material has its distinct tensile yield stress, shear yield stress and also the yield stresses at different multi-axial loads. How the material's yield stress changes under various loading orientations is different for different materials. Therefore, several yield surface models exist to serve materials with different yielding behavior. For example, Von Mises is considered appropriate for ductile metals [34], and Drucker-Prager cap model for geotechnical materials such as soil [35]. The two most common models for isotropic materials, Von Mises and Tresca, are illustrated in Figure 10. It is known that that the epoxy adhesives yield [26] and therefore the way they yield is be studied as a part of the characterization. The second objective is to investigate the multi-axial yielding behaviors of flexible epoxy adhesives and to select the most suitable yield surface model.

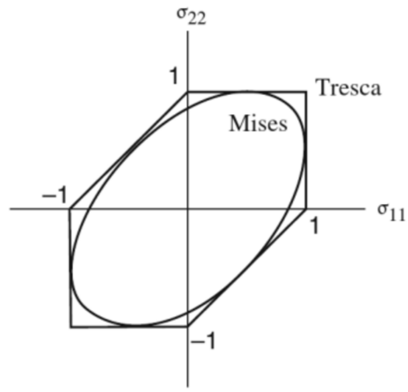

Figure 10. Von Mises and Tresca models.

The last objective is to study the properties of the epoxy adhesive under repeated loading. As epoxy adhesives yield, they deform plastically and consequently their properties permanently change. Therefore, it is expected that in the *in-situ* applications the adhesive's properties would progressively evolve throughout the life span of the joints. For example, the helicopter is under cyclical loads caused by the rotating blade. Another example is that any aircrafts are exposed to countless landings due to repeating flights. Therefore, designing hybrid joints with flexible epoxy adhesives has to be accompanied by proper understanding of their evolving properties.

2.2 Methodology

The present study selects EA 9361 AERO by Hysol as the representative thermoset material for flexible epoxy adhesives. EA 9361 is one of the few aerospace standard flexible epoxy adhesives that is commercially available. Another candidate was unavailable due to US export controls and its name is forbidden to be disclosed. Table 2 lists a number of main properties of the thermoset resin, EA 9361, extracted from the product's technical datasheet. The complete datasheet for EA9361 is found in Appendix A.

In this study, EA9361 is characterized through three different experiments: tensile tests, biaxial tests and hysteresis tests. The tensile tests are to be performed based on ASTM D638 [32]. The tensile tests are able to capture the stress/strain relation and the evolution of Poisson's ratio throughout the tensile deformation until failure. By observing the stress/strain curve, one can also quantify several mechanical properties including tensile modulus, yield stress and failure strength.

Biaxial tests are also performed to measure yield stresses at different biaxial loading orientations. Applying biaxial loads of different orientations can be achieved through the use of a mechanical fixture that allows the sample to rotate under a MTS machine. Such fixtures are the Iosipescu fixture or the Arcan fixture [33, 36-38]. The present study employs the Arcan fixture, which involves a simpler design than the Iosipescu fixture, to apply biaxial loads on the adhesive. With the measured yield stresses, the best fitting yield surface model for flexible epoxy adhesive is to be determined.

Hysteresis tests study the response of EA9361 in its bulk form under cyclic loads. For this study, the set-up of the testing is based on ASTM D638 similar to the tensile tests. The adhesive is repeatedly loaded beyond its yield stress so that the effect of the accumulating plastic strain can be monitored. From the results of the tests throughout the cyclic loads, the evolution of the stress/strain relation can be qualitatively studied.

In addition to the three experiments for material characterization, the hybrid joints with EA9361 are tested under cyclic loads. The joints to be tested take the configuration of a single-lap joint with a single bolt. The tests intend to investigate the *in-situ* response of the flexible epoxy adhesive and the hybrid joints. The qualitative interpretation of the results is to be related to the improvement in the bolt load sharing. Also, from the results of the joint tests, the traces of the findings from the previous three characterizing tests are to be observed. Table 3 summarizes the tests to be performed and their objectives.

Table 2. Properties of EA 9361.

Properties	Part A	Part B	Mixed
Viscosity [Pa·s]	70	95	80
Density [g/mL]	1.33	1.26	1.28
Mix ratio (by weight)	100A : 140B		
Room temperature curing time (at 25 °C)	7 days		
Accelerated curing time (at 82 °C)	1 hour		

Table 3. Overview of the Experimental Plan.

Test Type	Standard or Reference	Objective	Nature of the results
Tensile Test	ASTM D638 [32]	Tensile Stress/Strain Poisson's Ratio Tensile yield stress and strength	Quantitative
Biaxial Test	Custom Designed	Pure Shear Stress/Strain Shear yield stress and strength Yield Surface	Quantitative
Hysteresis Test (Tension-Tension)	Modified ASTM D638	Evolution of Stress/Strain	Qualitative
Hybrid Joint Test (Tension-Tension)	Bodjona *et al*. [18]	Evolution of Force/Displacement Bolt load sharing	Qualitative

3. Review of Theory

3.1 Stress Formulation

3.1.1 Axial stress

Infinitesimal strain theory is commonly used in the field of structural engineering, as it can greatly simplify the formulation of stress and strain within a large range of materials. With infinitesimal strain theory, the use of engineering stress is available. The change in cross section area is negligible, therefore the change in the cross-section area is practically unaffected by the material's deformation. The engineering stress is defined as force over initial cross section area, where *i* is the index to indicate the axial direction.

$$\sigma_{i_{Eng}} = \frac{F_i}{A_o}. \tag{1}$$

Such simplification is unfortunately not suitable for large deformation in bodies, such as the case with flexible adhesives. When a material undergoes large deformation, the cross section area may significantly change. For example, a highly stretched body has its cross section area significant lower than the initial cross section area due to Poisson's effect. Such change in the cross section area has to be properly reflected in the stress calculation. The true stress is defined as force over instantaneous cross section area.

$$\sigma_{i_{True}} = \frac{F_i}{A}. \tag{2}$$

How much the cross-section area changes is dependent on the Poisson's ratio of the material of interest. An analytical means to relate the true and engineering stress is possible for the special case of incompressibility. [39]

$$\sigma_{i_{True}} = \lambda_i \cdot \sigma_{i_{Eng}}. \tag{3}$$

where the stretch is defined as

$$\lambda_i = \frac{L_i}{L_{i.o}}. \tag{4}$$

3.1.2 Shear stress

Shear deformation is independent of Poisson's effect, Therefore, a body deformed purely by shear involves no change in cross sectional area. Therefore, there is no distinction between true and engineering shear stress. The shear stress is defined as Eq (5) where the indices *i* and *j* indicate a plane on which the shear stress is present.

$$\tau_{ij} = \tau_{ij_{True}} = \tau_{ij_{Eng}} = \frac{P}{A}. \tag{5}$$

3.2 Strain Formulation

3.1.1 Axial strain

As in the stress formulations, infinitesimal strain theory derives engineering strain. With infinitesimal strain, the length of a deforming body changes negligibly, $L \approx L_o$, and the engineering strain is formulated as Eq (6).

$$\varepsilon_{i_{Eng}} = \frac{\Delta L}{L_o} = \frac{L - L_o}{L_o}. \tag{6}$$

When the body is subjected to large deformation, the use of engineering strain is insufficient. Assume that a two-dimensional deformable body shown in Figure 11 is elongated due to a tensile load, and its progressive deformed configurations are captured at three different times: T_0, T_1 and T_2 where the body is undeformed at T_o. The engineering strain developed between T_o and T_2 is

$$\varepsilon_{i\ (T=T_2)_{Eng}} = \frac{\Delta L_{o2}}{L_o}. \tag{7}$$

To calculate the strain at T_2 incrementally,

$$\varepsilon_{i\ (T=T_2)_{Inc}} = \frac{\Delta L_{o1}}{L_o} + \frac{\Delta L_{12}}{L_1}. \tag{8}$$

The larger the deformation is, the more accurate the incrementally calculated strain is compared to the engineering strain. Also, the smaller the incremental step is, the more accurate the strain calculation is. By taking an integral where the time steps approaches zero, the calculation of true strain is achieved.

$$\varepsilon_{i\ (T=T)_{True}} = \int_{L_o}^{L_2} \frac{dL}{L} = ln\left(\frac{L_2}{L_O}\right). \tag{9}$$

This formulation is generalized to the definition of true strain by taking the final length, L, at any given time.

$$\varepsilon_{i_{True}} = \int_{L_o}^{L} \frac{dL}{L} = ln\left(\frac{L}{L_O}\right). \tag{10}$$

Knowing that the instantaneous length equals the sum of undeformed length and total change in length, $L = L_o + \ \Delta L$, the true and the engineering strains are related as below.

$$\varepsilon_{i_{True}} = l\,n\left(1 + \varepsilon_{i_{Eng}}\right). \tag{11}$$

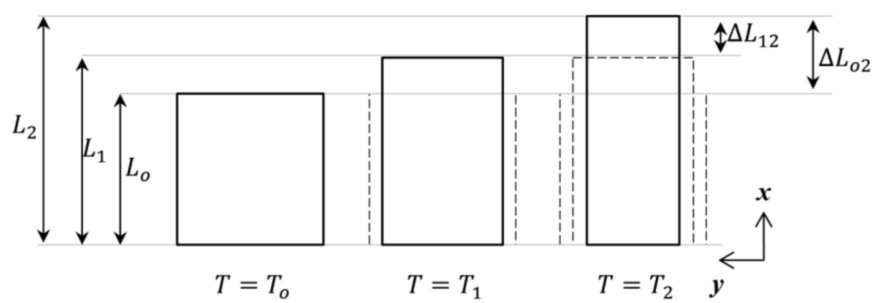

Figure 11. Deformable body under large tensile elongation.

3.1.2 Shear strain

Shear strain is a measure of angular deformation of a body, as illustrated by Figure 12. Therefore, the true shear strain is defined by,

$$\varepsilon_{ij_{True}} = \theta_{ij}. \tag{12}$$

Only when subjected to a very small strain, in which $\theta \approx \tan(\theta)$, the definition of engineering strain is feasible.

$$\varepsilon_{ij.Eng} = tan(\theta_{ij}). \tag{13}$$

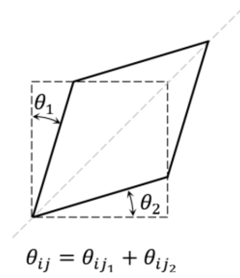

Figure 12. Two-dimensional shear strain.

3.3 Poisson's Ratio

Poisson's ratio measures the proportion with which a material expands or contracts in the transverse direction as a result to its longitudinal deformation. In other words, it is the ratio between the change in transverse strain and the change in the longitudinal strain. Assume that a deformable body has been elongated due to a tensile deformation during a time step between T_1 and T_2 as shown by Figure 13. Then the Poisson's ratio is approximated as Eq (14), where *i* and *j* indicates the longitudinal and transverse direction respectively. The minus sign in Eq (14) is present in order to ensure that the Poisson's ratio has a positive value. When a material is stretched in the longitudinal direction, it generally contracts in the transverse direction. Therefore, without the minus sign, the Poisson's ratio becomes a negative number. The strains used in Eq (14) have to be the true strains defined by Eq (11).

$$\upsilon = -\frac{(\varepsilon_{jj_2} - \varepsilon_{jj_1})}{(\varepsilon_{ii_2} - \varepsilon_{ii_1})} = -\frac{\Delta\varepsilon_{jj}}{\Delta\varepsilon_{ii}}. \tag{14}$$

If the Eq (14) is to be expressed in a differential form,

$$\upsilon = -\frac{d\varepsilon_{jj}}{d\varepsilon_{ii}}. \tag{15}$$

And the value of the Poisson's ratio approaches the exact value as the time step, $\Delta T = T_2 - T_1$, approaches zero.

$$\upsilon = \lim_{\Delta T \to 0} \left[-\frac{\int_{T_1}^{T_2} d\varepsilon_{jj}}{\int_{T_1}^{T_2} d\varepsilon_{ii}} \right]. \tag{16}$$

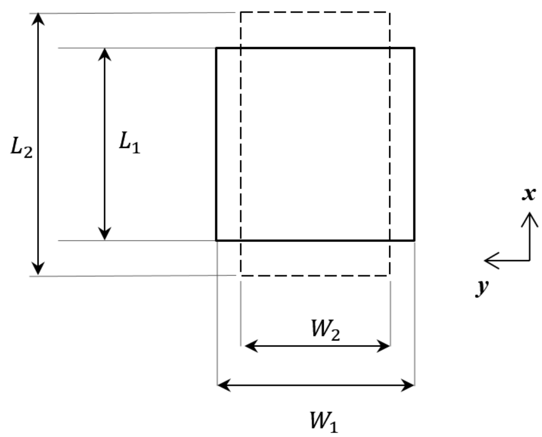

Figure 13. Two-dimensional illustration of Poisson's effect.

3.4 Comparison of True and Engineering Stress/Strain

Section 3.1 and Section 3.2 show how true stress and true strain are defined and formulated. And the two sections explain how they capture the effects of large deformation that the conventional definitions of engineering stress and strain are not able to. In addition to mathematically distinguishing them, Section 3.4 is dedicated to visually describe the differences. The stress/strain relation of a body that is axially loaded is to be plotted. Four curves are generated using each four permutations of stress/strain relations generated with true and engineering definition of stresses and strains.

For simplicity, despite the large deformation, the modulus of the body is considered constant with a value of unity. Furthermore, the body is considered incompressible. With these two conditions, Figure 14 is presented below. It is plotted such that the range of the engineering strain is between 0 and 1. It is clear from Figure 14 that significantly different results can be generated depending on which definition of the stress and strain is used. For example, for an incompressible material that has the strain, $\varepsilon_{Eng} = 1$, the stress could be twice as different, depending on using true or engineering stress. Considering the significant differences that are pronounced at large deformation, it is always recommended that one uses true stress and strain.

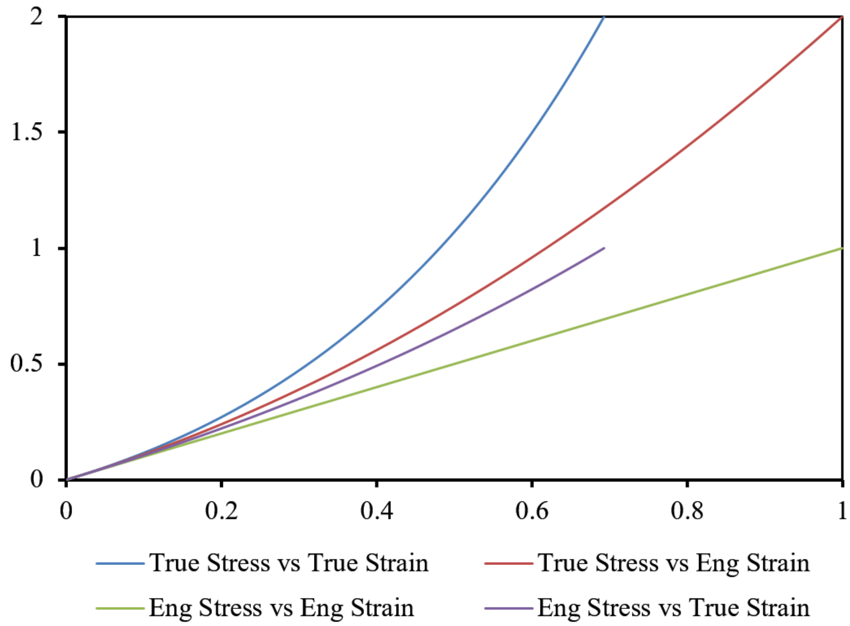

Figure 14. Comparison of stress/strain relation using true and engineering quantities.

Another aspect to be cautious of, besides the significant difference between the values of true and engineering quantities, is the curvature of the stress/strain curves. Depending on which definition of stress and strain, the curvature of the stress/strain curve may change. What seems to be linearly related may look nonlinearly related or vise versa. For example, in Figure 14, the straight curve of engineering stress/strain could be deceiving because the true quantities show that the relation is highly nonlinear.

3.5 Differentiation of Simple Shear and Pure Shear

3.5.1 Pure shear

Pure shear is the condition in which its stress state only includes shear stress and its strain state only includes shear strain. Since pure shear isolates shear from other component of stress or strain, it is used to describe the material properties in shear. The two-dimensional stress tensor of the pure shear state is as below.

$$\bar{\bar{T}} = \begin{bmatrix} 0 & \tau_{xy} \\ \tau_{xy} & 0 \end{bmatrix}. \tag{17}$$

If one transforms the above stress tensor by rotation of $\varphi = 45°$ using the transformation matrix, $\bar{\bar{R}} = \begin{bmatrix} cos(\varphi) & sin(\varphi) \\ -sin(\varphi) & cos(\varphi) \end{bmatrix}$, the pure shear becomes equivalent to biaxial loading with one component tensile and other component compressive.

$$\bar{\bar{T}}' = \bar{\bar{R}}\,\bar{\bar{T}} = \begin{bmatrix} -\sigma & 0 \\ 0 & \sigma \end{bmatrix}. \tag{18}$$

From the equivalent biaxial state expressed by the blue diagrams in Figure 15 (c), it is clear that pure shear involves no rigid body rotation.

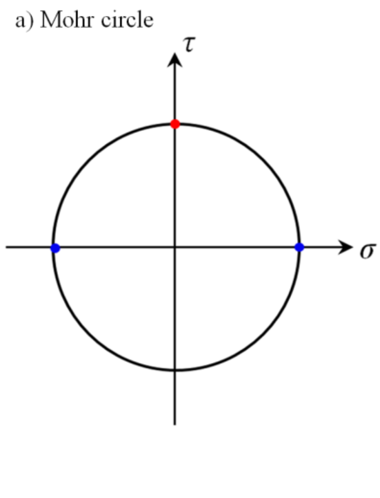

Figure 15. Two-dimensional pure shear.

(a) Morh circle (b) pure shear deformation (c) equivalent biaxial

3.5.2 Simple shear

Deformation due to simple shear is represented by Figure 16 (a). The boundary conditions equivalent to simple shear deformation are schematically shown by Figure 16 (b). The left and right sides of the two-dimensional element are constrained from displacement in x-direction but free to rotate. The left side cannot displace in y-direction while the right side can. The top and the bottom surfaces are free surfaces. If a shear force, *P*, is applied on the right side, the free body diagram of the element would be Figure 16 (c) where there is a reaction force and a moment. The moment is caused by the applied shear force, *P*, and the L_x acting as its moment arm. The moment causes distributed axial stress on the element, as shown in Figure 16 (d).

Therefore, the simple shear test leads to a stress state in which non-shear components are present. The stress tensor of the simple shear test is shown with the Eq (19). In order to achieve pure shear, the shear loads must be applied coaxially to eliminate the moment arm.

$$\bar{\bar{T}} = \begin{bmatrix} \sigma_x & \tau_{xy} \\ \tau_{xy} & 0 \end{bmatrix}. \tag{19}$$

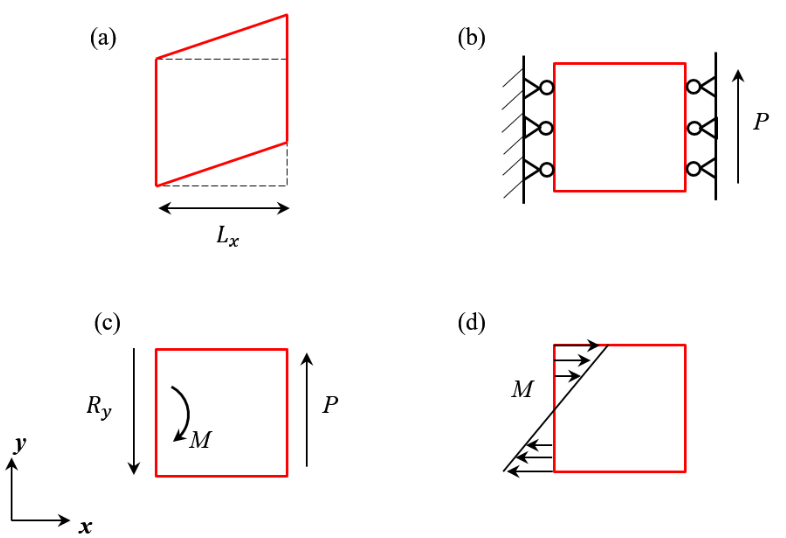

Figure 16. Two-dimensional simple shear deformation.

(a) simple shear deformation (b) boundary condition

(c) free body diagram (d) moment-driven axial stress

The presence of the moment in simple shear is revisited using the deformation gradient. Noting that the two-dimensional displacement field of Figure 16 (a) is,

$$u = 0. \tag{20}$$

$$v = C \cdot x. \tag{21}$$

where C is a constant, the resulting deformation gradient is,

$$\bar{\bar{F}} = \begin{bmatrix} \frac{\partial u}{\partial x} & \frac{\partial u}{\partial y} \\ \frac{\partial v}{\partial x} & \frac{\partial v}{\partial y} \end{bmatrix} = \begin{bmatrix} 0 & 0 \\ C & 0 \end{bmatrix}. \tag{22}$$

By decomposing the deformation gradient,

$$\bar{\bar{\bar{F}}} = \begin{bmatrix} 0 & \frac{c}{2} \\ \frac{c}{2} & 0 \end{bmatrix} + \begin{bmatrix} 0 & -\frac{c}{2} \\ \frac{c}{2} & 0 \end{bmatrix}. \tag{23}$$

where the first term indicates the pure shear and the second term indicates the rigid body rotation. The deformation gradient includes a component other than shear. Thus simple shear is different compared to pure shear. The rigid body rotation is due to the moment that was previously discussed, $M = P \cdot L_x$. (Note that the above deformation gradient is formulated under infinitesimal strain theory, merely to indicate the presence of the rotation. This definition of deformation gradient is not applicable when considering large deformation in a body.)

4. Uniaxial Tensile Test

The tensile test is an appropriate initial approach for analysis of EA9361 both quantitatively and qualitatively. The tensile stress/strain relation, yield stress, failure strength and strain are to be quantified. Optically measuring the displacement field of the sample's gage section in both longitudinal and transverse directions, one is also able to approximate the Poison's ratio. Any qualitative observations leading to further understanding of flexible epoxy adhesives and joint design are to be discussed.

4.1 Methodology

4.1.1 Sample preparation

The tensile test is prepared and performed based on the ASTM D638 standard. In order to produce specimens with uniform thickness, a plate of the adhesive is manufactured. Table 2 indicates that EA9361, a two-part paste adhesive, is very viscous. To accomplish homogeneous and void-free mixing, the two parts are mixed inside a Thinky Mixer ARE-310. The mixer, operating at 2,200 rpm for thirty seconds to one minute, is able to perfectly mix EA9361. The exact operating duration can be determined by trial-and-error depending on the size of the mixing container and the quantity of the adhesives to be mixed. It is recommended that the two parts are first hand-mixed with a spatula. Without the hand-mixing, full mixing process has to be done in the rapidly spinning mixer for longer period of time. This may lead to unnecessary heat generation because the high rpm accelerates the exothermic reaction. And gelation may initiate during the mixing. The undesired heat generation is more pronounced when larger quantities of adhesive are mixed. During the plate manufacturing, 25 to 30% of excess quantity over the exact amount for one plate is mixed because some adhesive stick to the container due to high viscosity.

The mixed adhesive is compression-moulded using a hot press. The mould is made of Aluminum 6061 and the moulding surface is machined and polished to a mirror finish. Appendix II shows the detailed design of the mould. The ASTM D638 standard suggests to achieve specimen thickness of 3.175 mm (equivalently 1/8 inches). Therefore, a silicone rubber sheet with the same thickness is purchased. The silicone rubber sheet is carefully chosen, with high temperature resistance and high hardness. Temperature resistance is necessary for its exposure to high temperature in the hot press, and the hardness for dimension control. Figure 17 (a) shows the assembled mould and the silicone frame. A hydrostatic pressure of 2MPa is mechanically applied by the press, as shown in Figure 17 (b). The accelerated cure, recommended by the manufacturer as seen in Table 2, is performed at 82°C for an hour. After the cure, the manufactured plate is found to have an average thickness of 3.277 ± 0.025 mm. Better thickness control is not feasible due to the silicone rubber sheet's thickness tolerance of 3.175 ± 0.43 mm. The thickness control of the plate can be improved if a precisely machined metallic frame replaces the silicone frame. If metallic frame is to be used, it is essential to properly release the frame so that the adhesive does not stick to it.

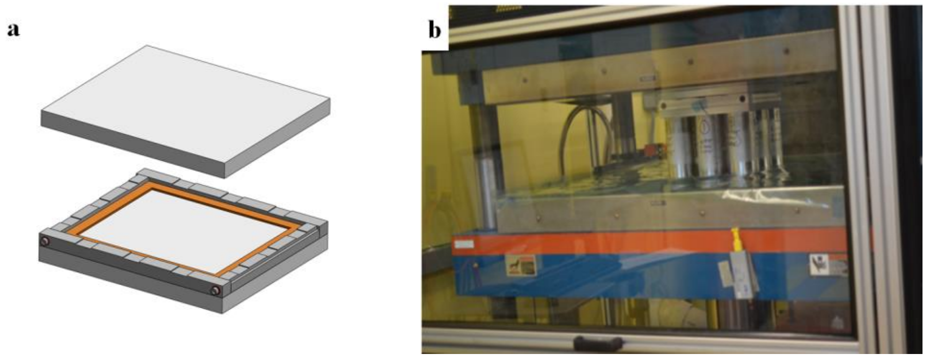

Figure 17. Compression mould and the hot press.

Once the plate is cured, it is cut and machined into the shape and the dimension of type I specimen of ASTM D638 standard indicated by Figure 18. The plate is manually hand-machined by a router that cuts the plate along a pre-machined profile that has the same shape as the specimen. Then the gage section of the sample is painted with a speckle pattern. Painting the speckle pattern is a necessary step during the manufacturing because the strain will later be measured by digital image correlation, which is to be abbreviated as DIC in the rest of this thesis. A white background with black speckles is painted; the white background with black speckles produces more accurate strain measurement than a black background with white speckles, as seen during the preliminary post-processing. The speckles are manually dotted on the gage section of the specimen with an ink pen, which achieves the control of the speckle size between 0.5 to 1 millimetres in diameter. Spraying, although time efficient, is avoided because the former achieves more consistent speckle size. The process of removing the plates from the mould, cutting, machining and painting the specimens is visually summarized in Figure 19 (a), (b), (c) and (d). Also, Figure 19 (e) is the close-up view of the speckle pattern on a specimen.

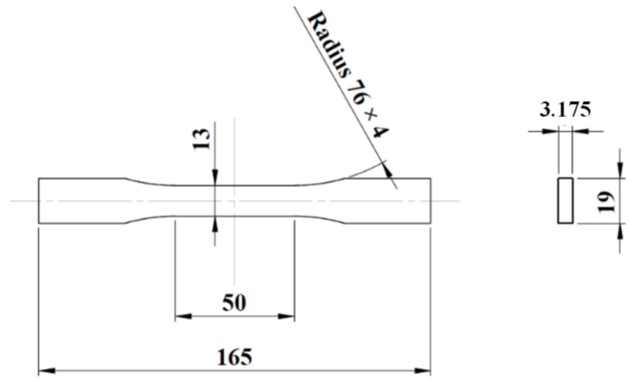

Figure 18. The dimensions of the type I specimen of ASTM D638 standard in millimetres.

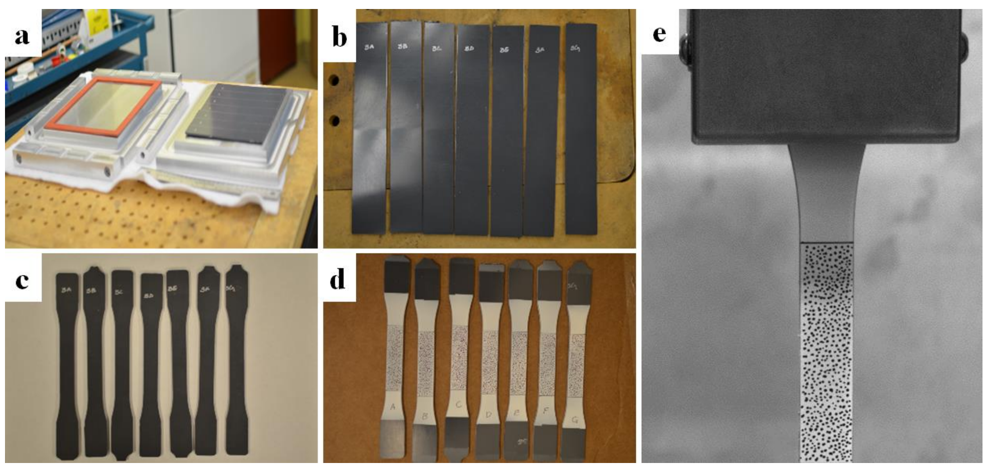

Figure 19. Tensile tests specimen preparation: curing, cutting, machining and painting.

4.1.2 Experimental procedure

Figure 20 is a schematic of the experimental set-up. The specimens are mounted on the Insight 5kN MTS machine with wedge clamp grips. Clamping by hand is sufficient to clamp the samples so that they stay well fastened throughout the tensile elongation. The MTS machine measures the force with a noise level of ± 0.5 N. Simultaneously, the camera, a PointGrey Flea 5MP, takes images of the speckled gage section. The DIC technique is used for strain measurement because strain developed during the test of the EA9361 is too large for strain gages or extensometers.

The force measurement and image capturing are performed at 1 Hz. While it is feasible to have higher frequency for the MTS, the frequency of the camera is limited due to the lack of space to store the image files. Nevertheless, the preliminary experiments show that using a higher sampling rate does not improve the accuracy of the strain measurement. The head displacement rate is 2.5 mm/min. This rate is intentionally set half as fast as in the ASTM D638 recommendation, in order to reduce the viscous response of the adhesive. At this head speed, the test is initiated with a strain rate of 0.05 per minute.

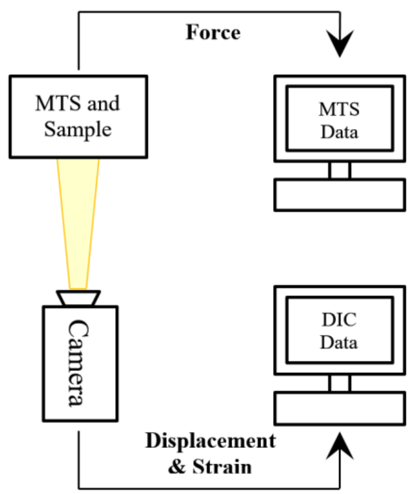

Figure 20. Schematic of the data acquisition system.

4.1.3 Post-processing

The DIC technique employs the commercial software Vic-2D for post-processing the captured images. The DIC is capable of measuring displacements in the transverse direction as well as in the longitudinal direction. As the displacement in the transverse direction is measured, the instantaneous width of the specimen's gage section is known. In the thickness direction, the sample is assumed to contract by the same proportion as in the width direction because EA9361 is isotropic. The instantaneous cross section area of the specimen is calculated to be the product of the instantaneous width and the thickness. With the force reading from the MTS and the calculated instantaneous area, the true stress is calculated with Eq (2).

Based on the displacement field throughout the speckled area captured by the camera, Vic-2D calculates and outputs engineering strains. These engineering strains are then converted to true strain by Eq (11), then are averaged to a single value. The Poisson's ratio is approximated by Eq (14) with the calculated average true strains between two consecutive images.

4.2 Results

Figure 21, Figure 22 and Figure 23 show the force/displacement, stress/strain and Poisson's ratio respectively from the tensile tests. It is observed from Figure 22 that the elastic region has tensile modulus of 514 MPa and the plastic region has a reduced modulus of 28 MPa. All the samples failed in the gage section with net section failure mode. The failed samples are shown in Figure 24 and their failure stresses and strains are summarized in Table 4. The Sample F (the sixth sample from the left in Figure 24) seems to fail outside the gage section. However, its failure is within the gage section, but outside of the area where the speckles are painted. This particular sample has higher failure strength than the minimum of the seven samples. Also contained in the Table 4 is the permanent strain observed in the failed samples after full shrinkage overnight after the experiments. Over the large elongation, the value of Poisson's ratio changed starting from $\upsilon = 0.44$, increasing upto $\upsilon = 0.47$, and then decreasing down to $\upsilon = 0.38$ before failure.

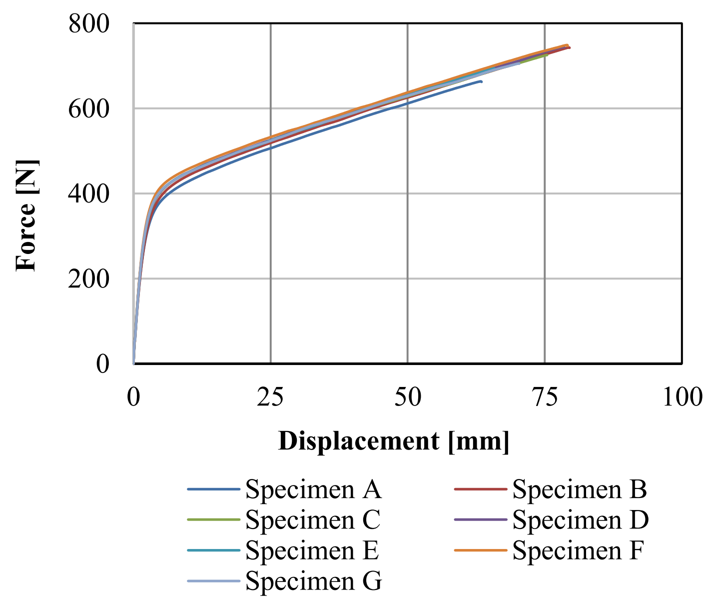

Figure 21. EA9361 tensile tests: force vs displacement.

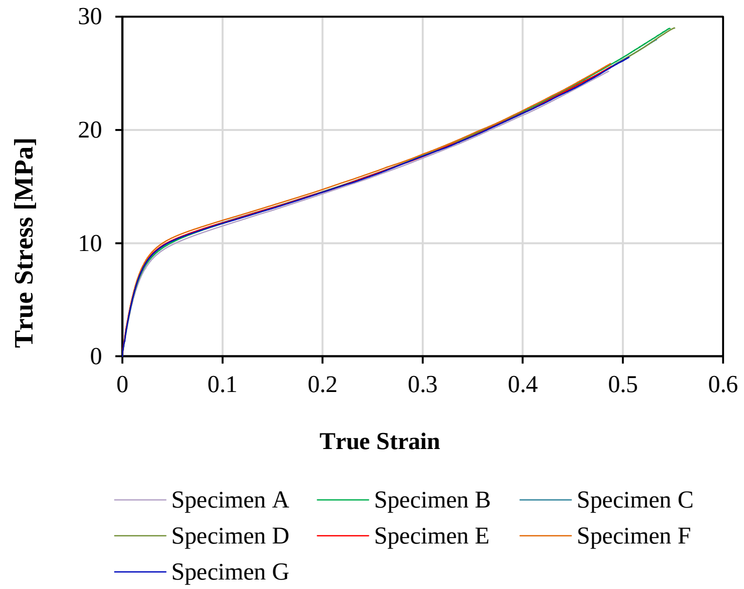

Figure 22. EA9361 tensile tests: stress vs strain.

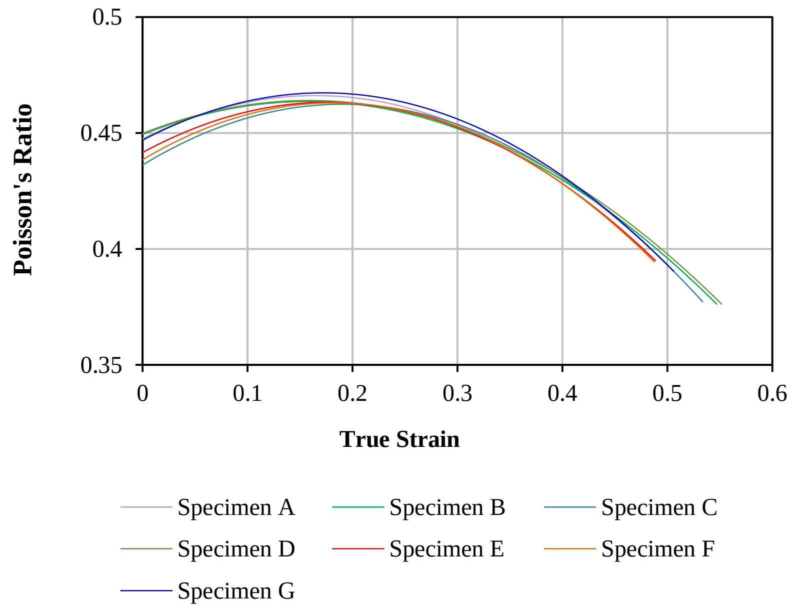

Figure 23. EA9361 tensile tests: Poisson’s ratio vs strain.

Figure 24. EA9361 tensile tests: failed specimens showing net-section failure.

Table 4. EA9361 tensile tests: failure stress and strain, and permanent strain.

	Failure Stress [MPa]	Failure Strain	Permanent Strain
A	25.30	0.49	0.071
B	28.90	0.56	0.097
C	28.00	0.53	0.071
D	29.00	0.55	0.089
E	25.70	0.49	0.071
F	29.10	0.55	0.089
G	26.50	0.51	0.105

4.3 Discussion

For both stress/strain and Poisson's ratio, the seven samples had precisely matching results as evident from Figure 22 and Figure 23. The precision confirms that the manufacturing method properly achieved uniform mixing and curing for each sample.

4.3.1 Distinct yielding and bilinear simplification for stress/strain relation

Distinct yielding is observed from the stress/strain curves. Beyond the point of yielding, the stiffness sharply reduces. The two segments of the curve before and after the yielding are nearly linear. Based on this observation, the nonlinear stress/strain curve can be approximated using a bilinear model. With the bilinear simplification, it becomes feasible to analyze structures with flexible adhesives found in semi-analytical models. An example could be the semi-analytical model developed by Bodjona [40] to analyze a hybrid bonded/bolted joint with a flexible adhesive, in which the bilinear simplification is used.

4.3.2 Poisson's ratio, and its effects on joint design

The value of Poisson's ratio changes with increasing strain. During the testing, the maximum Poisson's ratio found was 0.47 and the minimum was 0.38. The measured Poisson's ratio is higher than that of polyurethane and rubber-toughened adhesives [22] as well as most metallic and non-metallic materials (besides rubber). The difference between the maximum and minimum is 0.08, which is a significant difference considering that the possible range of Poisson's ratio for common isotropic materials is $0 < \upsilon_{\text{iso}} < 0.5$.

Understanding high and varying values of Poisson's ratio is crucial when designing bonded joints with flexible epoxy adhesives. Firstly, high Poisson's ratio can produce stress concentrations in the adhesive. In a joint, the adhesive bondline is very thin. The bondline of adhesive under peel stress will elongatee in the thickness direction. The Poisson's effect causes the adhesive to contract in other directions, but this contraction is constrained by the adherends. Not being able to contract, the adhesive develops a severe stress concentration. This stress concentration due to the Poisson's effect is more pronounced with higher values of Poisson's ratio. Furthermore, for a flexible adhesive, the constraint effects are further amplified due to higher relative modulus difference between the adhesive and the adherends: the more relatively stiffer the adherends, the more constrained the adhesive is, therefore higher the stress concentration.

Discovering the varying values of Poisson's ratio presents a challenge to modelling failures of flexible adhesive. So far, FE is considered an appropriate tool for analyzing joints with a flexible adhesive, since it can simulate both the nonlinear material properties and large deformation. Proper nonlinear FE analysis of a flexible adhesive requires taking varying values of Poisson's ratio as an input material property at different time steps, or load levels. This is a problem, because in general, commercial FE packages account for only a single constant value of the Poisson's ratio.

4.3.3 Material model selection

As a result of yielding, there is some permanent deformation in the samples as shown by Table 4. Certain flexible adhesives have previously been modeled with hyperelasticity. [21, 22] Although hyperelasticity can be used to model large deformation, the inherent plasticity of the flexible epoxy adhesive does not fit with the fully elastic properties of a hyperplastic material. Also, the measurement of Poisson's ratio showed that EA9361 is compressible, whereas hyperelasticity is formulated based on an assumption of incompressibility. Therefore, the present study recommends the use of elastic/plastic bilinear model with a yield surface. The elastic/plastic bilinear model is also compatible with the bilinear simplification discussed in Section 4.3.1.

4.4 Stress/Strain Curve Fitting: Hyper Elasticity vs Bilinear Elastic/Plastic

When using the experimental data as an input to an FE model, the stress/strain is one of the most significant material properties. In order to imitate the material's response accurately, one has to identify the most appropriate material model. While this study recommends the use of bilinear material model for flexible epoxy adhesives, the hyperelastic model is also commonly used as discussed in the literature review in Section 1. Section 4.4 is dedicated to investigating the capacity of the two models to fit the EA9361's data.

Hyperleasticity derives the stress/strain relation using the strain energy density function, E, under the assumption that the material is incompressible. [22] Using the strain energy density function, stress is formulated in terms of stretches as below.

$$\sigma_{i_{Eng}} = \frac{\partial E}{\partial \lambda_i} \tag{24}$$

$$\sigma_{i_{True}} = \lambda_i \frac{\partial E}{\partial \lambda_i} \tag{25}$$

There exist different hyperleastic models; examples of which are Mooney-Rivlin, Ogden, Polynomial, Saint Venant-Kirchoff and others. The previous attempts to use hyperelastic models most often employ the Mooney Rivilin model. [41, 42] This study also uses Mooney-Rivlin model to describe the hyperelasticity for comparison with the bilinear model. The Mooney-Rivlin formulation of strain energy density function is expressed below by Eq (26) where C_{ij} is a constant and the $I_1 = \lambda_1^2 + \lambda_2^2 + \lambda_3^2$, and $I_2 = \lambda_1^2\lambda_2^2 + \lambda_2^2\lambda_3^2 + \lambda_3^2\lambda_1^2$ are the invariants of the left Cauchy-Green deformation tensor.

$$E_{MR} = \sum_i \sum_j C_{ij}(I_1 - 3)^i (I_2 - 3)^j \tag{26}$$

For the curve fitting in this study, the strain energy density function of the Mooney Rivlin model is expanded to third order polynomials as shown below.

$$E_{MR} = C_{10}(I_1 - 3) + C_{01}(I_2 - 3) + C_{11}(I_1 - 3)(I_2 - 3) + C_{20}(I_1 - 3)^2 + C_{30}(I_1 - 3)^3 \tag{27}$$

The constants are solved with the simplex algorithm [43], that are available in MS Excel, so that the best-fitting curve generated by Mooney-Rivlin formulation is obtained.

The bilinear model, which consists of two lines, can be constructed if three points are given, as seen by Figure 25. The first point, the undeformed state, has known coordinates which are zero stress and zero strain. Therefore, if the two coordinates at yielding and at failure are known, the two lines are generated. The simplex algorithm is used again to solve for the four unknowns: yield stress, yield strain, failure stress and failure strain.

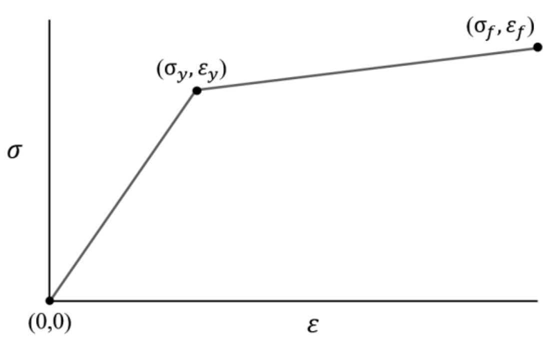

Figure 25. Bilinear model curve fitting

The fitting is performed three times in three different strain ranges: $[0 < \varepsilon < 0.5]$, $[0 < \varepsilon < 0.3]$ and $[0 < \varepsilon < 0.1]$ for EA9361. Figure 26 shows the results of the curve fitting with the two models. The curve from the experiment found in Figure 26 is the average of the seven specimens' results from the tensile tests. Table 5 lists the coefficient of determination of each fitting performed.

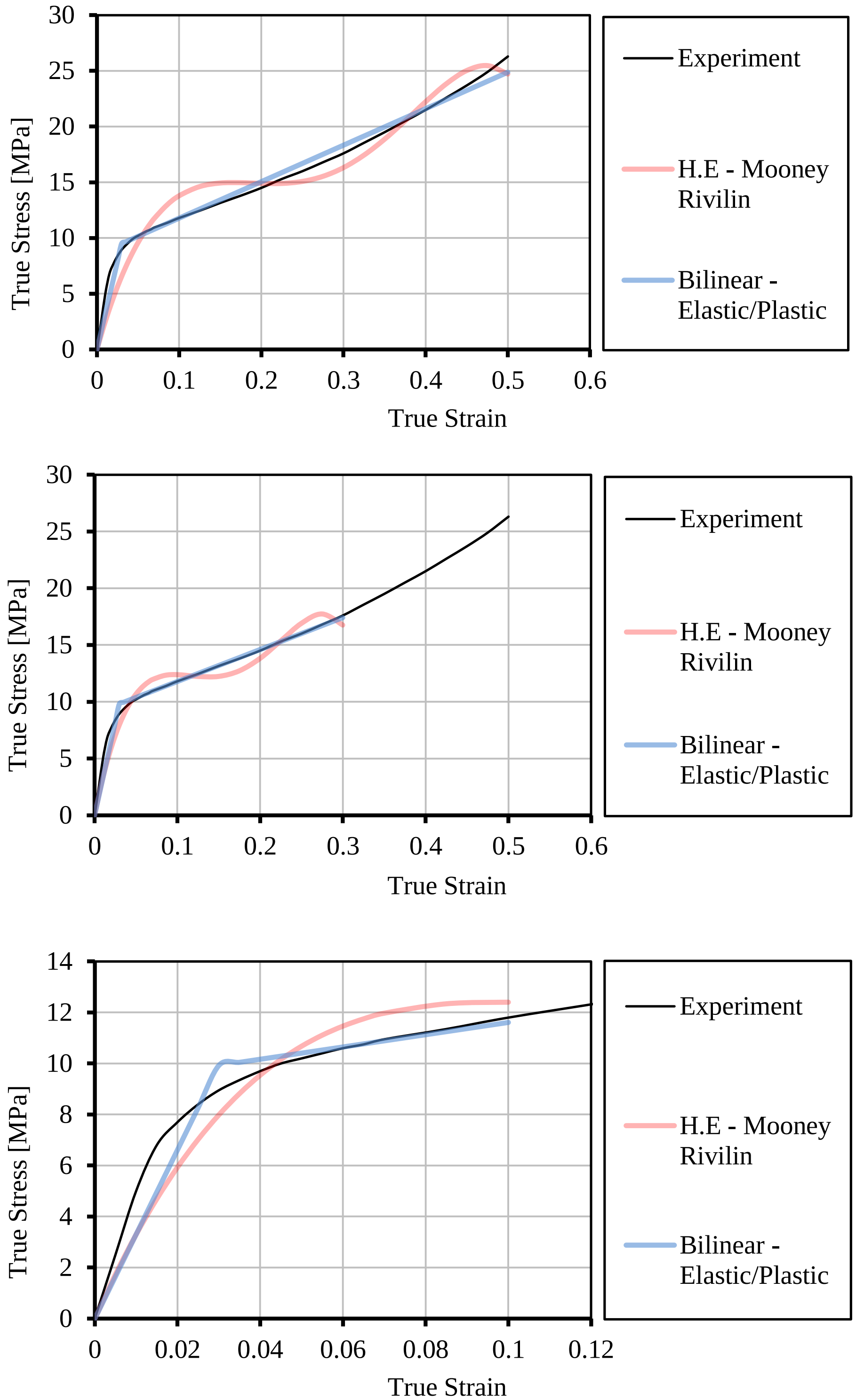

Figure 26. EA9361 tensile tests: curve-fitting.

Top: Fitted to $0 < \varepsilon < 0.5$, Middle: Fitted to $0 < \varepsilon < 0.3$, Bottom: Fitted to $0 < \varepsilon < 0.1$

Table 5. EA9361 tensile tests: curve-fitting.

Strain range fitted	Coefficient of Determination, R^2	
	Hyperelastic Mooney-Rivlin	Bilinear Elastic/Plastic
$0 < \varepsilon < 0.5$	0.94	0.99
$0 < \varepsilon < 0.3$	0.96	0.98
$0 < \varepsilon < 0.1$	0.97	0.98

Qualitatively speaking, the hyperelastic model has several peaks in the curve due to the nature of the polynomial fit. Consequently, there are several regions that overshot and undershot the experimental data of EA9361. Also, as the curve has to be smooth and continuous for a polynomial, it is clear from Figure 23 that the Mooney Rivlin model is unable to accurately fit the sharp slope charge at the location of yielding. As the strain range gets larger, the slope change becomes relatively more abrupt. Consequently, as shown in Table 5, the coefficient of determination worsens from 0.97 to 0.94. In contrast, the bilinear model does not produce any significant overestimation or underestimation. Its coefficient of determination remains at 0.98 or higher, validating the accuracy of the fit. Therefore, it is concluded that use of a bilinear model better fits the results from EA9361. Similar results are expected for flexible epoxy adhesives in general.

In addition to EA9361, two other flexible adhesives are fitted with both material models for comparison: Tensorgrip M70 and Pilogrip 7400/7410. The results of the fittings are presented in Figure 27 and Figure 28. The true stress/strain curve of M70 is nearly straight throughout the strain range until failure, and both hyperelastic and bilinear models are able to fit M70 accurately. Pilogrip 7400/7410 had nonlinear stress/strain but not a distinct yielding. Hyperelasticity fits Pilogrip 7400/7410 better than EA9361, but there were are regions where the stress is overestimated or underestimated.

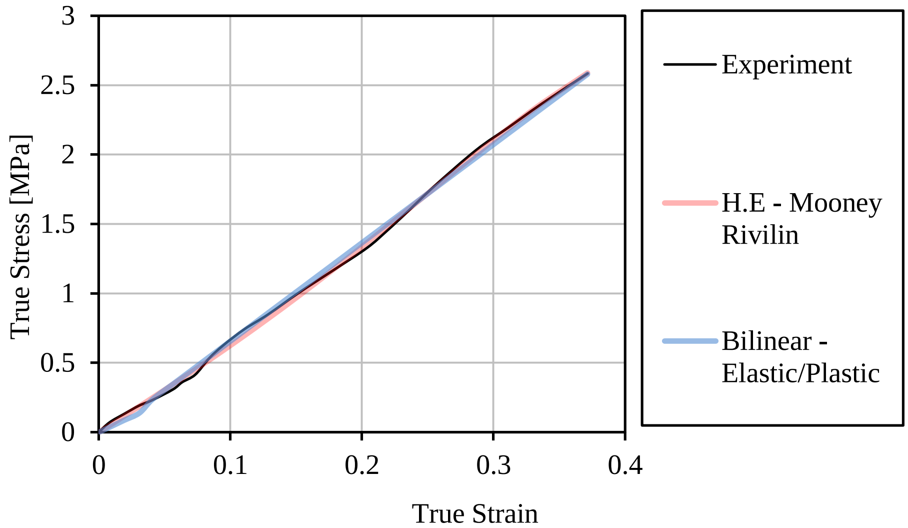

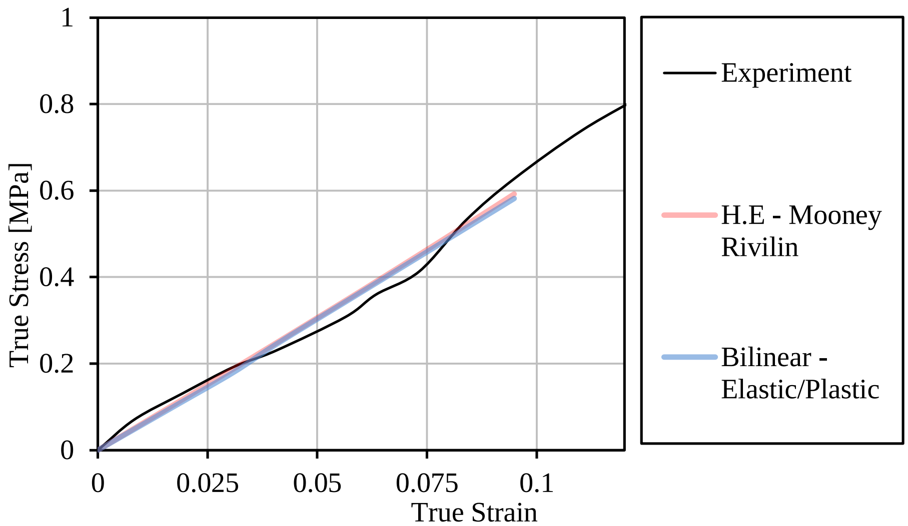

Figure 27. M70 tensile tests: curve-fitting.

top: fitted to $0 < \varepsilon < 0.47$, middle: fitted to $0 < \varepsilon < 0.3$, bottom: fitted to $0 < \varepsilon < 0.1$

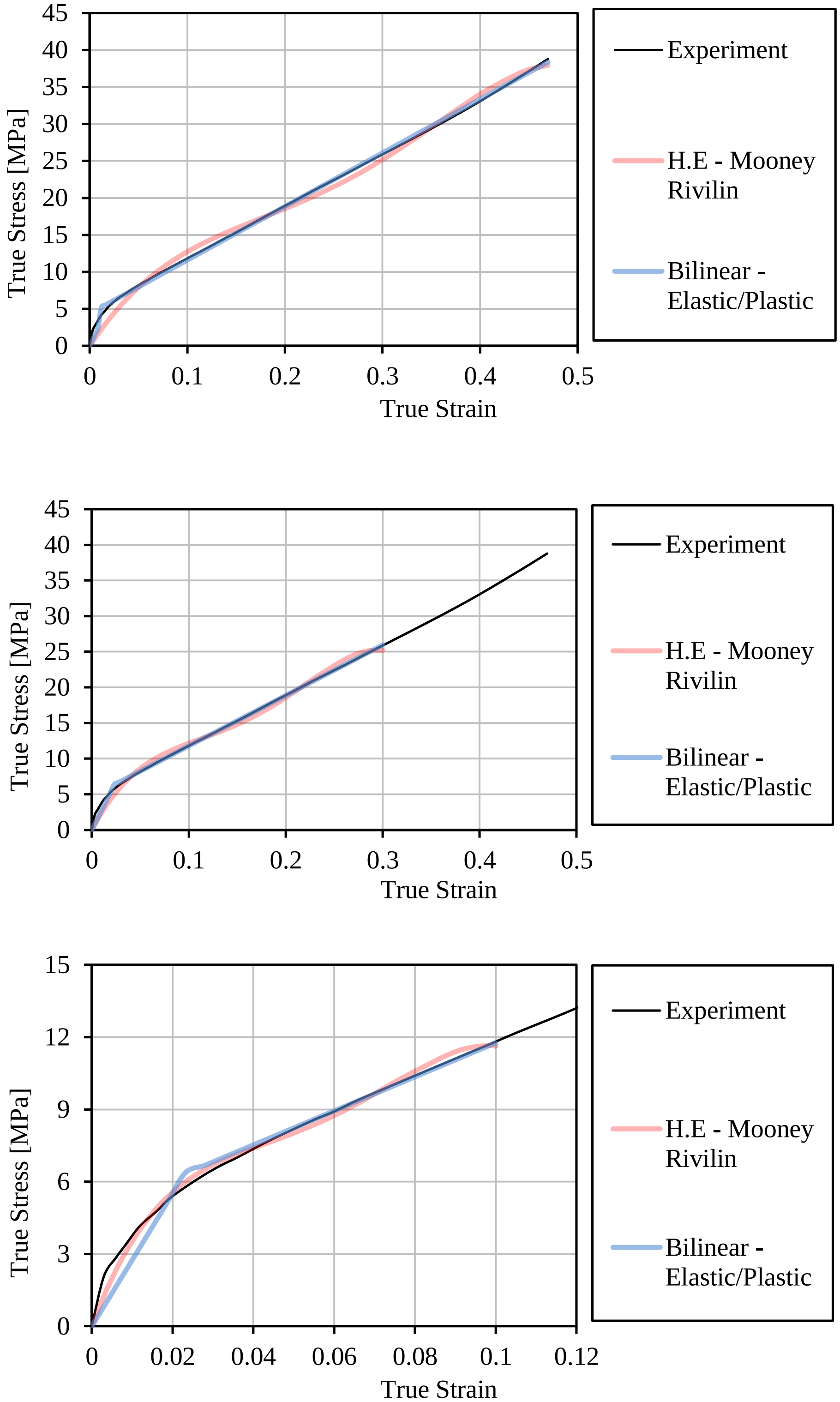

Figure 28. PiloGrip 7400/7410 tensile tests: curve-fitting.

top: Fitted to $0 < \varepsilon < 0.47$, middle: fitted to $0 < \varepsilon < 0.3$, bottom: fitted to $0 < \varepsilon < 0.1$

5. Biaxial Testing

As pronounced yielding is detected from the tensile tests, biaxial tests follow to measure yielding at various orientations of biaxial loads. Afterwards, one can attempt to fit the measured yield stresses into a yield surface model. This effort is motivated by the work of Wang [44], who has performed his tests using an Iosipescu fixture on film epoxy adhesive, FM73. The Drucker-Prager cap model, formulated and offered by ABAQUS, successfully fits Wang's test results. A similar approach is taken to investigate the yielding behaviour for EA9361 in this study. A custom-designed Arcan fixture is used to apply the biaxial loads. The Arcan fixture is able to apply pure shear while common standard tests such as ASTM D5656, Thick Adherend Shear Test, involves simple shear. Therefore, this test intends to capture the shear stress/strain relations as well as the yield stresses. V-notched specimens, manufactured from a custom-designed bonding jig, are used. Uniform pure shear could be attained in the adhesive through the use of these V-notched test specimens, similar to why the Iosipescu shear test, ASTM D5379, employs them.

5.1 Methodology

5.1.1 Sample preparation

The appearance of the V-notched specimen is displayed in Figure 29 (a) and the way a specimen is mounted on the fixture is depicted by Figure 29 (b). The specimen consists of two Aluminum 6061 adherends are bonded by EA9361. The adhesive thickness is targeted to be manufactured at 0.5 mm. The dimensions of the adherend are shown in Figure 30 (a). Also, Appendix III shows the detailed drawing of the specimen.

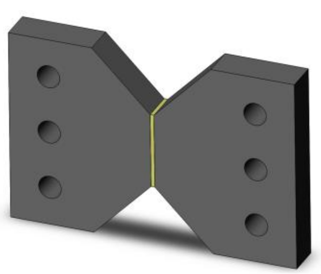

a) V-notched specimen

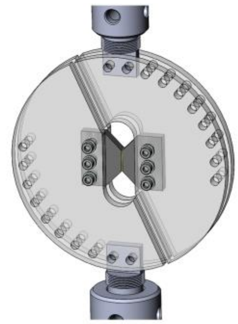

b) Arcan fixture

Figure 29. V-notched Specimen.

In order to manufacture the specimens with accurate adhesive thickness, a bonding jig is designed. Appendix IV shows the detailed design of the jig. Prior to placing the specimens in the jig, the bonding surface of the specimen is surface-treated. The surface treatment starts with cleaning all surfaces with soft cloth and dilute acetone 2-3 times. Then, the bonding surface is cleaned again using FreshStart, a mold cleaning agent provided by Zyvax. Cleaning with FreshStart is repeated until a water free surface is achieved (FreshStart is able to completely remove all contaminants. While applying FreshStart with white cloth, one can notice the cloth turning grey. The grey color comes from broken oxide layer of the aluminum surface that is wiped off by the cloths. Breaking the oxide layer confirms sufficient cleaning. Nevertheless, when exposed to air, oxide layer would instantly form again on the aluminum surface) Lastly, the 3M AC-130 pre-treatment solution is applied on the bonding surface.

Following the surface treatment, the specimen manufacturing is performed. On the base plate, the jig is placed, as seen by Figure 30 (b). Then the bottom specimens are fixed to the jig by thumb screws. While the jig is tilted, mixed adhesive from the Thinky Mixer is injected into the jig, onto the bonding surface of the specimen. Then the top specimens are placed and fixed with thumb screws, as shown by Figure 30 (c). The lid is closed, and then the jig assembly is clamped. (Figure 30(d))

The adhesive in the jig is then to be cured inside an oven. The preliminary manufacturing shows that the single-dwell cure at 82°C, used to cure the tensile test specimens, results in the adhesive leaking through the gap and escaping from the jig. The sudden rise in temperature to 82°C sharply reduced the viscosity, allowing the thin adhesive to flow between the gaps before gelation occurred. Therefore, the two-dwell cycle is designed: the first dwell at 50°C to harden the epoxy adhesive without leakage, and the second dwell at 82°C to fully cure the adhesive. The graph of the two-dwell cure cycle is shown in Figure 31. At the end of the cure cycle, which has no ramp-down, the bonding jig was taken out of the oven immediately.

After the cure, the adhesive thickness was found to be 0.6 mm ± 0.08. Although adhesive leakage is avoided by the new cure cycle, some excess adhesive is still present at the gap between the jig and the specimen. This trapped excess adhesive is considered to be the major reason for thickness being slightly greater than the targeted value of 0.5 millimeters.

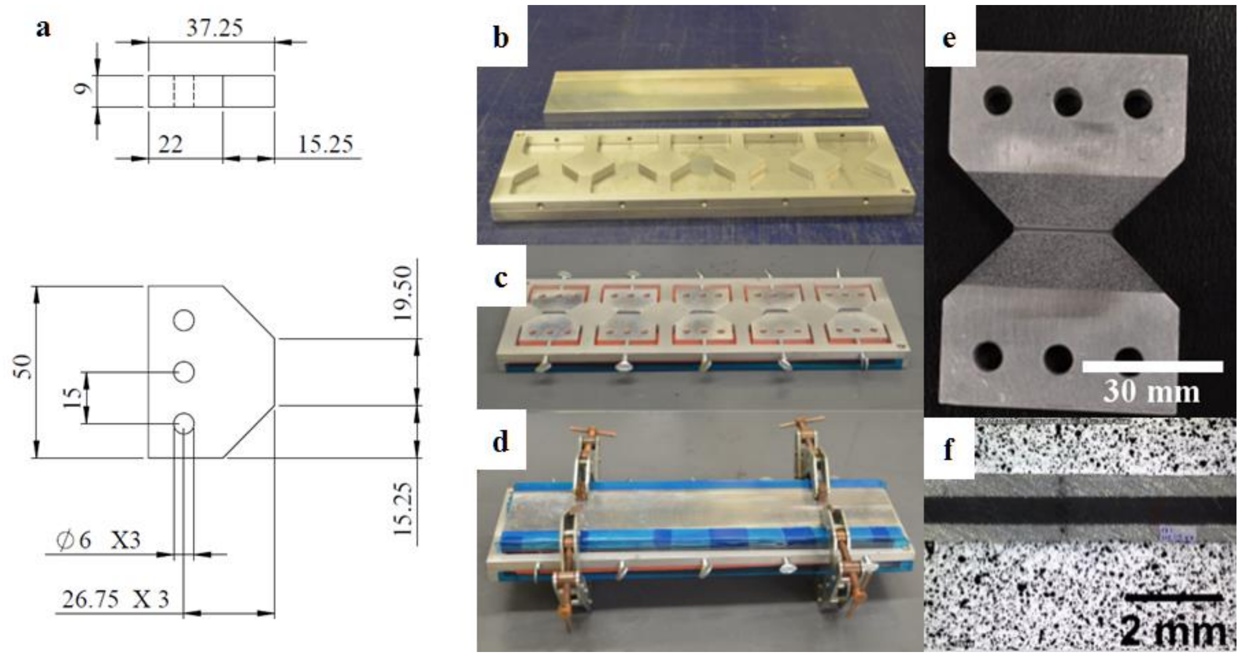

Figure 30. V-notched specimen.

(a) specimen dimensions, (b) curing jig, (c) specimens placed in jig (d) jig ready for oven cure, (e) specimen with speckle pattern, (f) close-up of speckle pattern around adhesive

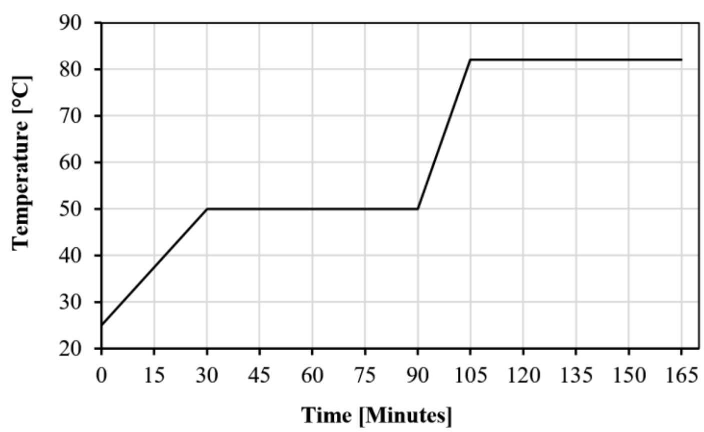

Figure 31. Two-dwell cure cycle for EA9361

The last part of the preparation is painting the speckle pattern onto the specimens. In order to produce small speckle size on the order magnitude of the adhesive thickness, an airbrush technique is used. Figure 30 (e) and (f) show the painted specimen and the close-up view of the speckle patterns.

5.1.2 Experimental procedure

The bonded specimen is first attached rigidly to the fixture by six bolts. The rotation of the fixture allows changing the orientation of the specimen and thus the ratio of biaxial loads on the adhesive, described by Figure 32. The detailed design of the Arcan fixture is presented in Appendix V. Similar to the tensile test, the Insight 5kN MTS measures the forces and the PointGrey Flea 5MP camera captures the images for DIC. Both measurements are taken at 1 Hz. The head displacement rate is adjusted so that strain rate is the same as the tensile test from Section 4.1.2. The specimens are tested at five different orientations, each with five repetitions. The tested loading orientations are presented in Table 6.

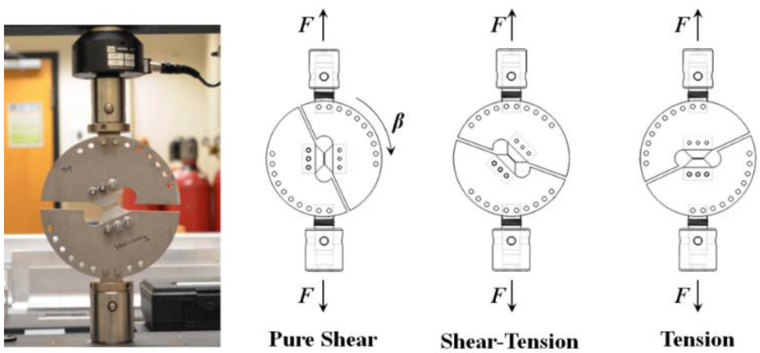

Figure 32. Arcan fixture and the shift of loading orientation.

Table 6. Biaxial tests: loading orientations.

Loading Orientation	β [Degree]
Tension	0°
Tension Dominant	22.5°
Combined	45°
Shear Dominant	67.5°
Pure Shear	90°

5.1.3 Post-processing

Stress approximation

The modulus of the aluminum adherends are two orders of magnitude greater than that of the flexible adhesive, EA9361. The deformation of the adherends is negligible throughout the testing. Therefore, relative to the adhesive, the adherends are assumed to be rigid. Then, the adhesive at the interface is unable to deform as they are attached to the adherends. The adhesive thickness is so thin that the other parts of the adhesive are also significantly constrained. Consequently, the change in cross section area is negligible. And the constant value of the cross section area, which equals the area of the bonding surface, is used to calculate the stress, using Eq (1) and (5).

Strain approximation

It is impractical to apply white paint, serving as the background color, onto the very thin bondline of the adhesive. After painting white on the adhesive bondline, spraying minuscule speckles onto it is an even greater challenge. If the speckle size is not comparable with bondline thickness, it could affect the accuracy of the strain approximation by DIC. Figure 30 (f) shows that the adhesive itself is not painted with speckles. Instead, the adherends are painted. This is because this study intends to measure the adhesive strain by tracking the two adherends' relative displacement. This method to measure strain is named the *Adherends Relative Displacement* technique, or shortly ARD method.

As shown in Eq (6), the engineering strain formulation defines the axial strain to be the ratio of the change in the length, ΔL, over the initial lengths, L_o, of a stress element. Therefore, if the equivalence of the ΔL and L_o are specified, the calculation of the engineering strain is possible. In order for the strain approximation, it is assumed that uniform displacement field is found on each adherend. This is a valid assumption as the adherends are two orders of magnitudes stiffer than the adhesive, therefore the strain developed in the adherends are negligible. Under this assumption the relative displacement of the two adherends in the axial direction (x-direction with respect to Figure 33 (a)) equals the change in the thickness of the adhesive, $u_r = \Delta t$. If the stress element is taken to be the adhesive whose length starts from one interface to the opposite interface with the adherends, then the length of the stress element, L, becomes the adhesive thickness, t. Then, as Δt and t replace ΔL and L in Eq (6), the ARD method approximates the adhesive's engineering strain in the axial direction to be Eq (28). Then, as Eq (28) is substituted into Eq (11), the approximation of the true stress is achieved to be Eq (29).

The relative displacements of the adherends in the y-direction, v_r, along with the adhesive thickness forms the angular deformation, $tan(\theta) = \frac{v_r}{t}$. Therefore, using the Eq (12) and (13), the engineering and the true shear strain is calculated to be Eq (30) and Eq (31) respectively.

$$\varepsilon_{xx_{Eng}} = \frac{\Delta t}{t} = \frac{u_r}{t} \tag{28}$$

$$\varepsilon_{xx_{True}} = \ln(1 + E_{xx_{Eng}}) \tag{29}$$

$$\varepsilon_{xy_{Eng}} = \frac{dv}{dx} = \frac{v_r}{t} \tag{30}$$

$$\varepsilon_{xy_{True}} = arctan\left(\varepsilon_{s_{Eng}}\right) \tag{31}$$

In order to validate the strain measurement technique, the strain approximation is compared between the proposed ARD method and direct DIC processing on the bondline of the adhesive. For this comparison, the tested specimen is painted both on the adhesive (with some difficulty) and on the adherends. The painting of this specimen is shown in Figure 33 (b). A pure shear loading case is used for simplicity rather than using biaxial loading. In order to process the strain measurement, the speckled adhesive surface is subjected to direct strain calculation by DIC, and the speckled adherends' surfaces are subjected to the ARD methodology. Figure 34 compares the strain measurements from the two methods. As a sign of the difficulty associated with painting the thin bondline, there is a scatter in the results of the direct DIC method. For strain values for $\varepsilon_{xy} > 0.2$, the proposed methodology visibly underestimates the strain, and the magnitude of underestimation increases with increasing strain as seen by Figure 34. However, the error is controlled within 5% when the percent difference is calculated. The discontinuity at $\varepsilon_{xy} > 0.43$, is due to the failure of the adhesive. The least square technique calculates the coefficient of determination, for the range of $0 < \varepsilon_{xy} < 0.43$, to be $R^2 = 0.994$ between the two techniques. From the calculation of the percent difference and coefficient of determination, it is verified that the proposed methodology is valid for measuring strains in a thin bondline.

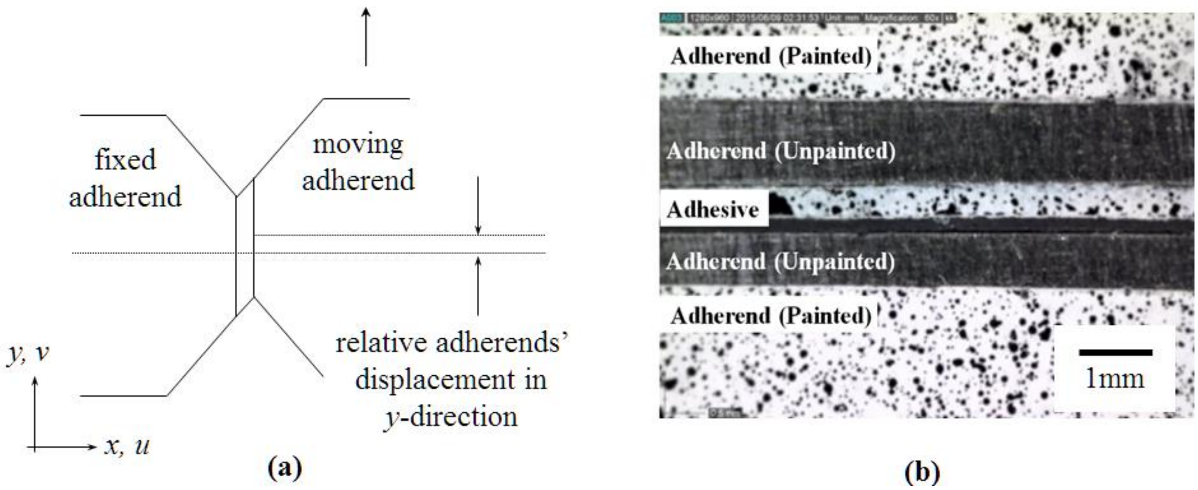

Figure 33. Strain measurement by ARD method.
(a) ARD method schematics (b) Preliminary test specimen

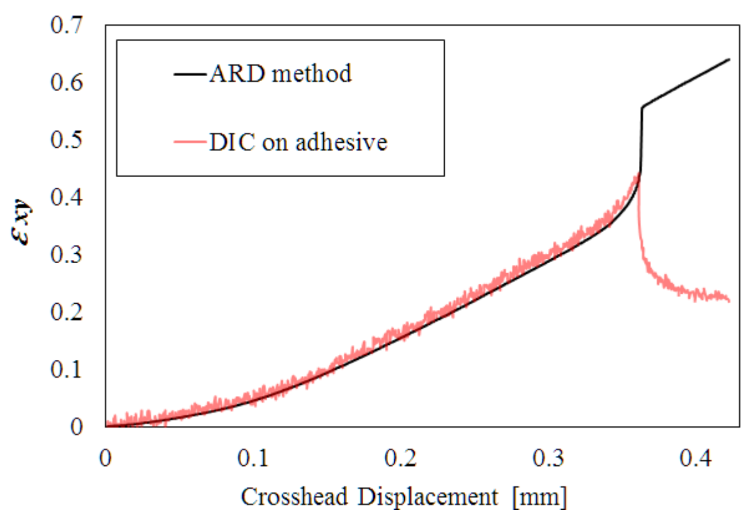

Figure 34. ARD method validation.

5.2 Results: Biaxial Testing

All specimens failed by cohesive failure, indicating that the surface preparation technique is appropriate. The failed specimens are shown in Figure 35. One can observe that there is still some adhesive on both bonding surfaces for each pair of adherends.

Figure 36 shows the experimental stress strain results for the pure shear case. Similar to the tensile tests, distinct yielding is observed. Yield stress under shear is observed to be $\tau_y = 8.3\ \mathrm{MPa}$ In the elastic region, the shear modulus is found to be 174 MPa, and in the plastic region the shear modulus is reduced to 25 MPa. Table 7 summarizes the failure stresses and strains under pure shear. Although failure from the tensile tests occurs instantly by net section failure, the shear test has gradual failure with the initial crack slowly propagating along the bondline.

Figure 37 summarizes the yielding captured at different orientations of biaxial loads. Also shown in Figure 37 is the best-fit curves generated by least-square fitting using Von Mises and Tresca models. Neither Von Mises and Tresca models are able to fit the measured yield stresses properly. The value yield stress for the pure shear case seems particularly high compared to other measured yield stresses.

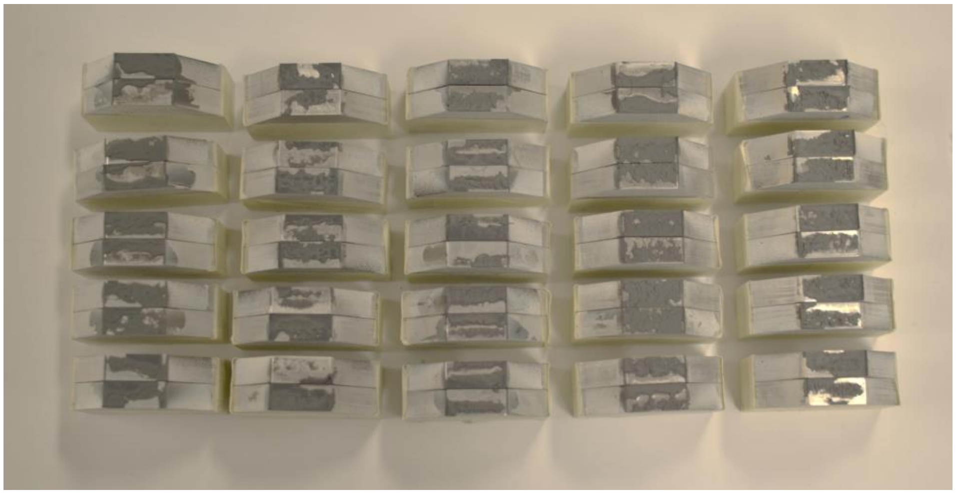

Figure 35. Failed V-notched specimens.

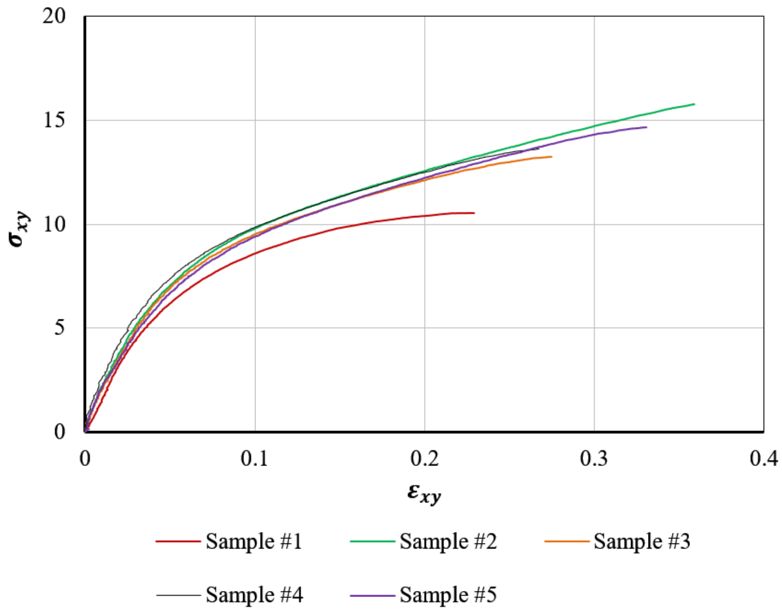

Figure 36. Pure shear tests: stress vs strain.

Table 7. Pure shear tests: failure stress and strain.

Specimen #	Failure Stress [MPa]	Failure Strain [θ]
1	10.5	0.22
2	15.8	0.36
3	13.8	0.27
4	13.5	0.26
5	15.2	0.33

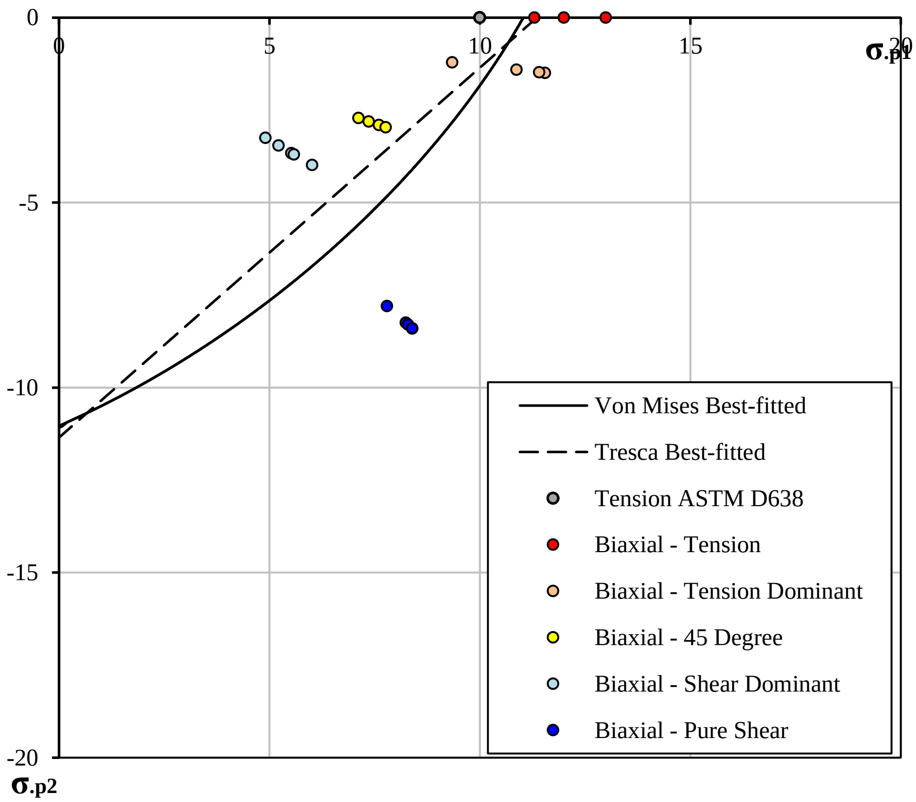

Figure 37. Biaxial tests: yield stress measurement.

5.3 Discussion: Biaxial Testing

5.3.1 Elastic shear modulus and validation of the shear properties

In order to verify the consistency between the tensile tests and the pure shear tests, the measured properties from both tests are analyzed. For an isotropic material, the two moduli and Poisson's ratio are related by Eq (32).

$$G = \frac{E}{2(1+v)} \tag{32}$$

The calculated shear modulus, using the E and υ measured from tensile test from Section 4.2, is shown below by Eq (33).

$$G = \frac{E}{2(1+v)} = \frac{514\ MPa}{2(1+0.44)} = 178\ MPa. \tag{33}$$

The calculated shear modulus, 178 MPa, closely matches the directly measured shear modulus from the biaxial test, 174 MPa. The difference of only 2.3% verifies that the pure shear tests are validly designed.

5.3.2 Plastic shear stress/strain relation and directionality of plasticity

The tensile modulus after yielding is 28 MPa, and the shear modulus after yielding is 25 MPa. Eq (32) is no longer applicable for the moduli found in the plastic region, indicating that the material is no longer isotropic. After yielding, the material becomes less stiff along the previous loading direction. Such anisotropy due to plastic deformation has to be understood for the hybrid joint design with flexible epoxy adhesives. For hybrid joints, certain loads are carried by adhesive, and the remaining loads are taken by the bolts. As mentioned in the literature review, Kelly [16] found that the design is improved when the bolts take higher load, and that this could be achieved by using a flexible adhesive. Given that the joint is always loaded in the same direction, permanent deformation of adhesive can help improve the bolt load transfer as it causes the adhesive to be even more flexible in the loading direction. The examples of the aircraft parts that are load in a single direction are the aircraft fuselage or helicopter blades. The joints in these parts are always in tension. If loading on the joint involves multiple directionalities, multidirectional plasticity presents additional complexity to the design problem.

5.3.3 Poisson's effects on yield stress measurement, and caution for joint design

Unfortunately, the loading orientations containing tensile components of stress in the adhesive are highly affected by the Poisson's effect as previously predicted in Section 4.3.2. These orientations include pure tension, tension-dominant, tension-shear and shear-dominant. The Poisson's effect causes stress concentration, therefore inaccuracy in the yield stress measurement. It is once more emphasized that such stress concentration needs to be properly considered in the joint design.

In order to quantify the severity of the stress concentration, an FE modeling of the biaxial tests is performed. Linear elastic analysis is used for simplicity to look only at the initial stress concentration at small strain. Figure 38 shows the mesh of the FE model. The V-notched specimen is loaded once by shear load and another time by tensile loading. The magnitude of each load is such that the applied tensile and shear loads produce average stress values of unity in the adhesive. Figure 39 shows the stress results of the FE analysis.

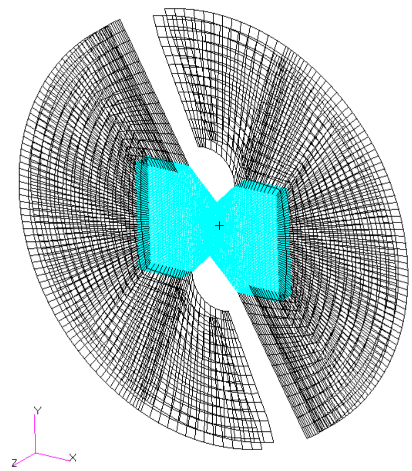

Figure 38. Mesh generated for FE analysis of the biaxial tests.

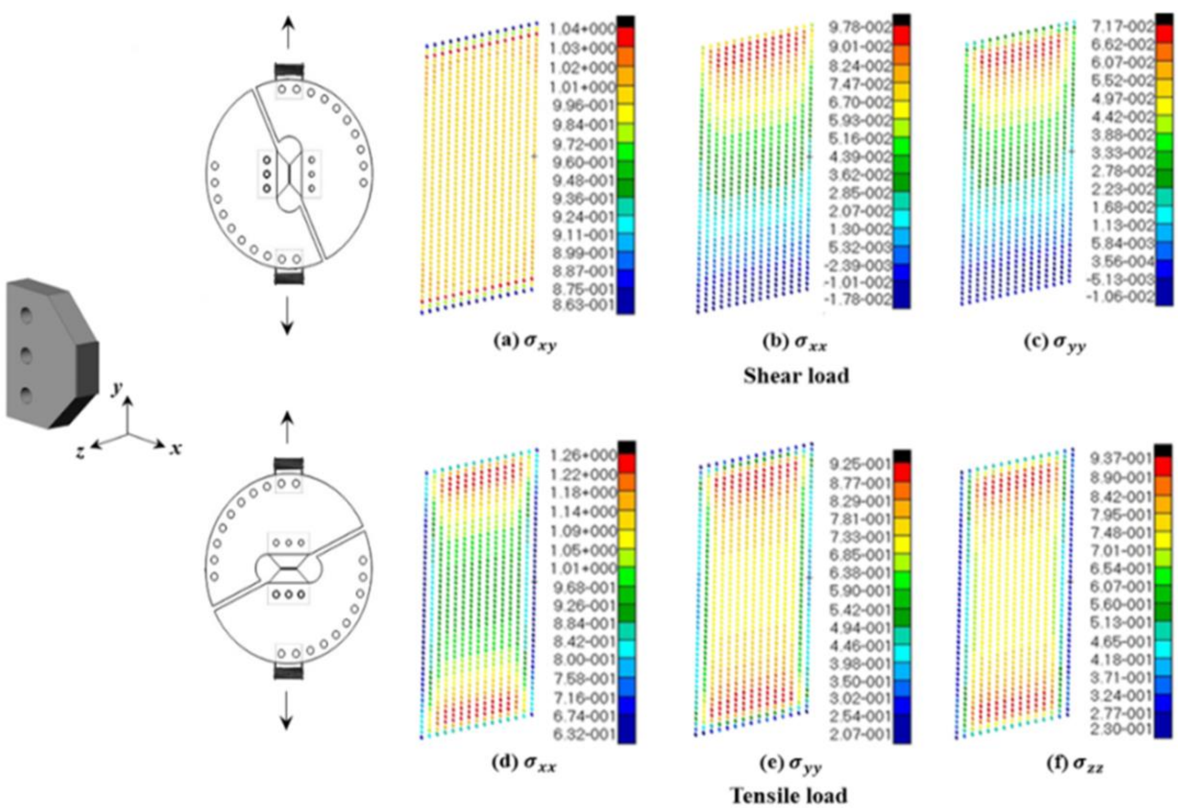

Figure 39. FE modelling stress results. (a-c) shear load case (b-d) tensile load case

For the shear case presented by Figure 39 (a-c), throughout the overlap, uniform shear stress whose values are nearly unity are found, except for the overlap ends. The overlap ends have lower stress value. This is due to the presence of the free surfaces, and theoretically there has to be a zero stress on these free surfaces. As shear deformation involves no volume change, there is no Poisson's effect. Therefore, the axial stresses in x and y direction are negligible: they have values that are two order magnitudes lower than the shear stress. The uniformity of the shear stress is achieved due to the flexibility of the adhesive. Therefore, the validity of the shear test is once again verified by FE modeling in addition to the modulus calculation from Section 5.3.1.

For the tensile case presented by Figure 39 (d-f), the three axial stresses are presented: σ_{xx}, σ_{yy} and σ_{zz}. Though the average tensile stress is close to unity, the peak stress of σ_{xx} reaches 1.26, which is 26% higher than the average value. At the same location of the stress peak for σ_{yy} and σ_{zz} reach 0.93 and 0.94, respectively. The three components of axial stresses at this critical location, $\begin{bmatrix}\sigma_{xx} = 1.26\\ \sigma_{yy} = 0.93\\ \sigma_{zz} = 0.94\end{bmatrix}$, are severely concentrated compared to the desired stress state of $\begin{bmatrix}\sigma_{xx} = 1.0\\ \sigma_{yy} = 0.0\\ \sigma_{zz} = 0.0\end{bmatrix}$. The stress concentration acts almost as if it is an inverse hydrostatic stress that outwardly tears the material. From the FE stress analysis of the V-notched specimen under tension, it is quantitatively shown that high Poisson's ratio results in undesired stress states, therefore inaccuracy in yield stress approximation.

5.3.4 Evaluation of the ARD strain measurement method

This study presents and validates the ARD method to measure strain in a thin adhesive bondline. Even if the bond is very thin, if the displacement of the adherends is properly measured, the strain in the adhesive can be accurately approximated from the relative displacement of the adherends. DIC can accurately measure adherends displacement as small as one tenth of a pixel size. For a smaller thickness than that of the current study, such as film adhesives, significant zooming is possible through proper lens selection and the use of an extension tube. If there is undesired aberration caused by extensive zooming, it can be corrected through image processing techniques presented by Yoneyama *et al*. [45]

6. Adhesive Hysteresis Testing

EA9361, the representative material for flexible adhesives, exhibits distinct yielding. After yielding, permanent deformation remains. The presence of permanent deformation indicates that the adhesive's properties change once the adhesive in a joint yields. In order to study the evolution of material properties, bulk specimens of EA9361 are tested under cyclic loading. Whether or not hysteresis convergence is attained in EA9361 is to be determined. Also the behaviour of the sample before and after hysteresis are to be compared.

6.1 Methodology

6.1.1 Sample preparation

The same type of sample as in the tensile testing, based on ASTM D638, is used for the hysteresis tests. The manufacturing procedure of this type of sample has been outlined in in Section 4.1.1. Four samples that are tested achieve their thickness controlled to be within $3.30 \pm 0.03\ \mathrm{mm}$, and the cross section area controlled to be within $41.3 \pm 0.6\ \mathrm{mm}^2$ in the gage section.

6.1.2 Experimental procedure

The Insight 5kN MTS measures the force and the PointGrey Flea 5MP camera simultaneously captures the images, similar to the previous tensile testing described in Section 4.1.2. This set-up is illustrated by Figure 20 in Section 4.1.2.

Head Speed

The slower the head speed of the MTS machine, the closer is the test to quasi-static. But testing with slower speed also requires longer time to test. In order to help determine an appropriate test speed for the hysteresis test, EA9361 is preliminarily tested at different head speeds. The specimens are tested in tension in the range of head speeds from 0.1 mm/min to 10 mm/min. The recommended speed from ASTM D638 is 5 mm/min. The head is displaced up to 1 millimeter, within which the sample stays un-yielded based on the results from the tensile tests. No DIC is performed, and the results of this sensitivity test are expressed with force and cross-head displacement measurements.

Figure 40 displays the results of the sensitivity test with force/displacement curves. As expected from the viscous nature of EA9361, the faster the head rate, the stiffer the material response. It has to be noted that the value of the stiffness should not be considered to be a material property, because the measured displacement is for the whole system, rather than for just the specimen. Figure 41 plots the values of the stiffness from each of the testing rates, from which the linearly relation is observed between stiffness and logarithmic head speed.

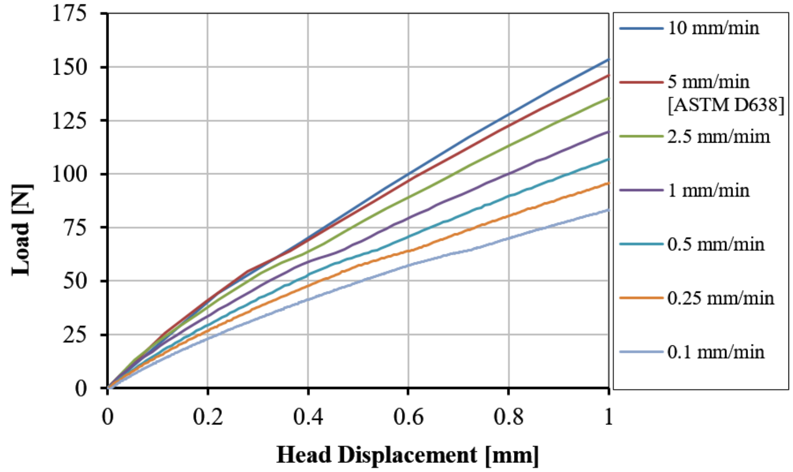

Figure 40. Force vs displacement of EA9361 under various head speeds.

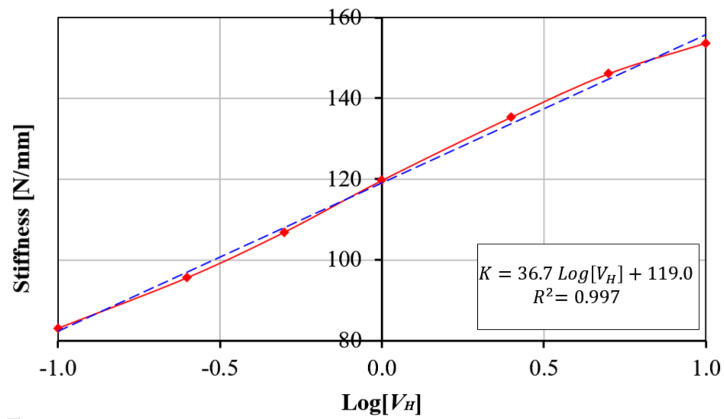

Figure 41. Head speed vs stiffness of EA9361

Even at 0.1 mm/min, 50 times slower than the recommended speed, the material property does not reach quasi-static. Though viscosity exists at all levels of speed and quasi-static loading is impractical, it is still recommended to use a slower speed to reduce the effects of viscosity. The head speed is selected to be at 1 mm/min. Further reduction would result in overly long time to perform the tests.

Sampling Rate

For the MTS, the sampling rate is set at 1 Hz as in the tensile testing. But, the sampling rate of the image capturing is reduced by five times to 0.2 Hz from 1 Hz. The sampling rate with respect to strain rate is in fact reduced by half, considering that the head speed is also reduced by 2.5 times from 2.5 mm/min to 1 mm/min. Hysteresis testing is to be performed until the convergence of material properties is observed. Thus, in order to avoid excessive amount of space usage due to the large size of the image files, the sampling rate of the camera has to be set slower.

Loading Part I: Cyclic Loading

The cyclic loading is applied such that the upper limit is defined by displacement, and the lower limit is defined by force. The upper displacement limit is selected to be 26 mm. This value corresponds to 25% true strain. It is half of the ultimate failure strain, based on the force/displacement and stress/strain relations from the tensile test shown by Figure 21 and Figure 22. The lower force limit is set at 10 N. EA9361 is very viscous and the head speed is indeed faster than the rate of the specimen’s shrinkage according to the preliminary testing during the unloading. Therefore, in order to avoid compressive stress in the specimen, the lower limit is set as a force slightly higher than zero force. This way, the nature of the cyclic loading stays in the tension-tension regime. Without such force boundary condition, not only compressive stress could develop, but the sample could easily buckle due to its small thickness relative to its length. Figure 42 graphically shows the cyclic loading to be applied to the specimens. The total number of the cycles is unlimited, and the machine is manually turned off when convergence is observed.

Loading Part II: Static Loading

Once the convergence is detected from the cyclic loading, the specimen is left to shrink until it becomes stress-free. Then the specimen is loaded again until failure at the same head speed as in the cyclic part, that is 1 mm/min.

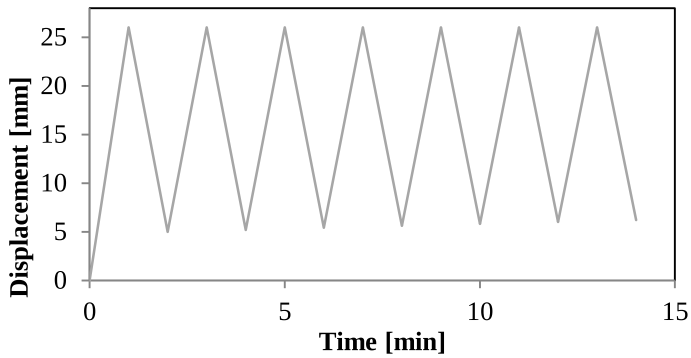

Figure 42. Schematic of cyclic loading for EA9361 hysteresis tests.

6.2 Results

The response from EA9361 under cyclic load converges. Therefore, the material is reloaded till failure, and the stress/strain results of the tests are shown in Figure 43. The cyclically loaded parts are drawn with solid lines; the statically loaded parts after the convergence are drawn with dashed lines. The hysteresis loops are found to be approximately between true strain value of 0.22 and 0.27. After the convergence of the loop, when the specimens are left to shrink, they contracted to a true strain value of around 0.12. Figure 44 compares the specimen before and after the hysteresis. On the left of the figure are the undeformed specimens. On the right of the figure shows the left most specimen elongated after a cyclic load and the rest of the specimen undeformed. When the specimens are statically re-loaded till failure, they failed by net-section failure. The strain values at full shrinkage and the failure strain values are summarized by Table 8.

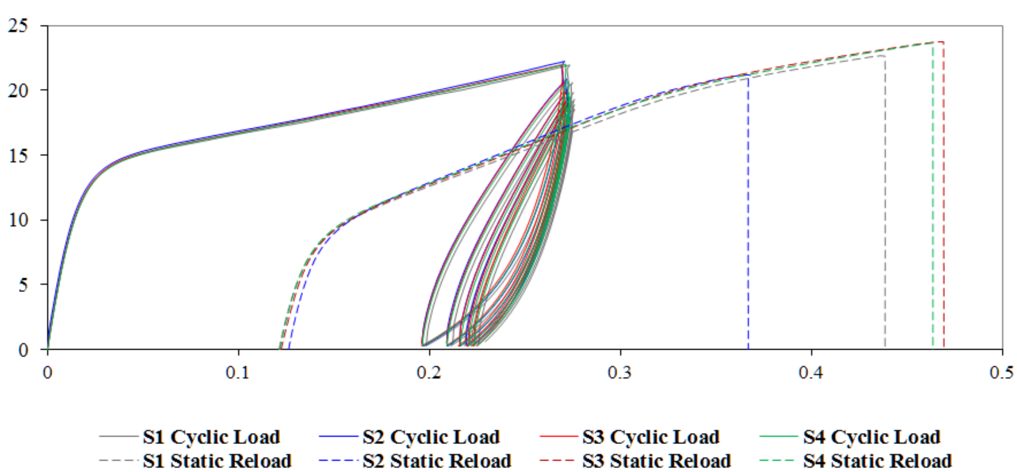

Figure 43. EA9361 hysteresis tests: stress vs strain

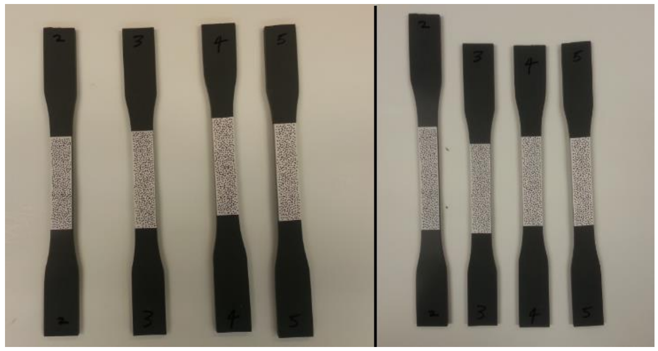

Figure 44. EA9361 hysteresis tests: undeformed vs deformed specimen

Table 8. EA9361 hysteresis tests: permanent strain and failure strain.

Specimen	Permanent Strain (after full shrinkage)	Failure Strain
1	0.13	0.37
2	0.12	0.44
3	0.12	0.46
4	0.12	0.47

6.3 Discussion: Bulk Specimen Hysteresis Testing

6.3.1 The effects of the adhesive's viscosity

Although the permanents strain after the convergence is 0.12 as seen in Table 8, the value of the strain at the near-zero force in the converged loop is 0.22. The material shrinks from a strain of 0.22 to 0.12, indicating the presence of significant viscous effects. The more flexible the adhesive, the more viscous manner in which it behaves. Inside the loop, the stress/strain in the loading phase is closer to a straight line rather than a bilinear curve. This is because of the dynamic load due to the adhesive's viscosity: while the material wants to shrink, the MTS machine stretches the adhesive. Bilinear response is observed again when the fully shrunk specimens are statically re-loaded. Considering the frequency of the repeated loading found in industrial applications, it is unlikely that EA9361 would fully shrink between cycles. For flexible epoxy adhesives, the presence of dynamic loads in the adhesive is unavoidable in practice.

6.3.2 Post-hysteresis yield stress/strain

The same specimen behaves differently between when initially loaded and when loaded after the hysteresis cycles. As shown in Figure 43, the yield stress decreases from about 13 MPa to 10 MPa. Also the yield strain of the specimen dramatically increases, due to permanent deformation, with respect to the undeformed configuration. This change in the properties certainly affects the joint performance. For example, Bodjona's [46] sensitivity test for hybrid joints found out that the yield stress is the most significant variable for bolt load sharing in a hybrid joint.

6.3.3 Application to hybrid joints

Section 5.3.2 discusses that the presence of adhesive yielding could be beneficial for bolt load transfer of a hybrid joint; it predicts that the adhesive will exhibit a less stiff response after yielding and consequently the bolt carries more load. Figure 43 shows that the stress/strain curve of the static reload starts from permanent strain value of 0.12. Consequently, for a particular value of strain, the corresponding stress from the static reload is significantly lower than the stress from the initial cycle of the hysteresis test. Therefore, it is verified by the hysteresis tests that permanent deformation causes a less stiff response from the adhesive. Yielding further softens flexible adhesive, and bolt load transfer in hybrid joint is improved.

In addition to permanent deformation, the hysteresis test also identifies viscosity as a source of improvement for the bolt load transfer. Assume that a hybrid joint is loaded and is stretched by displacement, *d*. And the adhesive is also deformed by certain value of strain as a result of the joint displacement. Then as the load is removed, the adhesive would tend to shrink towards the value of the permanent strain that is found at fully shrunk state. This would occur over a long period of time. While the adhesive shrinks, it is as if the adhesive deformation exists without the adhesive taking any load. Viscosity allows the adhesive deformation without load being concurrently applied. If a joint with the adhesive in such state is loaded, more load would transfer through the bolts.

7. Hybrid Bonded/Bolted Joint Hysteresis Testing

Repeated loadings and repeated applications are inevitable for joint structures in actual use. Chapter 6 discusses the bulk adhesive's response under cyclic loading. Observations of the bulk adhesive leads to prediction of behavior of hybrid joints with flexible epoxy adhesives. In this section, hybrid joints are tested under cyclical loading to generate a better *in-situ* understanding. Any observation from the joint tests that relates to previous findings from the material characterization of EA9361 is to be discussed.

7.1 Methodology

7.1.1 Sample preparation

Plate Manufacturing

In order to produce the substrates for the hybrid joints, a composite plate is manufactured first. Cycom 5320 CFRP prepreg tape is used. The ply sequence of the laminate is $[45/0/-45/90]_{4S}$. Plies are laid up on an aluminum flat tool plate. During the lay-up, a debulk is performed at every four plies. Once all plies are stacked, the laminate is subjected to a debulk for 12 hours or more. Afterwards, the vacuum-bagged laminates are cured in an oven using the manufacturer's recommended cure cycle.

Hybrid Joint Manufacturing

The cured plate is cut into the width of the joint, using a saw with a diamond tip. The thickness of the adhesive is targeted at 0.5 mm. This thickness is recommended by the industrial sponsors of this project. A thickness of 0.5 mm is the maximum thickness used in aerospace applications. Maximum thickness is preferred over smaller thickness because of the manufacturing challenges. The appearance and the dimensions of the hybrid joint are illustrated in Figure 45.

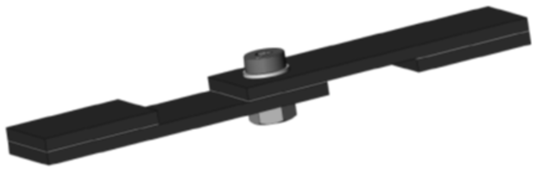

(a) CAD model of the hybrid joint

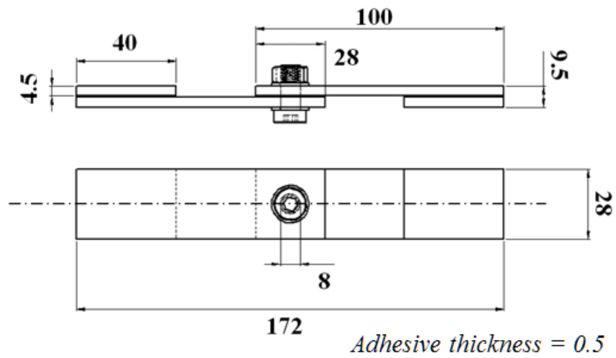

(b) Dimensions of the hybrid joint

Figure 45. CAD model of the hybrid joint and its dimensions in millimetres.

Before the hybrid joint, the bonded joint to be drilled is first made. The bonded joint manufacturing is performed using a custom-designed mold, designed by Bodjona. [18] The mold produces two joints at a time. The bonding procedures take the following steps, which are also summarized in Figure 46.

The precisely machined mold and its shim enables the control of the adherends alignment, overlap length and the adhesive thickness of 0.5 mm. The process is initiated by sand-blasting the bonding surfaces of the CFRP adherends. The bottom adherends, shims and doublers are placed on the mold, as shown by Figure 46 (a). The top shims are placed on the adherend, and solder wires of 0.508 mm (equivalently 0.02″) in diameter are placed on the bottom doublers. (Figure 46 (b)) The shim’s thickness and the diameter of the wire serve to control the adhesive thickness in the overlap and in the doubler respectively. EA9361 is applied at the locations of the overlap and the doublers. Then, the top doublers and adherends are placed. (Figure 46 (c)) The clamping blocks fix the hybrid joint assembly, and the lid is closed. (Figure 46 (d)) The mold is cured in an oven. The two-dwell cure cycle previously presented in Section 5.1.1 by Figure 31 is used. Once the joints are cured, the excess adhesive is removed and the remaining rough surface is polished.

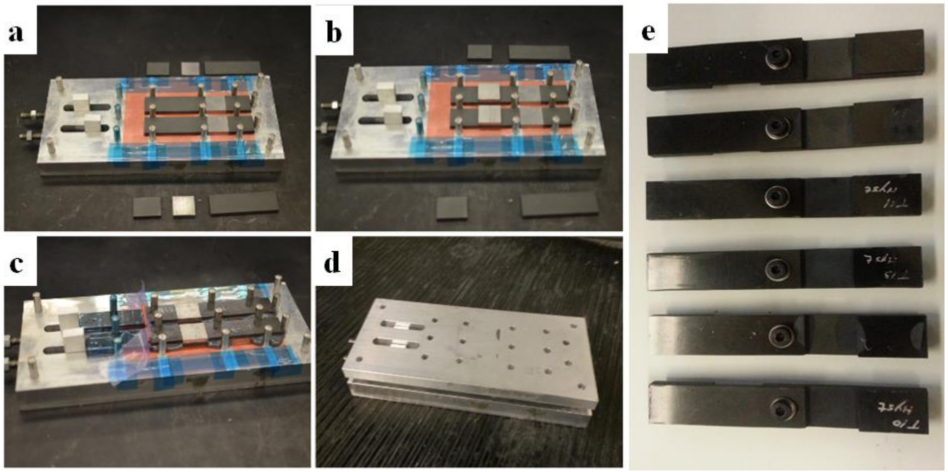

Figure 46. Hybrid joint manufacturing procedure.

Once the bonded joints are ready, holes are drilled for the bolts to be installed. CNC drilling is performed using the drill bit, Sandvik-Coromant Corodrill 854, whose application is specific to composite materials. This drill bit is capable of machining the hole as precisely as ± 0.025 mm in diameter. Finally, shoulder-bolts made of 4137 alloy steel are installed to complete the hybrid joints.

7.1.2 Experimental procedure

Cyclic Loading

Preliminary tests are performed to tune the experiments. In the tuning experiments, the joint is statically loaded and value of the displacement at half the failure load is recorded. This value is found to be approximately 0.6 mm, and is used as the maximum displacement of the cyclic load. Then the minimum displacement is set to be 25% of the maximum, which is 0.15 mm. As the tuning sample is cyclically loaded, the joints achieves convergence within 15 cycles. It is observed that the force response always stays in tension throughout the testing.

After the tuning, the final loading cycle is defined. The oscillatory displacement is to be applied between d = 0.15 and 0.6 for 15 cycles. After the 15 cycles, the head returns to zero displacement. The head speed is set at 0.006 mm/min similar to Bodjona's static tests which employ the identical hybrid joint specimen [18]. Figure 47 is the visualization of the loading in displacement vs time.

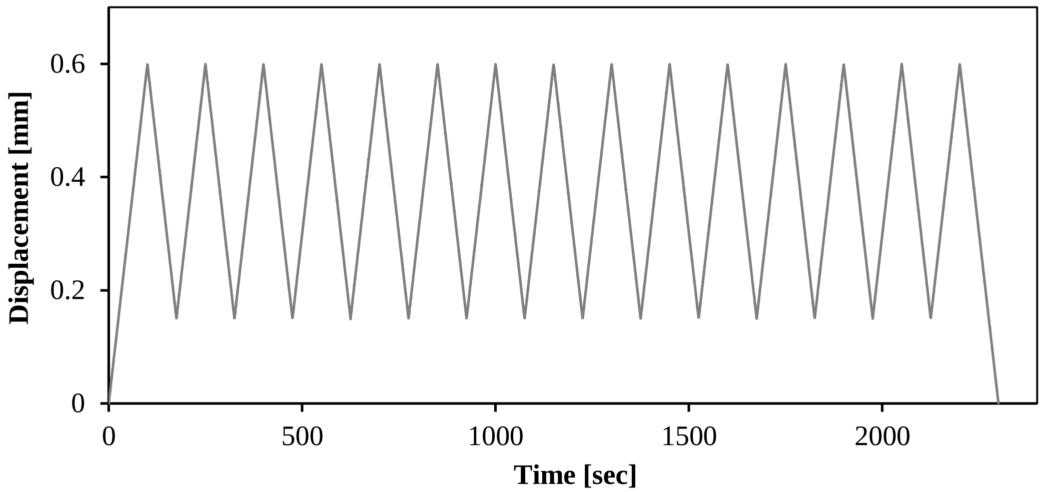

Figure 47. Joint hysteresis tests: cyclic loads.

Test Set-up

A 100 kN MTS machine is used to load the hybrid joints. The MTS records the force at 1 Hz. The testing is performed at room temperature. Figure 48 depicts the joint being tested.

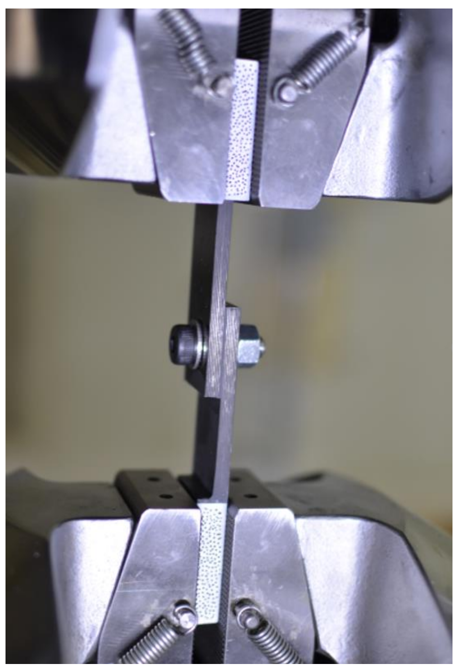

Figure 48. Hybrid joint hysteresis tests.

7.2 Results

The force/displacement results and the force/time results are shown by Figure 49 and Figure 50 respectively. It is observed in the force/displacement results that convergence is achieved. The converged loops are seen in Figure 49. Also observed in the force/displacement results is the drop in the load at maximum displacement. One could also notice that the peak load asymptotes toward the converged value in Figure 50.

For the initial cycle, the stiffness drops at around $d = 0.17$, but the change occurs gradually. The second and the subsequent cycles exerts significantly lower force response than the initial cycle, similar to the responses of the bulk adhesive specimens under cyclic loads presented by Figure 43 in Section 6.2. When the head is returned to zero after the cycles, compressive load is detected, indicating presence of the permanent deformation.

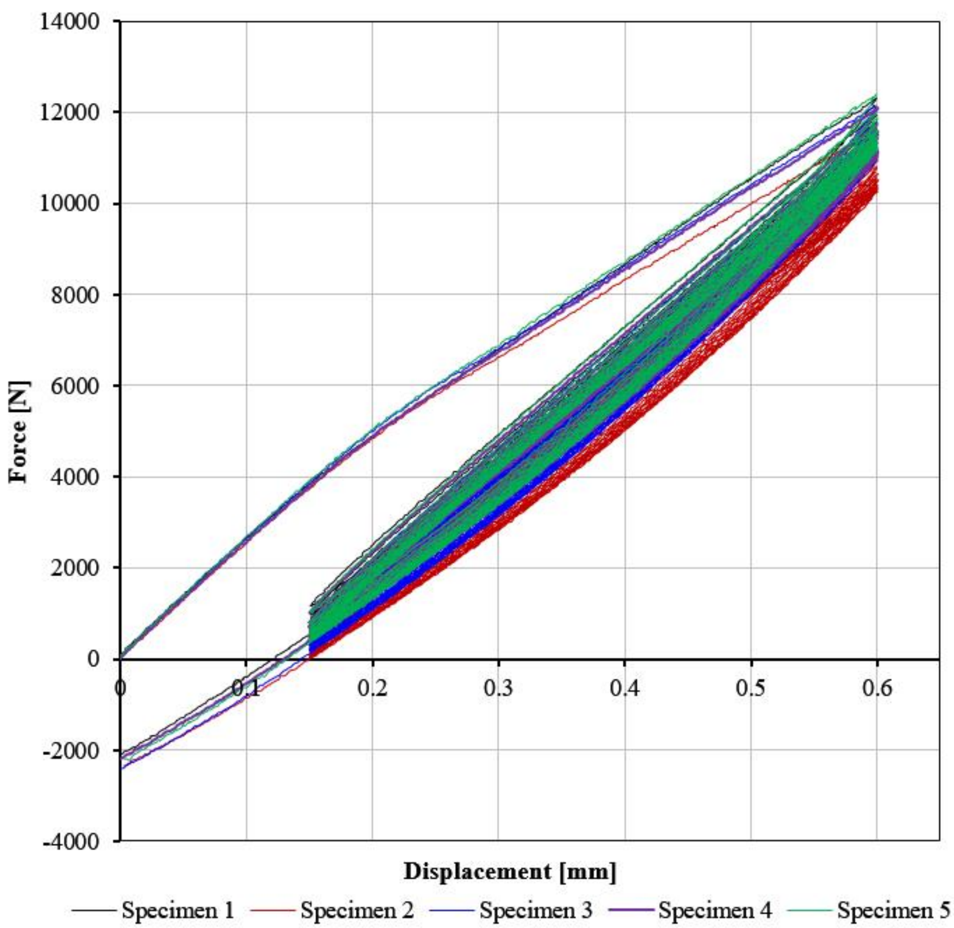

Figure 49. Hybrid joint hysteresis tests: force vs displacement.

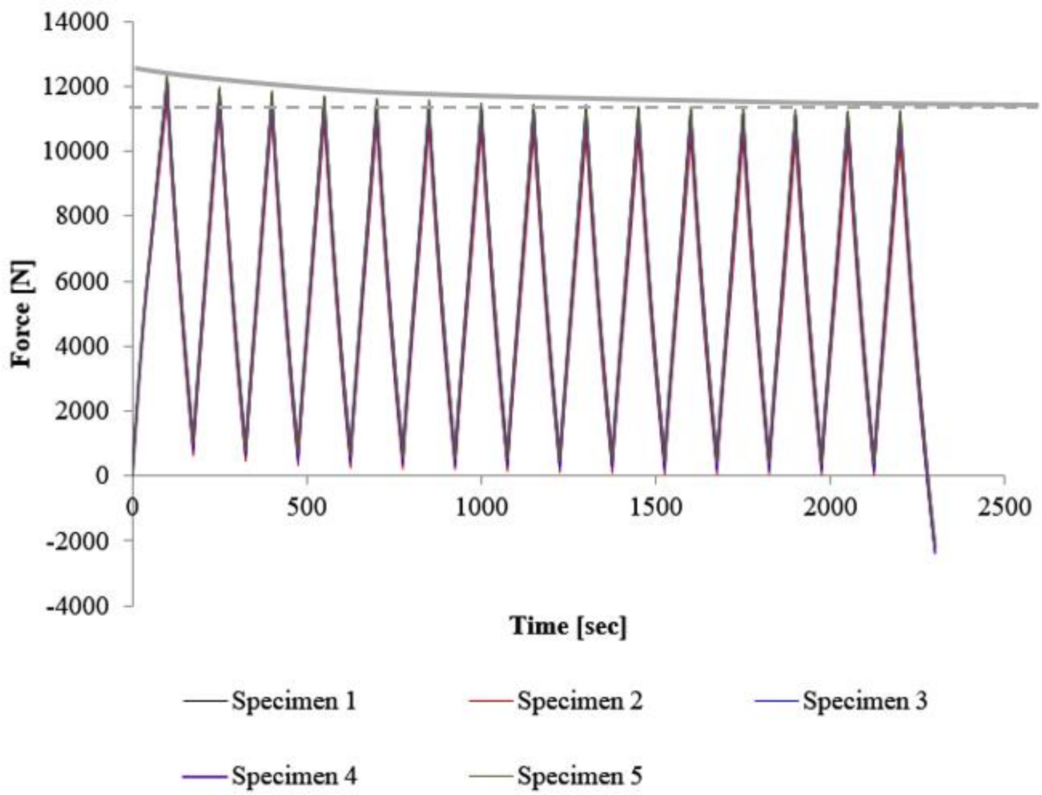

Figure 50. Hybrid joint hysteresis tests: force vs time.

7.3 Discussion

It was pointed out from the literature review that the performance of the conventional hybrid joint is highly inefficient due to the fact that the adhesive that is too stiff; the adhesive carries most of the load and the bolt is barely carrying any load, but simply adds weight. In addition, unless the bolt has a perfect fit, which is rarely achieved in practice, only the adhesive carries the load until the bolts comes in contact with the hole surface. Therefore, a flexible adhesive is desired for improving the efficiency.

At about a displacement of 0.17 mm in Figure 49, one can notice the change in slope that indicates the yielding of the adhesive. The change in slope is not as abrupt as in the tensile test, because the adhesive yields gradually. The adhesive in a single lap joint has a peak stress at the overlap's end. Therefore, the yielding initiates at the overlap ends. Then, the region of plastic deformation propagates towards the center of the overlap. For this region, the drop in stiffness occurs gradually.

From the second and subsequent loadings, the force/displacement curves exhibit significantly lower force response than the curve from the initial loading. This is due to the combined effects from yielding and viscosity that have been previously discussed in Section 6.3.3. Despite the complicated response of EA9361, its application in hybrid joint is promising. According to Figure 49, when equal force is applied to specimens, the later cycles reach higher displacements than the earlier cycles. The shear load through the bolt is relevant to the total head displacement and irrelevant to the adhesive deformation. Based on this principle, one knows that in the later cycles, the bolt is carrying more load than in the earlier cycles, for a given applied load. Conclusively, the hybrid joint hysteresis testing found that, in the presence of yielding and viscous effects of the EA9361, the bolt load transfer is improved, which could lead to higher joint strength and fatigue resistance. [10]

8. Conclusion

As the usefulness of the flexible epoxy adhesives on the design of hybrid joints is certain, the present study has analyzed EA9361, as a representative material for flexible epoxy adhesives. Three sets of experiments are performed to characterize EA9361: the tensile tests, biaxial tests and the hysteresis tests. Each experiment has contributed to further understanding of flexible epoxy adhesive and its applicability to joint design.

The tensile stress/strain relation and the Poisson's ratio are generated by the tensile tests. The pure shear case of the biaxial tests also generates stress/strain in shear. The two tests also quantify modulus, yield stress and failure strength of EA9361 in tension and shear. These mechanical properties of EA9361 are summarized by Table 9.

Table 9. EA9361 measured properties.

E_{el} [MPa]	E_{pl} [MPa]	G_{el} [MPa]	G_{pl} [MPa]	ν	σ_{xx}^{yield} [MPa]	σ_{xx}^{f} [MPa]	ε_{xx}^{f}	σ_{xy}^{yield} [MPa]	σ_{xy}^{f} [MPa]	ε_{xy}^{f}
514	28	174	25	0.38-0.47	10	27.5	0.53	8.3	13.76	0.29

A meaningful observation from the stress/strain curves from the tensile tests and the pure shear test is the distinct yielding of the adhesive, after which the modulus sharply drops. This observation leads to simplifying the stress/strain relation to be bilinear. This studies verifies that the elastic/plastic bilinear material model is able to fit the experimental data more accurately than the commonly used hyperelastic model. Therefore, the present study presents a meaningful finding that the analysis and numerical simulation of flexible epoxy adhesive must be accompanied with elastic/plastic bilinear material model.

Another useful finding from the tensile tests is the varying value of Poisson's ratio. As the adhesives are constrained by the adherends, the stress in the adhesive is highly affected by Poisson's ratio. Therefore, this study advises that the varying value of Poisson's ratio be properly reflected when analyzing stress in the adhesive.

The biaxial tests, designed to measure yield stresses at different orientations of biaxial loads, have been unable to accurately measure the yield stresses. Nevertheless, a follow-up Finite

Element analysis detects the stress concentrations due to Poisson's effect. The Poisson's ratio of EA9361 is particularly high with an its initial value of 0.44 and its maximum value reaching 0.47. Therefore, this study brings up a valuable caution for severe stress concentrations caused by high value of the Poisson's ratio.

As the presence of yielding and permanent deformation indicates change in material properties, the hysteresis tests study the evolution of the material properties of EA9361 under cyclic loads. EA9361 exhibit weaker and weaker force response as the cycle continues, but the response eventually converges. The experimental results realize that the effects of the viscosity are substantial for the stress/strain response of EA9361 under cyclic loads. With the yielding and viscous effects together, it is significantly easier to deform the adhesive in the subsequent cycles compared to the initial cycle. This is a useful finding for the design of hybrid joints. As the adhesive requires less load to deform, it improves the bolt load transfer, which improves the joint's strength and fatigue resistance.

Finally, the hybrid joints are tested under cyclic loads and its applicability in the joint design is evaluated based on the findings from the previous characterization. From the force/displacement results of the first cycle, the drop in the joint's stiffness due to the adhesive yielding is observed. While the modulus drop is expected from the tensile tests, the yielding occurs gradually unlike the tensile tests. The yielding is progressive as it initiates locally and propagates along the adhesive bondline. In the subsequent cycles, the convergence in the response is reached. As the adhesive approaches convergence, the force response from the bond decreases due to the adhesive's plastic deformation and viscosity, indicating the higher bolt load transfer. Therefore, the *in-situ* improvement in bolt load transfer is verified at a joint level. It has to be noted that use of the yielding and viscous nature of the adhesive has to be limited to aircraft components that are always loaded in a single direction. The analysis of multi-directional yielding and dynamic loads is currently infeasible.

Although several aspects of flexible adhesives have been investigated in this study, one limitation is that they are studied only at room temperature. Structures operate at a wide range of temperatures. For example, currently commercial aircrafts operate at minimum temperature as low as -50°C. Potential future work is to examine the effects of temperature on the adhesive's properties.

Appendix

Appendix I. Manufacturer's Technical Data Sheet for EA9361

General Properties

	Part A	Part B	Mixed
Colors	White	Black	Grey
Viscosity (25°C) [Pa·s]	130	70	100
Brookfield, HBT	Spdl 5 @ 2.1 rad/sec	Spdl 5 @ 2.1 rad/sec	Spdl 5 @ 2.1 rad/sec
Density [g/ml]	1.33	1.26	1.28
Shelf life(25°C)	1 year	1 year	
Shelf life(32°C)	1 year	1 year	

Mixing Ratio (By weight): Part A to Part B = 1 : 1.4

Pot Life (450g mass): 120 minutes at 25°C

Application

- **Mixing:** Combine Part A and Part B in the correct ratio and mix thoroughly. THIS IS IMPORTANT! Heat buildup during or after mixing is normal. Do not mix quantities greater than 450 grams as dangerous heat buildup can occur causing uncontrolled decomposition of the mixed adhesive. TOXIC FUMES CAN OCCUR, RESULTING IN PERSONAL INJURY. Mixing smaller quantities will minimize the heat buildup.
- **Applying:** Bonding surfaces should be clean, dry and properly prepared. For optimum surface preparation consult the Hysol Surface Preparation Guide. The bonded parts should be held in contact until the adhesive is set. Handling strength for this adhesive will occur in 24 hours @ 77°F/25°C, after which the support tooling or pressure used during

cure may be removed. Since full bond strength has not yet been attained, load application should be small at this time.

- **Curing:** This adhesive may be cured for 5 to 7 days @ 77°F/25°C to achieve normal performance. Accelerated cures up to 200°F/93°C (for small masses only) may be used as an alternative. For example, 1 hour @ 180°F/82°C will give complete cure.

Bond Strength

- **Tensile Lap Shear Strength:** Tensile lap shear strength tested per ASTM D1002 after curing for 5 days @ 77°F/25°C. Adherends are 2024-T3 bare phosphoric acid anodized per ASTM D3933.

Test Temperature [°C]	Shear Strength [Mpa]
-196	27.6
-55	27.6
25	24.1
71	5.9

- **Peel Strength:** T-Peel strength tested per ASTM D1876 after curing for 5 days @ 77°F/25°C. Adherends are 2024-T3 bare phosphoric acid anodized per ASTM D3933.

Test Temperature [°C]	Peel Strength [N/25 mm]
-55	44
25	111

Service Temperature: Service temperature is defined as that temperature at which this adhesive still retains 1000 psi/6.9 MPa using test method ASTM D1002 and is approximately 140°F/60°C.

Bulk Resin Properties (Tensile Properties: - tested using 0.125 inch/3.18 mm castings per ASTM D638)

- **Elongation at Break (25°C):** 40%
- **Shore D Hardness (25°C):** 70
- **Tensile Modulus (25°C):** 723 MPa

Appendix II. Compression Mold Design

This section describes the custom design of the compression mold aimed to manufacturer an adhesive plate in order to produce a dogbone sample that meets the specification of the ASTM D638. In the drawings to be presented next, all dimensions are in inches unless otherwise specified.

Compression Mold Assembly

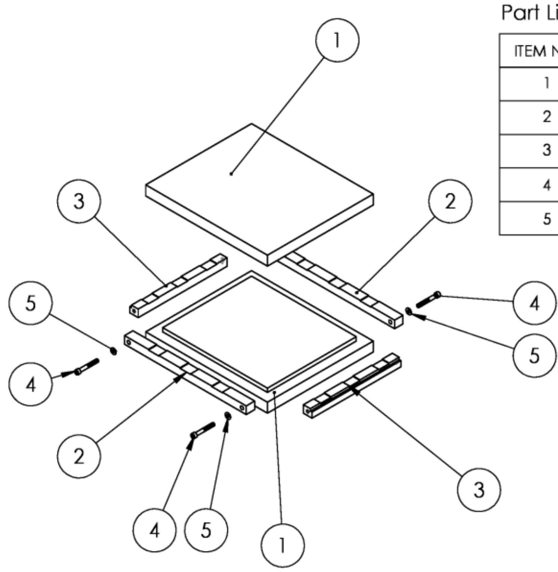

Part List

ITEM NO.	PART NUMBER	DESCRIPTION	QTY.
1	p01_BaseLid_Plate	Base & Lid Plate	2
2	p02_SideWall_A_	Longer Side Wall	2
3	p03_SideWall_B_	Shorter Side Wall	2
4	91251A448	Screw	4
5	91950A027	Washer	4

Material and Dimensions

Part	Material	Dimension
Base & Lid Plate	Al 6061-T651 Plate	12" X 10.5" X 1.5"
Longer Side Wall (A)	Al 6061 T-6511 Bar	1" X 1.25" X 11"
Shorter Side Wall (B)	Al 6061-T6511 Bar	1" X 1.25" X 10"

Note:

- In the part list, the parts number for the screws and washers correspond to part number found in McMaster-Carr. [47, 48]

Base and Lid Plate

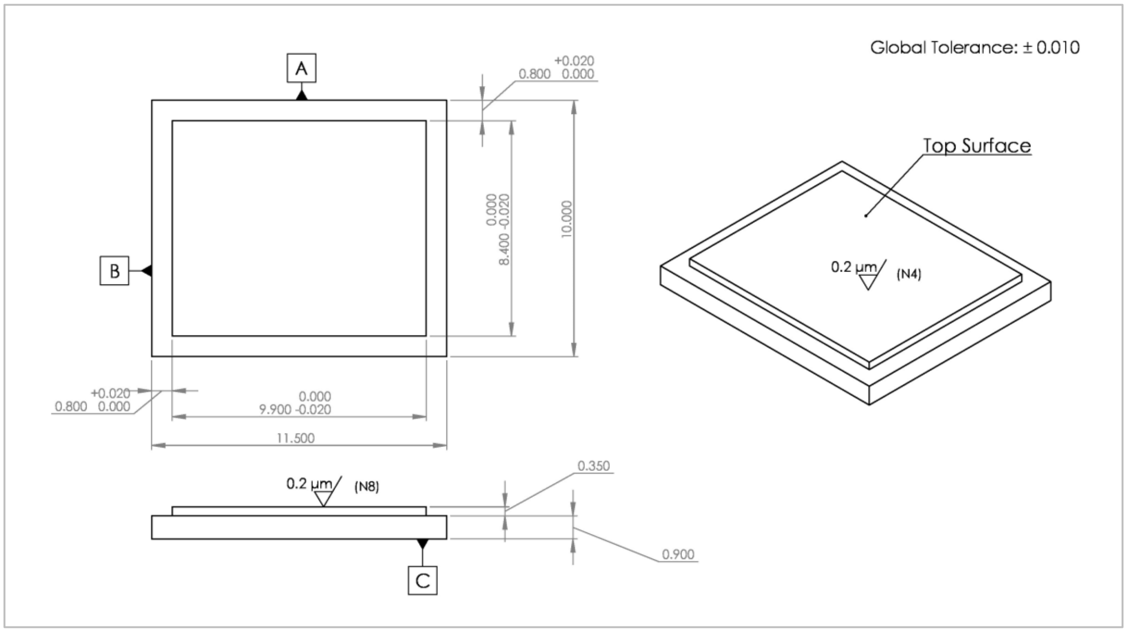

Note:

- The surface finish on the molding surface is in millimeters unlike all other dimensions that are in inches. The quality of this finish corresponds to a mirror finish.

SideWall A

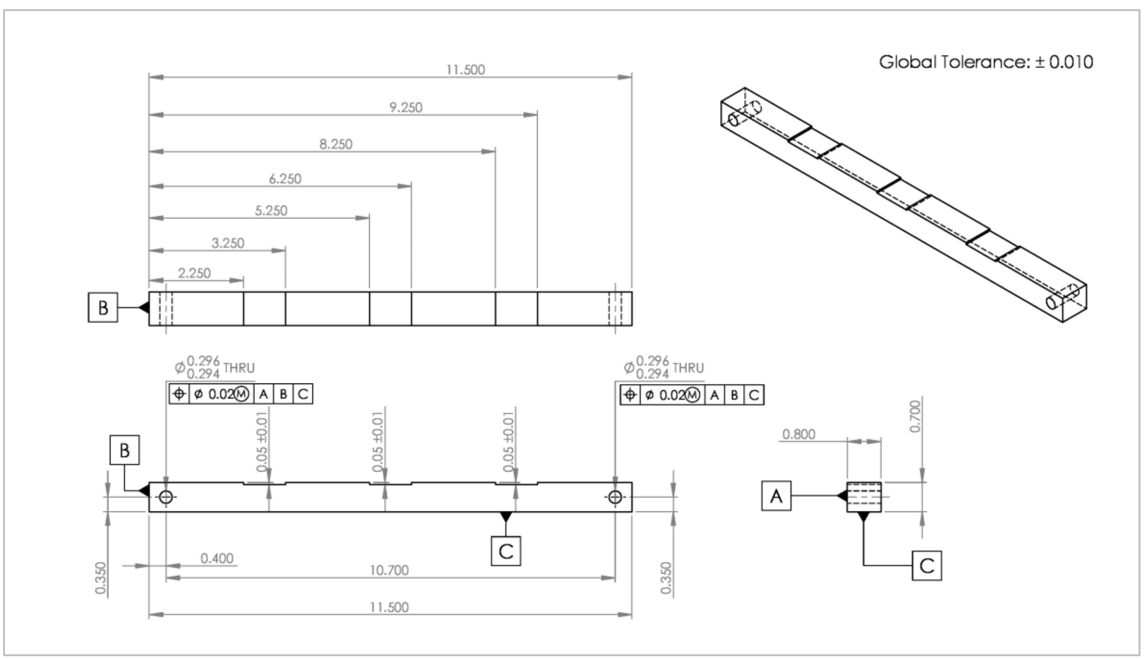

SideWall B

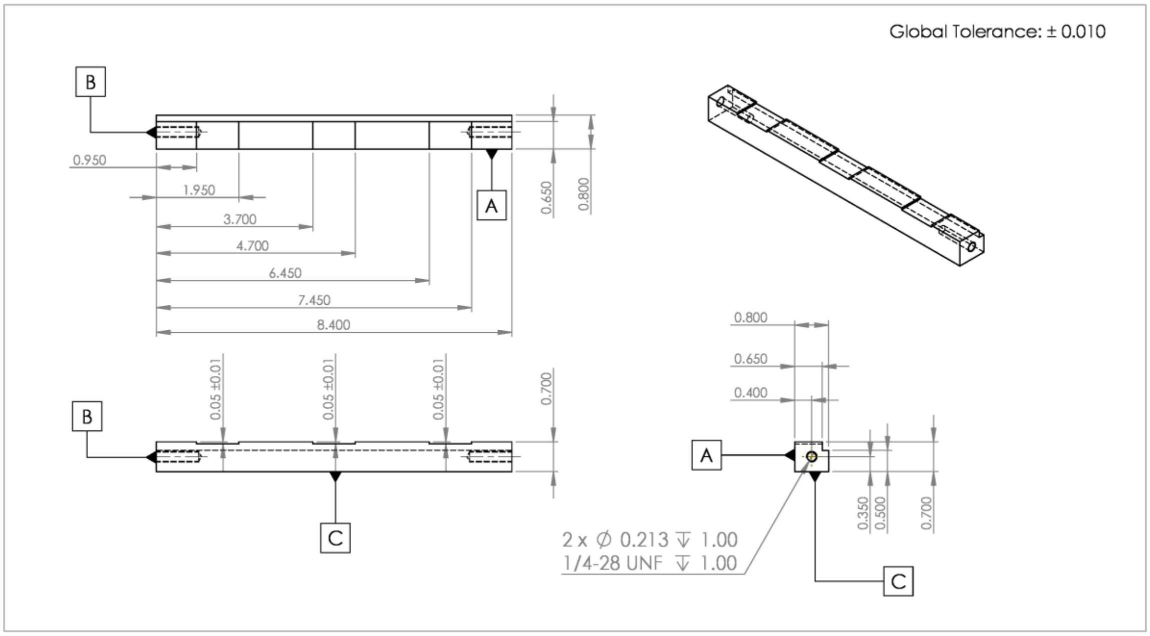

Global Tolerance: ± 0.010
B
A
C
0.950
1.950
3.700
4.700
6.450
7.450
8.400
0.650
0.800
0.05 ±0.01
0.700
0.400
0.350
0.500
2 x Ø 0.213 ↧ 1.00
1/4-28 UNF ↧ 1.00

Appendix III. V-Notched Specimen Design

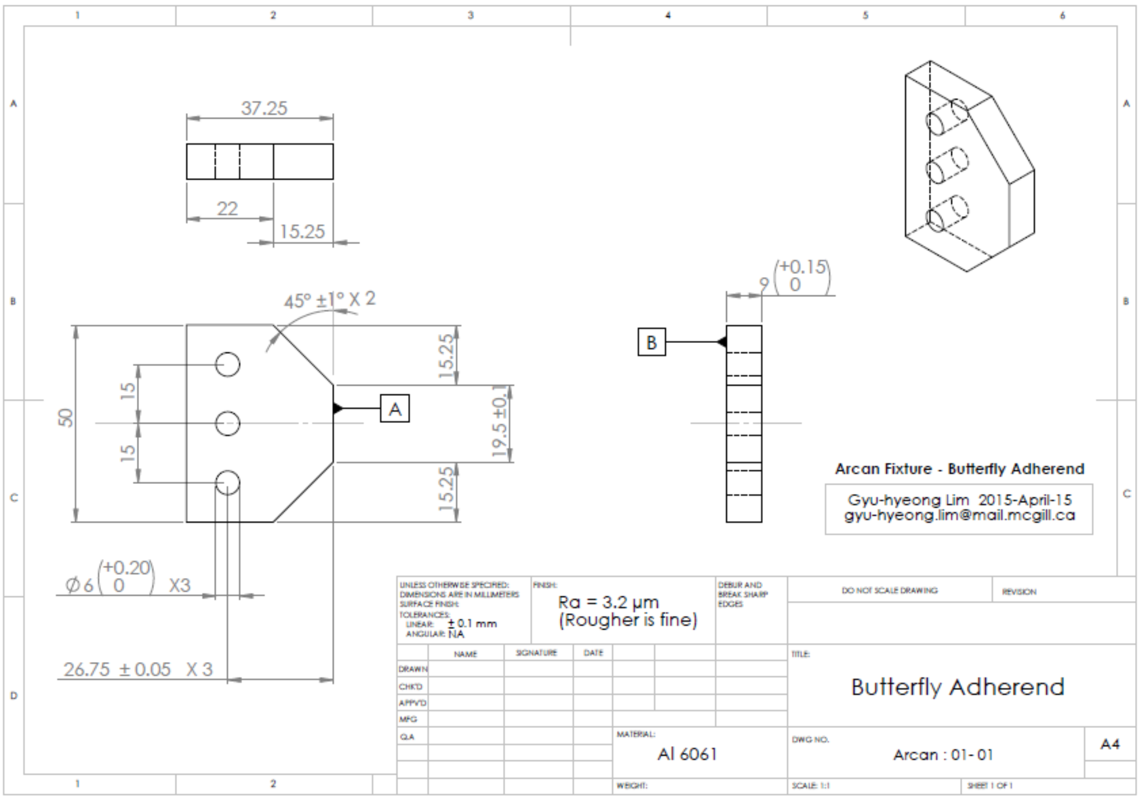

Appendix IV. Bonging Jig Design

Base Plate

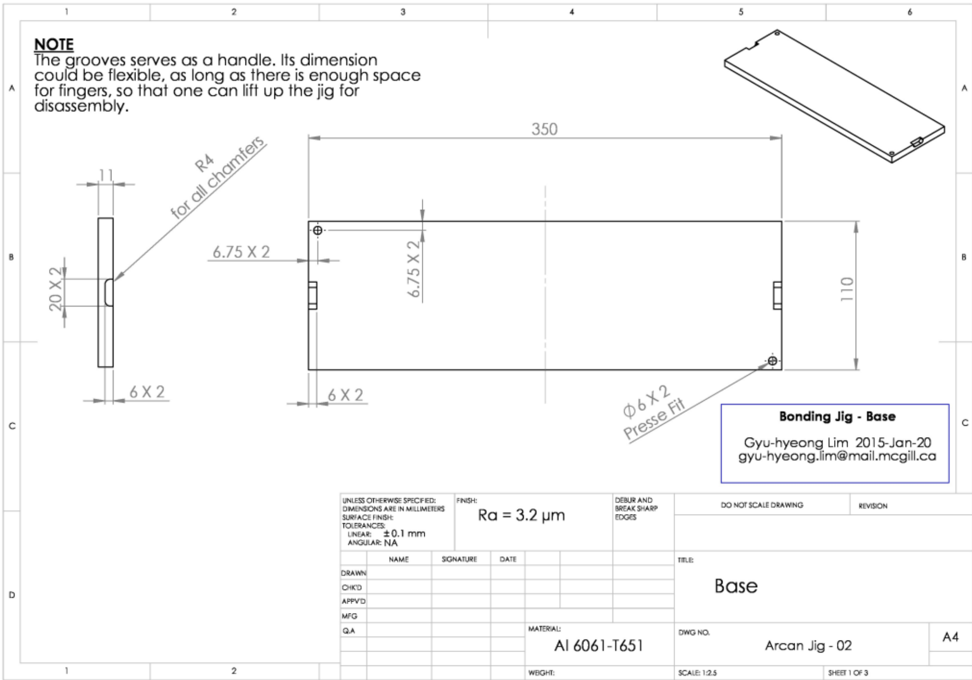

Lid

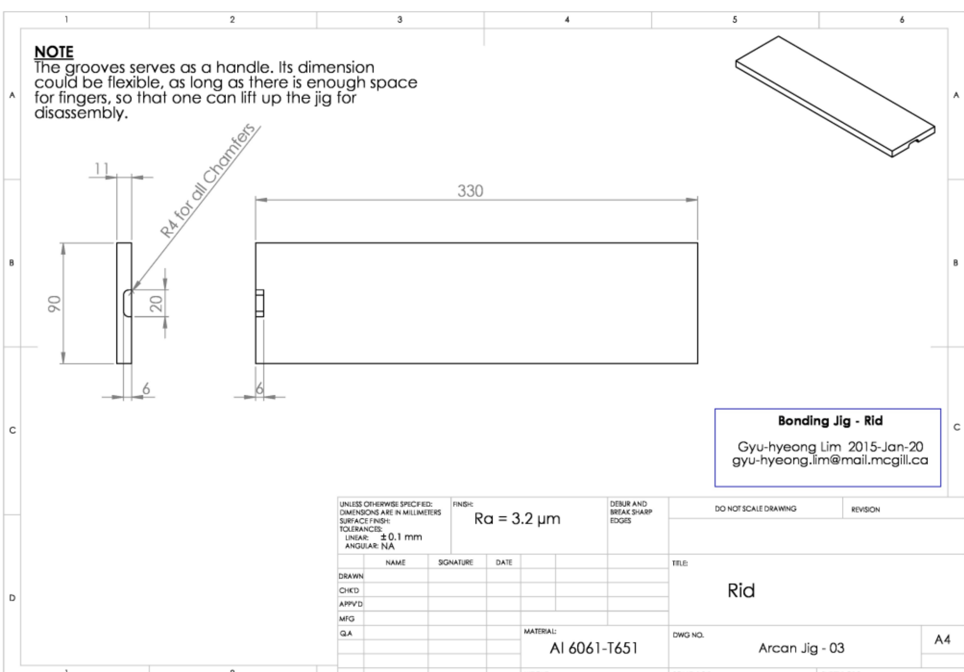

Jig

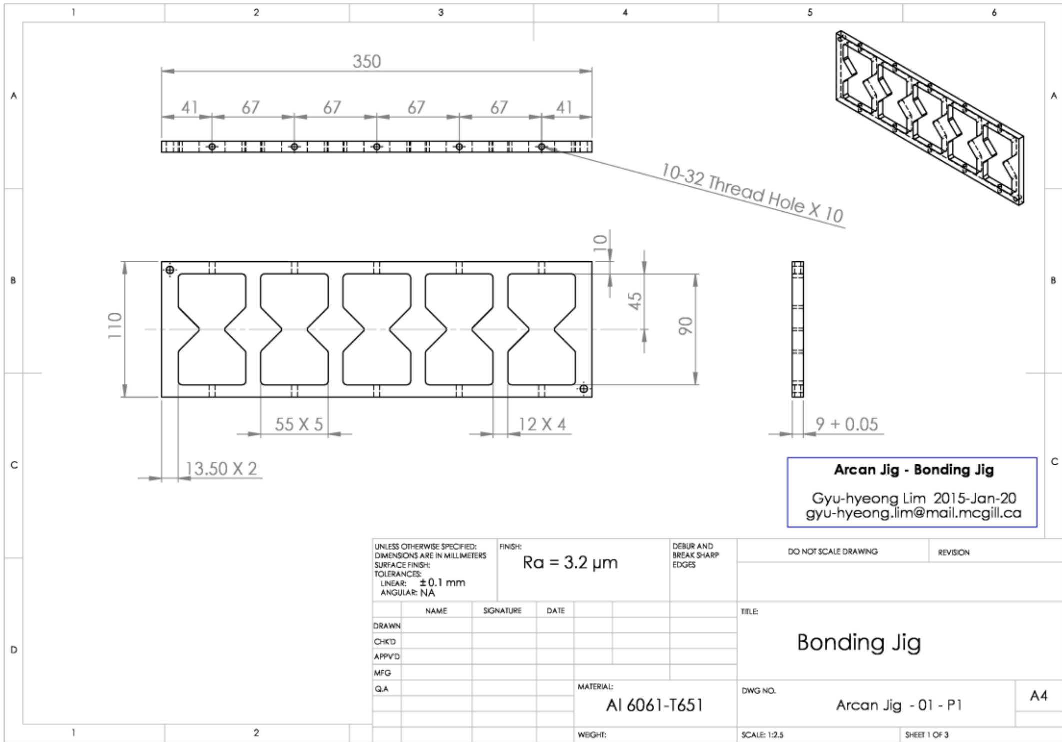

350
41
67
67
67
67
41
10-32 Thread Hole X 10
10
45
90
110
55 X 5
12 X 4
9 + 0.05
13.50 X 2
Arcan Jig - Bonding Jig
Gyu-hyeong Lim 2015-Jan-20
gyu-hyeong.lim@mail.mcgill.ca
UNLESS OTHERWISE SPECIFIED:
DIMENSIONS ARE IN MILLIMETERS
SURFACE FINISH:
TOLERANCES:
LINEAR: ±0.1 mm
ANGULAR: NA
FINISH:
Ra = 3.2 μm
DEBUR AND BREAK SHARP EDGES
DO NOT SCALE DRAWING
REVISION
NAME
SIGNATURE
DATE
DRAWN
CHK'D
APPV'D
MFG
Q.A
TITLE:
Bonding Jig
MATERIAL:
Al 6061-T651
DWG NO.
Arcan Jig - 01 - P1
A4
WEIGHT:
SCALE: 1:2.5
SHEET 1 OF 3

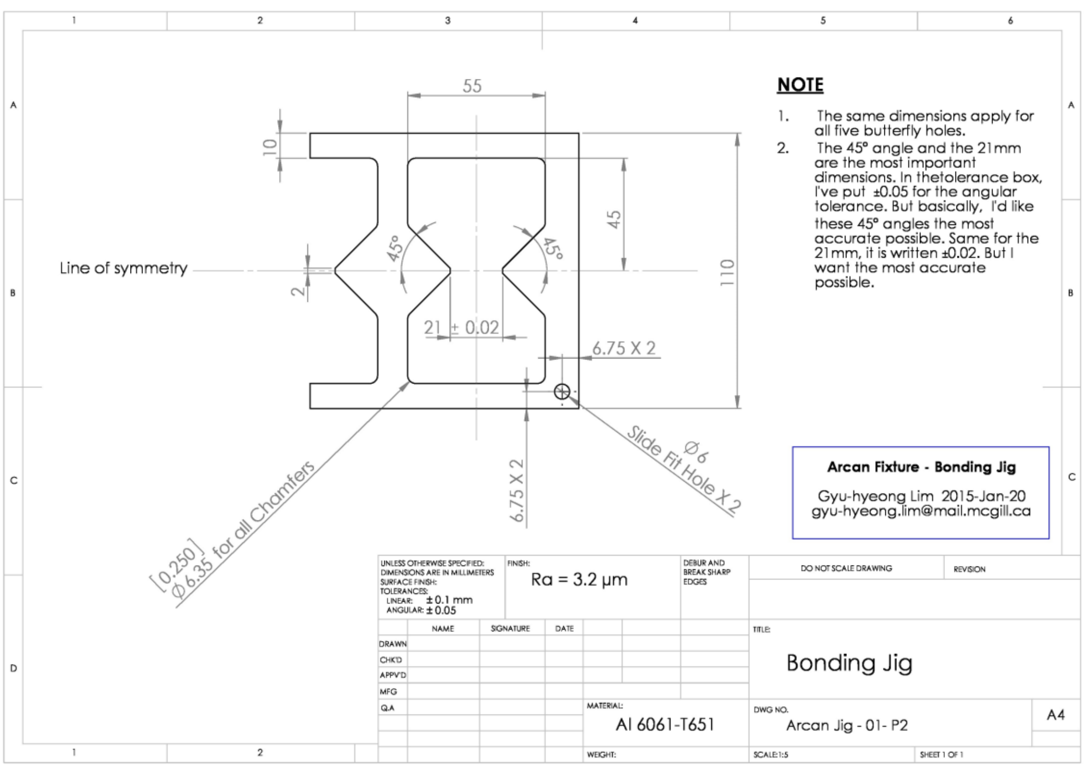

55
10
45
110
Line of symmetry
2
45°
45°
21 ± 0.02
6.75 X 2
6.75 X 2
Ø 6
Slide Fit Hole X 2
[0.250]
Ø 6.35 for all Chamfers
NOTE
1. The same dimensions apply for all five butterfly holes.
2. The 45° angle and the 21mm are the most important dimensions. In thetolerance box, I've put ±0.05 for the angular tolerance. But basically, I'd like these 45° angles the most accurate possible. Same for the 21mm, it is written ±0.02. But I want the most accurate possible.
Arcan Fixture - Bonding Jig
Gyu-hyeong Lim 2015-Jan-20
gyu-hyeong.lim@mail.mcgill.ca
UNLESS OTHERWISE SPECIFIED:
DIMENSIONS ARE IN MILLIMETERS
SURFACE FINISH:
TOLERANCES:
LINEAR: ±0.1 mm
ANGULAR: ±0.05
FINISH:
Ra = 3.2 μm
DEBUR AND BREAK SHARP EDGES
DO NOT SCALE DRAWING
REVISION
NAME
SIGNATURE
DATE
DRAWN
CHK'D
APPV'D
MFG
Q.A
TITLE:
Bonding Jig
MATERIAL:
Al 6061-T651
DWG NO.
Arcan Jig - 01- P2
A4
WEIGHT:
SCALE: 1:5
SHEET 1 OF 1

Jig Assembly

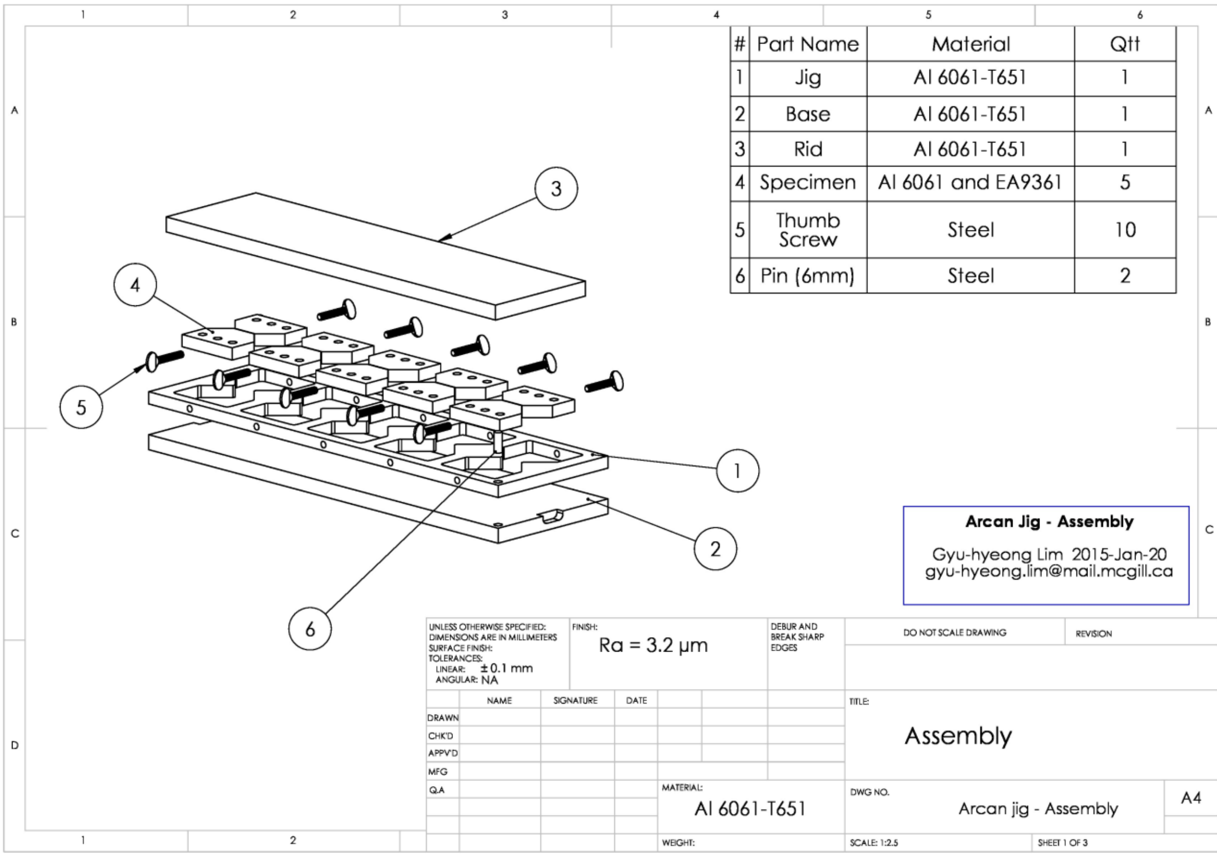

Appendix V. Arcan Fixture Design

Fixture A

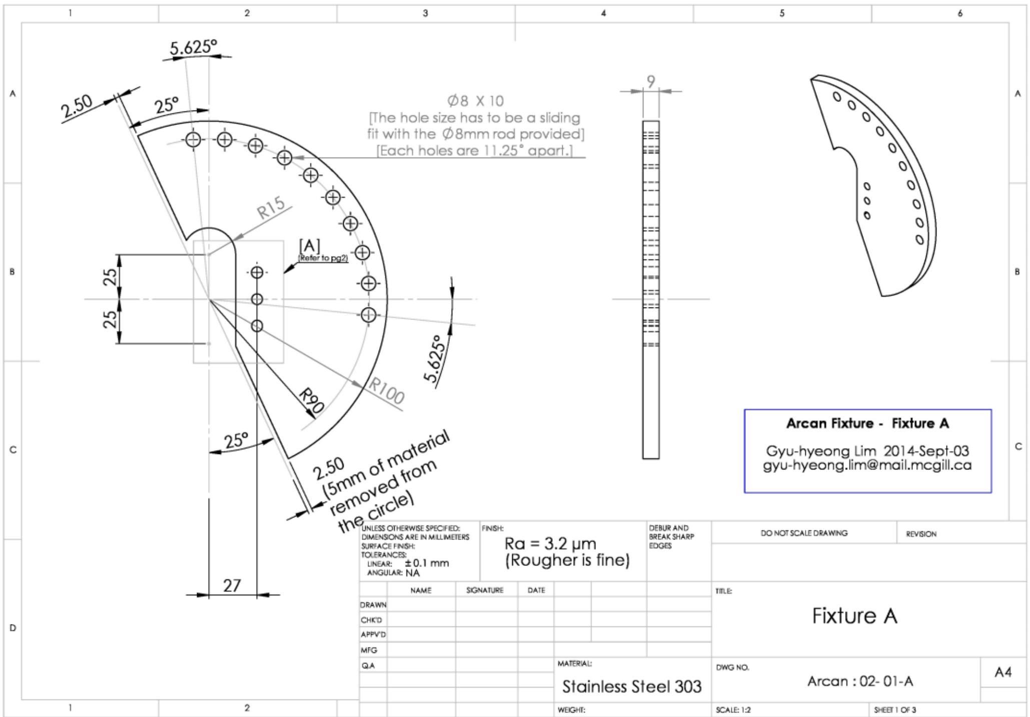

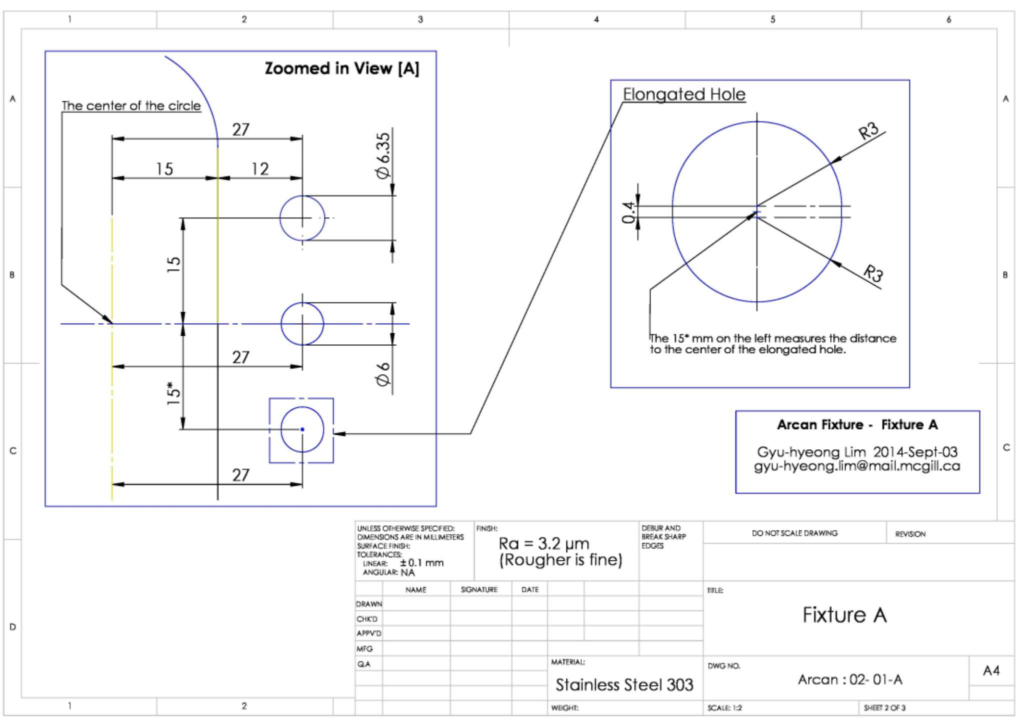

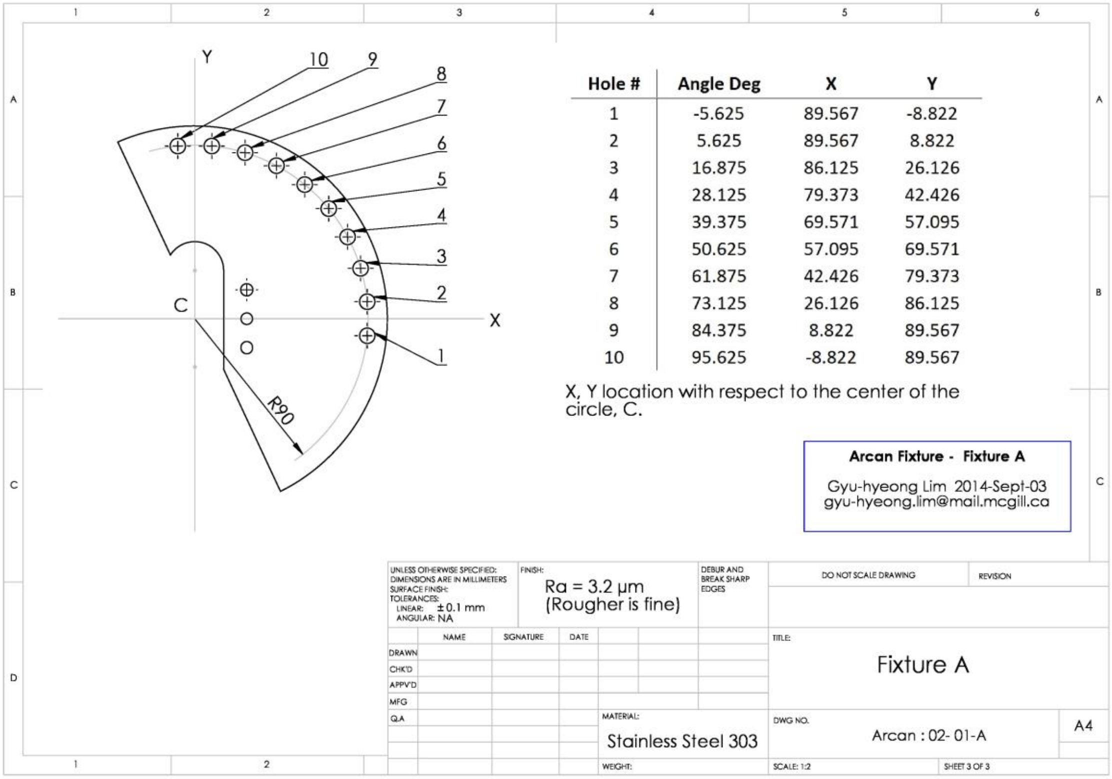

Hole #	Angle Deg	X	Y
1	-5.625	89.567	-8.822
2	5.625	89.567	8.822
3	16.875	86.125	26.126
4	28.125	79.373	42.426
5	39.375	69.571	57.095
6	50.625	57.095	69.571
7	61.875	42.426	79.373
8	73.125	26.126	86.125
9	84.375	8.822	89.567
10	95.625	-8.822	89.567

Fixture B

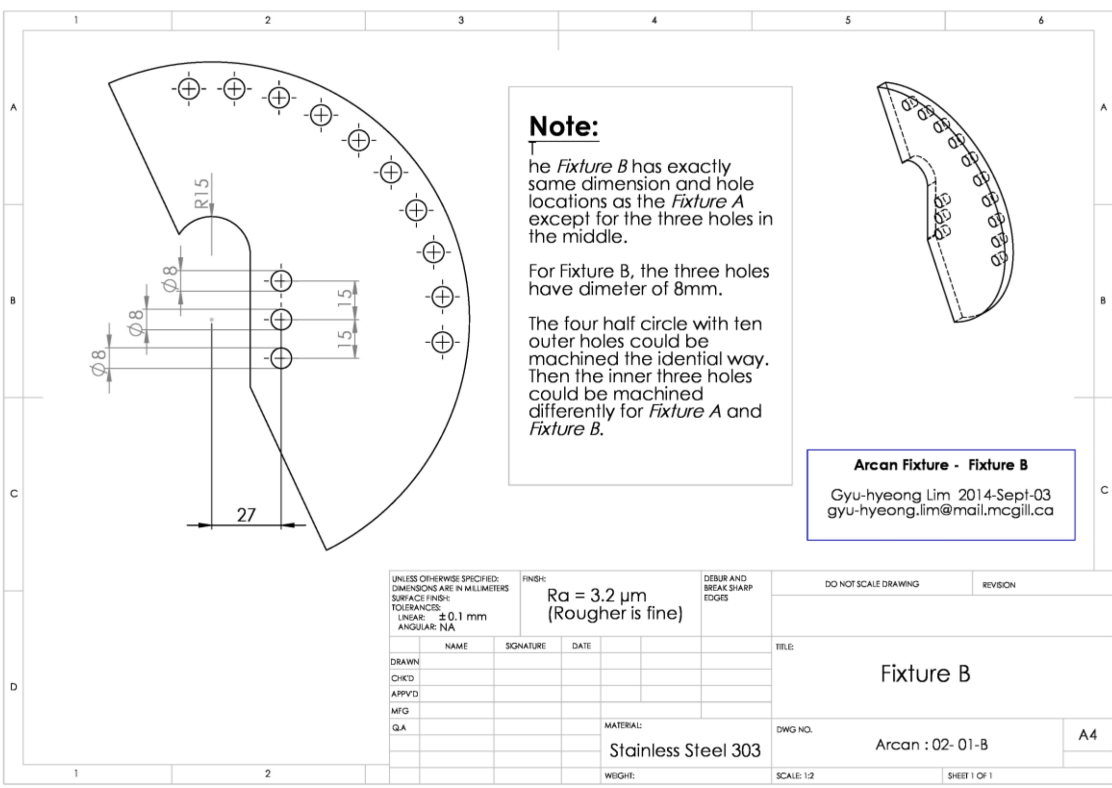

MTS Connector

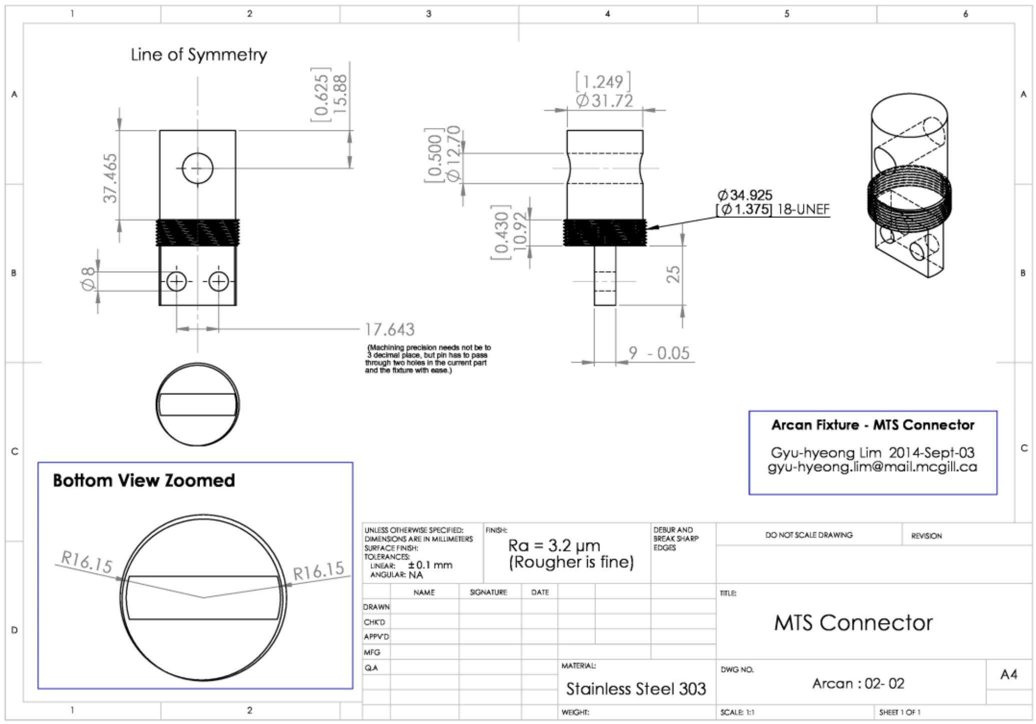

Fixture Assembly

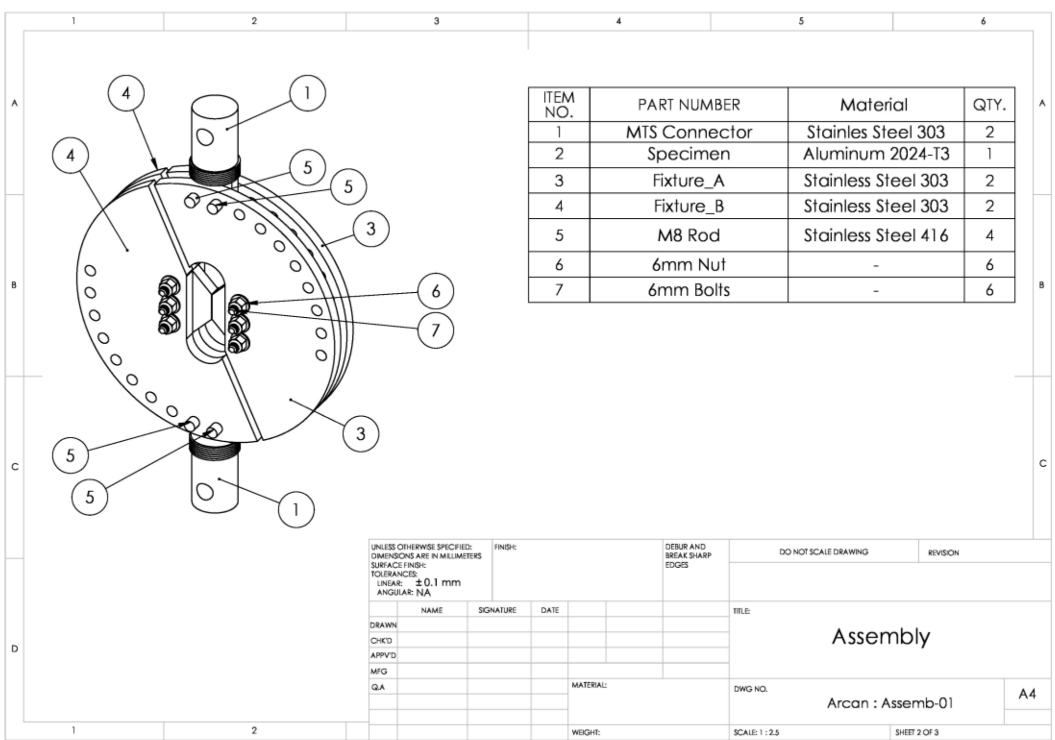

Appendix VI. Temperature Dependency of EA9361

Fermilab's test data by H.Cease [28] characterizes EA 9361 for low temperature range from -173 to 25 °C. The results on modulus, strength and Poisson's ratio are presented by Figure 51, Figure 52 and Figure 53 respectively. Also available data from *Jet Propulsion Laboratory* of California Institute of Technology [29] is the joint lap shear strength measured based on ASTM D1002, ranging from -150 to 100 °C. The tested lap shear strength is curved and plotted in Figure 54.

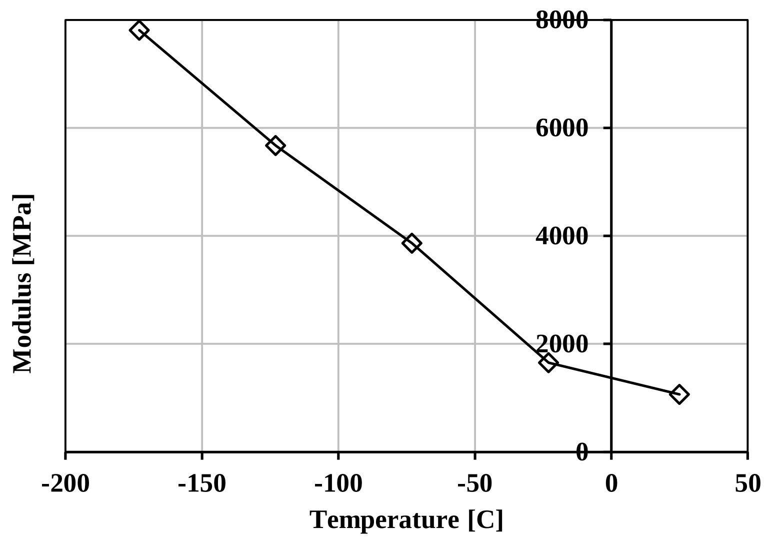

Figure 51. EA9361 – Temperature vs Tensile Modulus

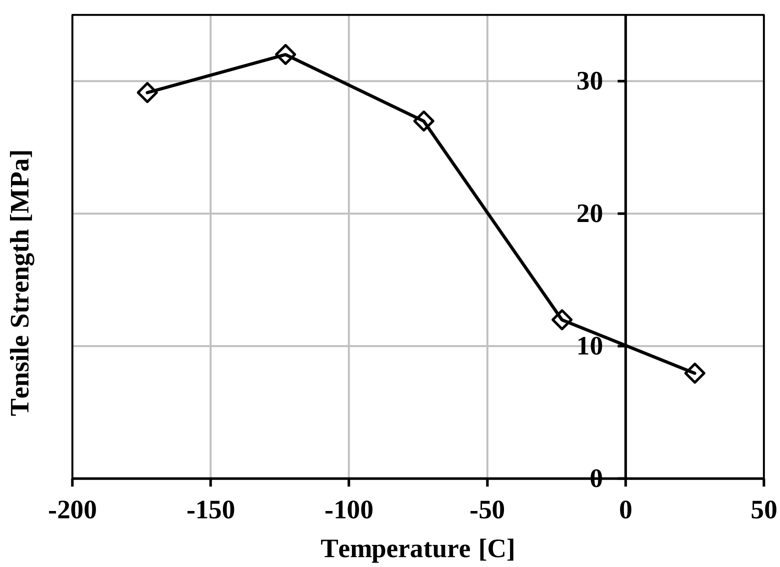

Figure 52. EA9361 – Temperature vs Tensile Strength

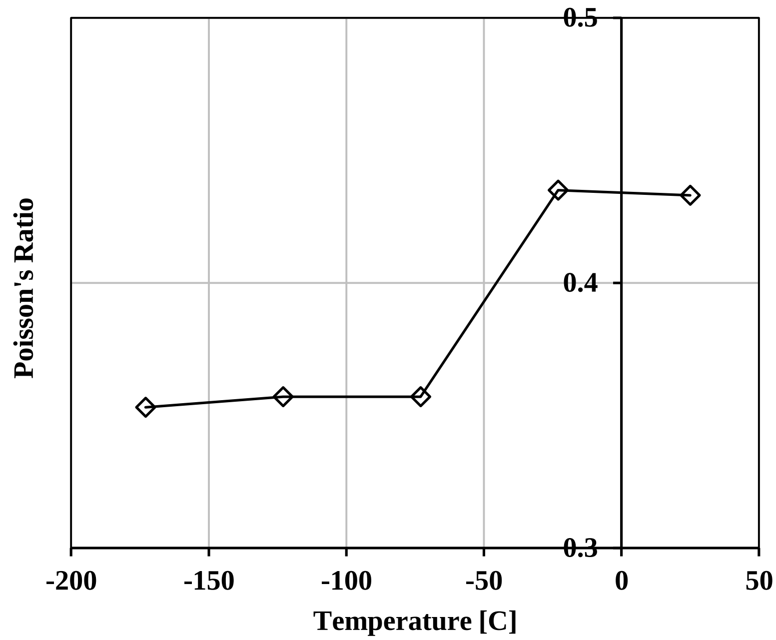

Figure 53. EA9361 – Temperature vs Poisson’s Ratio

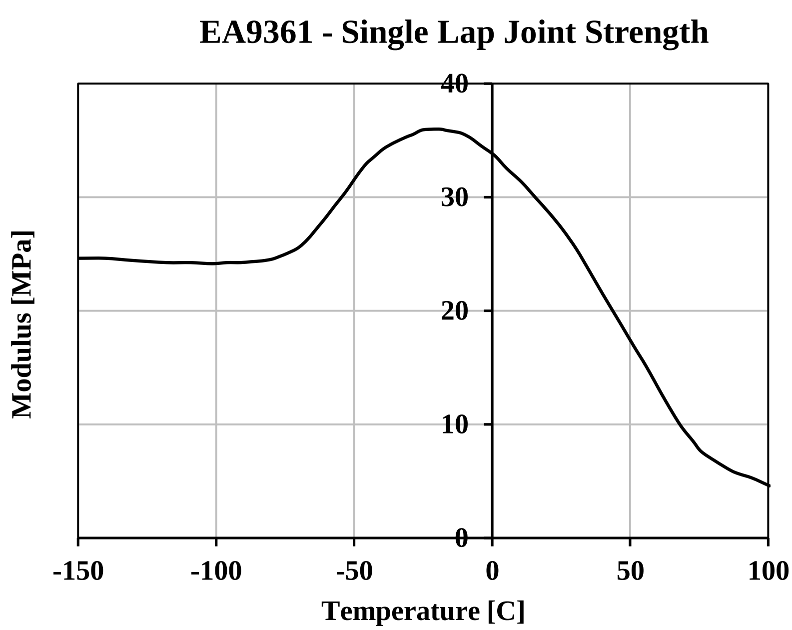

Figure 54. EA9361 – Temperature vs Single-Lap-Joint Bond Strength

References

[1] P. P. Camanho and F. Matthews, "Stress analysis and strength prediction of mechanically fastened joints in FRP: a review," *Composites Part A: Applied Science and Manufacturing,* vol. 28, pp. 529-547, 1997.

[2] E. Godwin and F. Matthews, "A review of the strength of joints in fibre-reinforced plastics: Part 1. Mechanically fastened joints," *Composites,* vol. 11, pp. 155-160, 1980.

[3] S. D. Thoppul, J. Finegan, and R. F. Gibson, "Mechanics of mechanically fastened joints in polymer–matrix composite structures–a review," *Composites Science and Technology,* vol. 69, pp. 301-329, 2009.

[4] F. Matthews, P. Kilty, and E. Godwin, "A review of the strength of joints in fibre-reinforced plastics. Part 2. Adhesively bonded joints," *Composites,* vol. 13, pp. 29-37, 1982.

[5] J. Bickford, *An introduction to the design and behavior of bolted joints, Revised and expanded* vol. 97: CRC press, 1995.

[6] J. Bickford, *Handbook of bolts and bolted joints*: CRC press, 1998.

[7] K. T. Kedward, *Joining of Composite Materials*: ASTM International, 1981.

[8] L. F. da Silva, A. Öchsner, and R. D. Adams, *Handbook of adhesion technology*: Springer Science & Business Media, 2011.

[9] A. Kin Loch and S. Shaw, "The fracture resistance of a toughened epoxy adhesive," *The Journal of Adhesion,* vol. 12, pp. 59-77, 1981.

[10] G. Kelly, "Quasi-static strength and fatigue life of hybrid (bonded/bolted) composite single-lap joints," *Composite structures,* vol. 72, pp. 119-129, 2006.

[11] H.-S. Wang, C.-L. Hung, and F.-K. Chang, "Bearing failure of bolted composite joints. Part I: experimental characterization," *Journal of Composite Materials,* vol. 30, pp. 1284-1313, 1996.

[12] L. J. HART-SMITH, "Bonded-bolted composite joints," *Journal of Aircraft,* vol. 22, pp. 993-1000, 1985.

[13] M. Fu and P. Mallick, "Fatigue of self-piercing riveted joints in aluminum alloy 6111," *International Journal of Fatigue,* vol. 25, pp. 183-189, 2003.

[14] N. M. Chowdhury, J. Wang, W. K. Chiu, and P. Chang, "Experimental and finite element studies of thin bonded and hybrid carbon fibre double lap joints used in aircraft structures," *Composites Part B: Engineering,* vol. 85, pp. 233-242, 2016.

[15] J.-H. Kweon, J.-W. Jung, T.-H. Kim, J.-H. Choi, and D.-H. Kim, "Failure of carbon composite-to-aluminum joints with combined mechanical fastening and adhesive bonding," *Composite structures,* vol. 75, pp. 192-198, 2006.

[16] G. Kelly, "Load transfer in hybrid (bonded/bolted) composite single-lap joints," *Composite structures,* vol. 69, pp. 35-43, 2005.

[17] K. Bodjona, K. Raju, G.-H. Lim, and L. Lessard, "Load sharing in single-lap bonded/bolted composite joints. Part I: Model development and validation," *Composite Structures,* vol. 129, pp. 268-275, 2015.

[18] K. Bodjona and L. Lessard, "Quasi-static strength of hybrid bonded-bolted single-lap joints," presented at the 17th European Conference on Composite Materials, Munich, Germany, 2016.

[19] R. Adams and N. Peppiatt, "Stress analysis of adhesive bonded tubular lap joints," *The Journal of Adhesion,* vol. 9, pp. 1-18, 1977.

[20] A. Loureiro, L. F. Da Silva, C. Sato, and M. Figueiredo, "Comparison of the mechanical behaviour between stiff and flexible adhesive joints for the automotive industry," *The Journal of Adhesion,* vol. 86, pp. 765-787, 2010.

[21] C.-T. Hoang-Ngoc and E. Paroissien, "Simulation of single-lap bonded and hybrid (bolted/bonded) joints with flexible adhesive," *International Journal of Adhesion and Adhesives,* vol. 30, pp. 117-129, 2010.

[22] B. Duncan and G. Dean, "Measurements and models for design with modern adhesives," *International journal of adhesion and adhesives,* vol. 23, pp. 141-149, 2003.

[23] M. D. Banea and L. F. da Silva, "Mechanical characterization of flexible adhesives," *The Journal of Adhesion,* vol. 85, pp. 261-285, 2009.

[24] B. C. D. L.E.Crocker, R.G.Hughes and J.M.Urquhart, *Hyperelastic modelling of flexible adhesives*: NPL, 1999.

[25] Y. I. Dimitrienko, *Nonlinear continuum mechanics and large inelastic deformations* vol. 174: Springer Science & Business Media, 2010.

[26] L. F. da Silva, T. Rodrigues, M. Figueiredo, M. De Moura, and J. Chousal, "Effect of adhesive type and thickness on the lap shear strength," *The journal of adhesion,* vol. 82, pp. 1091-1115, 2006.

[27] F. Kadioglu and R. D. Adams, "Flexible adhesives for automotive application under impact loading," *International Journal of Adhesion and Adhesives,* vol. 56, pp. 73-78, 2015.

[28] H. Cease, P. Derwent, H. Diehl, J. Fast, and D. Finley, "Measurement of mechanical properties of three epoxy adhesives at cryogenic temperatures for CCD construction," *Fermi National Accelerator Laboratory,* 2006.

[29] C. E. Ojeda, E. J. Oakes, J. R. Hill, D. Aldi, and G. A. Forsberg, *Temperature effects on adhesive bond strengths and modulus for commonly used spacecraft stuctural adhesives*: Pasadena, CA: Jet Propulsion Laboratory, National Aeronautics and Space Administration, 2011.

[30] B. C. Duncan, L. E. Crocker, and J. M. Urquhart, *Evaluation of hyperelastic finite element models for flexible adhesive joints*: National Physical Laboratory. Great Britain, Centre for Materials Measurement and Technology, 2000.

[31] "Technical Datasheet Hysol EA9361," Henkel Corporation Aerospace Group.

[32] "ASTM D638-14 Standard Test Method for Tensile Properties of Plastics," ed: American Society for Testing and Materials, 2014.

[33] V. Weissberg and M. Arcan, "A uniform pure shear testing specimen for adhesive characterization," in *Adhesively Bonded Joints: Testing, Analysis, and Design*, ed: ASTM International, 1988.

[34] R. M. Christensen, *The theory of materials failure*: Oxford University Press, 2013.

[35] B. Loret and J. H. Prevost, "Accurate numerical solutions for Drucker-Prager elastic-plastic models," *Computer Methods in Applied Mechanics and Engineering,* vol. 54, pp. 259-277, 1986.

[36] "ASTM D5379-12 Standard Test Method for Shear Properties of Composite Materials by the V-Notched Beam Method," ed: American Society for Testing and Materials, 2012.

[37] J.-Y. Cognard, L. Sohier, and P. Davies, "A modified Arcan test to analyze the behavior of composites and their assemblies under out-of-plane loadings," *Composites Part A: Applied science and manufacturing,* vol. 42, pp. 111-121, 2011.

[38] A. Bansal and M. Kumosa, "Application of the biaxial Iosipescu method to mixed-mode fracture of unidirectional composites," *International journal of fracture,* vol. 71, pp. 131-150, 1995.
[39] R.W.Ogden, *Non-linear Elastic Deformations*: Courier Corporation, 1984.
[40] K. Bodjona and L. Lessard, "Nonlinear static analysis of a composite bonded/bolted single-lap joint using the meshfree radial point interpolation method," *Composite Structures,* vol. 134, pp. 1024-1035, 2015.
[41] "Simulation of Single-Lap Bonded and Hybrid(Bolted/Bonded) Joints with Flexible Adhesive," *International Journal of Adhesion and Adhesives,* vol. 30, pp. 117-129, 2010.
[42] "Measurements and Models for Design with Modern Adhesives," *International Journal of Adhesion and Adhesives,* vol. 23, pp. 141-149, 2003.
[43] G. B. Dantzig, *Linear programming and extensions*: Princeton university press, 1998.
[44] C. H. Wang and P. Chalkley, "Plastic yielding of a film adhesive under multiaxial stresses," *International Journal of Adhesion and Adhesives,* vol. 20, pp. 155-164, 2000.
[45] S. Yoneyama, H. Kikuta, A. Kitagawa, and K. Kitamura, "Lens distortion correction for digital image correlation by measuring rigid body displacement," *Optical engineering,* vol. 45, pp. 023602-023602-9, 2006.
[46] K. Bodjona and L. Lessard, "Load sharing in single-lap bonded/bolted composite joints. Part II: Global sensitivity analysis," *Composite Structures,* vol. 129, pp. 276-283, 2015.
[47] (2015). *McMaster Carr - Black-Oxide Alloy Steel Socket Head Cap Screw 1/4"-28 Thread, 3/4" Length*. Available: http://www.mcmaster.com/#91251a440/=139nxpz
[48] (2015). *McMaster Carr - Type 316 Stainless Steel SAE Flat Washer Number 10 Screw Size, 0.219" ID, 0.500" OD*. Available: http://www.mcmaster.com/#91950a027/=139nzmb